UNIVERSITY OF CALIFORNIA
SANTA CRUZ

# LOW-COST WEARABLE DATA-ACQUISITION SYSTEM ENHANCED WITH BIOMECHANICAL ANALYSIS

A dissertation submitted in partial satisfaction of the
requirements for the degree of

DOCTOR OF PHILOSOPHY

in

COMPUTER ENGINEERING

by

**Erik Jung**

June 2022

The Dissertation of Erik Jung
is approved:

---

Dr. Mircea Teodorescu, Chair

---

Dr. Sri Kurniawan

---

Dr. Steve McGuire

---

Peter Biehl
Vice Provost and Dean of Graduate Studies

# Table of Contents

# List of Figures

# List of Tables

## Abstract

Low-cost Wearable Data-acquisition System Enhanced with Biomechanical Analysis by Erik Jung.

Wearable robotics have been proposed as one possible solution for increasing mobility and enhancing the stability and strength of users requiring prosthesis or musculoskeletal augmentation. However, most robotics literature neglects the internal flexibility of any anatomic joints. It views the human limbs (and therefore their replacements) as rigid elements connected by revolute joints with a confined range of motion. Tensegrity-inspired designs replicate the musculoskeletal connections using compressive and tensile components within a self-stabilizing structure, preserving the hybrid (rigid/flexible).

Traditionally, monitoring biomechanics parameters requires a significant amount of sensors to track exercises such as gait. Both research and clinical studies relied on intricate motion capture studios to yield precise measurements of movement. The advantage of the IMU-based (inertial measurement units) system used is that it does not require a fixed array of infrared (IR) cameras; therefore, it is not only significantly cheaper, but it is also less restricted by its environment. Biomechanic simulation environments, such as OpenSim, are commonly used for their complex multi-body dynamics solvers [23], and this work extends the framework to simulate the behavior of flexible-rigid robotic systems within the same environment.

Specifically, in this thesis I discuss a method that captures motion independently of optical hardware with the specific goal of tracking joint-angle measurements with IMU sensors. I extended this approach to the control strategy and the sensing network for flexible-rigid robotics and human movements like walking for gait phase classification. Additionally, I interpreted the biomechanics solvers

from OpenSim to generalize a set of required maximum joint-moments to transition between stages of gait based on physical characteristics (e.g., height, weight, etc.). To my knowledge, integrating flexible-rigid structures and human subjects using IMU sensors with complex biomechanics solvers has never been proposed before. This work could help applications beyond monitoring the phases of gait with direct applications to medical and assistive technology fields.

The work in this dissertation is dedicated to my mother, Dr. Connie Conley-Jung or Mama Jung.

# Acknowledgments

To the family I was born with and the one I met along the way, thank you for **everything**.

Firstly, I would like to thank Dr. Mircea Teodorescu for not only being an amazing mentor and advisor, but a life-long friend. Mircea and his wife, Dr. Sri Kurniawan, treated their students like their own family. They hosted many celebrations to celebrate milestones and graciously offered food to anyone hungry. They constantly provided many favors (e.g., doctor visits, moving, etc.) that undeniably make them one of the most selfless people I have met in my life, and I feel y lucky to have had them in my life.

Thank you to my parents, Dr. Leland Jung and Dr. Connie Conley-Jung, who always fed us, and with open arms, invited us to camp out during a fire evacuation, global pandemic, and weekend getaways. You taught me how to balance dreams and reality and bring out the best in myself and others, shaping me into the person I am today. You guys did a fantastic job raising not just one kid but all of my friends, giving us all something we could call home. I love you both more than you could ever imagine.

For Dr. Victoria Ly, thank you for being my partner in life. Thank you for constantly reminding me to eat and, most importantly, take a step back to enjoy life in the moment. Every single day you not only simultaneously impress and inspire me, you make me better and happy, making me feel like the luckiest person on Earth to just be around you. I'm excited for our next chapter. I love you to infinity & beyond.

Thank you to my grandparents, Sally and Arlan Jung and Ute and Bill Conley, for introducing me to the world of technology, and providing constant support and

unconditional love. Thank you for always looking after me.

Thank you to my friends. You are the brothers and sisters I always dreamed of having. You have, and always will be, family to me. Thank you for always supporting me and sponsoring a broke college student dinners and drinks. Now it's my turn to return the favor.

Thank you to my team for teaching me so much and making every day uniquely fun: Christopher Cheney, Martin Contreras, Cheryl Lin, Adam Buderi, Archisha Sinha, David Prager, Emma Appleton, Dylan Yong, Lawrence Ngo, Nick Cessna, and Quitong Li.

Thank you to my fellow lab mates: Dr. Pattawong Pansodtee, Dr. Alex Mazhari, Dr. Mike Powell, Gordon Keller, Ash Robbins, and Dr. Steven Lessard for teaching me so much and introducing me to so many different worlds. I will definitely cherish those moments together.

Lastly, thank you again to my committee members: Dr. Steve McGuire, Dr. Sri Kurniawan & Dr. Mircea Teodorescu for participating in this monumental milestone in my life that I will cherish forever.

# Publications

## Journal Papers

**Jung, E.A.**, Lin C, Contreras M, Teodorescu M, "Applied Machine Learning on Phase of Gait Classification and Joint-Moment Regression." *Biomechanics* 2, 44–65 (2022)

**Jung, E.A.**, Ly V, Cheney C, Cessna N, Ngo ML, Castro D, Teodorescu M. "Design, Construction and Validation of a Proof of Concept Flexible–Rigid Mechanism Emulating Human Leg Behavior." *Applied Sciences* 11.19:9351 (2021)

Baudin PV, Ly VT, Pansodtee P, **Jung, E.A.**, Currie R, Hoffman R, Willsey HR, Pollen AA, Nowakowski TJ, Haussler D, Mostajo-Radji MA. "Low cost cloud based remote microscopy for biological sciences". *Internet of Things* 100454 (2021)

Ly VT, Baudin PV, Pansodtee P, **Jung, E.A.**, Voitiuk K, Rosen Y, Willsey HR, Mantalas GL, Seiler ST, Selberg JA, Cordero SA, Ross JM, Rolandi M, Pollen AA, Nowakowski TJ, Haussler D, Mostajo-Radji MA, Salama SR, Teodorescu M "Picroscope: low-cost system for simultaneous longitudinal biological imaging".Communications biology 4.1: 1-11 (2021)

Chen LH, Kim K, Tang E, Li K, House R, Zhu EL, Fountain K, Agogino AM, Agogino A, Sunspiral V, **Jung, E.A.** "Soft spherical tensegrity robot design using rod-centered actuation and control." *Journal of Mechanisms and Robotics*. 9.2 (2017).

### In Review

**Jung, E.A.**, Cheney C, Contreras M, Yong D, Ly V, Teodorescu M, Low-cost motion tracking system using OpenSim for kinematic and dynamic analysis. PLoS ONE.

Parks, D.F., Voitiuk, K., Geng, J., Elliott, M.A., Keefe, M.G., **Jung, E.A.**, Robbins, A., Baudin, P.V., Ly, V.T., Hawthorne, N. and Yong, D., 2021. Internet of Things Architecture for High Throughput Biology.

## Conference Papers

**Jung E**, Ly V, Buderi A, Appleton E, Teodorescu M. Design and Selection of Muscle Excitation Patterns for Modeling a Lower Extremity Joint Inspired Tensegrity. In 2019 Third IEEE International Conference on Robotic Computing (IRC) 2019 Feb 25 (pp. 282-287). IEEE.

**Jung E**, Ly V, Cessna N, Ngo ML, Castro D, SunSpiral V, Teodorescu M. Bio-inspired tensegrity flexural joints. In 2018 IEEE International Conference on Robotics and Automation (ICRA) 2018 May 21 (pp. 5561-5566). IEEE.

**Jung E**, Ly V, Castro D, Teodorescu M. Knee-inspired tensegrity flexural joint. In Ubiquitous Robots (UR) 2018, Oahu, Hawaii, IEEE International Conference 2018.

Baltaxe-Admony, L. B., Robbins, A. S., **Jung, E. A.**, Lessard, S., Teodorescu, M., SunSpiral, V., & Agogino, A. (2016, August). Simulating the human shoulder through active tensegrity structures. In International Design Engineering Technical Conferences and Computers and Information in Engineering Conference (Vol. 50183, p. V006T09A027). American Society of Mechanical Engineers.

Lessard, S., Bruce, J., **Jung, E.**, Teodorescu, M., SunSpiral, V., & Agogino, A. (2016, May). A lightweight, multi-axis compliant tensegrity joint. In 2016 IEEE International Conference on Robotics and Automation (ICRA) (pp. 630-635). IEEE.

# Chapter 1

# Introduction

## 1.1 Motivation

Musculoskeletal health issues create a great deal of stress and demands on health care systems worldwide and cost the US economy over $849 billion annually [24]. In the United States alone, about two million people live with limb loss, and about 185,000 amputations occur each year [25, 26]. Those with limb loss and amputations may require long-term rehabilitation as well as mobility technologies to monitor or assist with walking or standing. For optimal rehabilitation treatment planning, it will be beneficial if therapists are supported by combined software tools and data acquisition methods to automate some of the data recording and monitoring activities. These tools and data acquisition methods should ideally be equipped with some indicative capabilities based on a level of biomechanics modeling. This modeling requires a deep understanding of quantitative movement analysis, which involves an understanding of limb movements, rehabilitative practices and overall dynamic behaviors of muscles and joints.

Biological systems provide natural flexibility and structural compliance with movements, allowing for non-permanent deformation while maintaining initial

equilibrium. Skeletal-based arrangements use muscles and tendons to distribute forces throughout the entirety of the system. When external forces act upon an anatomical structure, its natural flexibility adapts and distributes the internal stresses within the system, which allows for use in unpredictable environments [27]. Common robotics (e.g., industrially robotic manipulators) appear stiff with little to no structural flexibility [28]. When external forces act upon these rigid structures, the combination of rigid links with revolute or sliding interconnections often cannot handle the irregular forces and lead to failures [27, 29].

Traditional mobility devices (e.g., prostheses, exoskeletons, crutches) follow a rigid mechanical structure that is capable of handling and exerting excess amounts of force [3], but lack the innate flexibility of anatomical systems in human leg joints [26]. One compromise between soft and hard robotic classifications are "tensegrity" (known as "tensile with integrity") flexible-rigid robotic systems [30, 14, 18, 31]. In tensegrity arrangements, the articulation consists of rigid compression elements held together within a network of flexible tension elements [14, 31]. The benefits of flexible-rigid robotics are that they use static, rigid elements to support a load and implement elastic tension elements to manipulate and evenly disburse forces while absorbing external impacts similar to the dampening features in passive robots [20]. The movement of these types of robotics use cable-driven actuation to follow that lengthening and contraction patterns of muscles or tendons in the human body.

This thesis focuses on a sequence of modeling, designing, and monitoring flexible-rigid robotics and validating them using human subjects. The development focused on sensory-based feedback (e.g., angular rate and direction sensors) with a distributive wireless network that classifies the kinematic behavior of human gait. To apply the recordings from these sensors, an additional solver iden-

tifies the phase of gait from joint-angle measurements and generalizes a set of required joint-moments between those phases of gait.

## 1.2 Applications

This work takes a holistic approach to the model and design methodology bridging bio-inspired robotics and user studies. Specifically, the work contributes to the following:

- Flexible-rigid robotics - model, simulate, measure, and control a series of prototypes that replicate musculoskeletal connections within joints, specifically by connecting the rigid (e.g., bones) and tensile elements (e.g., muscles, tendons).

- Low-Cost Motion Capture Systems - Motion capture systems are generally room-bound and expensive, making them inaccessible for the general public. Our system can provide joint kinematics and dynamics using wearable IMU sensors creating new opportunities for those who can not afford expensive motion capture systems.

- Rehabilitation - the IMU-based sensing system can be adapted for wearable biomechanics devices used for rehabilitation [32].

- Remote Evaluation and Telehealth - Our sensors enhanced with bio-mechanical solvers will help physical therapists monitor patients' recovery remotely or at home.

## 1.3 Contributions

The work in this dissertation describes the design, development, experimentation, and analysis to create a biometric motion system enhanced with bio-mechanical solvers. The contributions are listed below.

- Successive generations of design frameworks that can generate custom models in an open-sourced biomechanical simulation environment.
- A methodology for developing a wearable wireless network using off-the-shelf components to assess the kinematic behaviors of a variety of human subjects.
- Several generations of bio-mechanical pipelines to determine the kinematic and dynamic behaviors.
- A set of machine learning-based algorithms to predict complex motions of human subjects.

The dissertation concludes with a summary of potential applications for future research.

# Chapter 2

# Literature Review

## 2.1 Introduction

Biomechanics field is a study of biological systems and the mechanical effects on the body's movement, size, shape, and structure [33]. The quantitative study of time-motion problems by Fischer as cited by [1, 33] proposed a two-dimensional rough representation of a human model to calculate the muscle force dynamics for the swing phase of walking, and later by Bernstein and Elftman as cited by [33] to obtain moments on the joints or points of support in the human body. Limited by the computational technology of their time and by the complexity of the problem, the simplified set of equations of motion were incapable of completely modeling human behavior, but they set the foundation for future work. Those initial set of equations [1] were modeling human behavior as mechanical systems with rigid bars, links, and springs that these mathematicians were familiar with. In an ideal world, we would want to take into account:

- unique strengths/applied forces that vary between individuals
- random initial positions and velocities

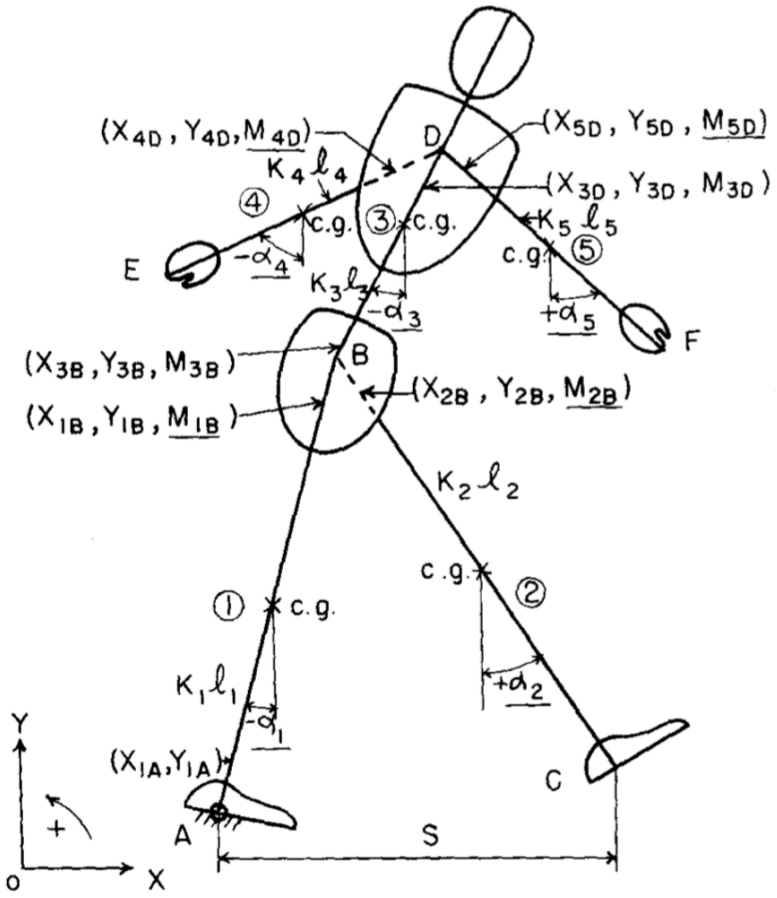


**Figure 2.1:** Illustration of the "minimal principle" on the sagittal plane by removing the *unknowns* for the equation of dynamics on the characteristics of segments and the joints [1].

- calculating moments at each joint grouped several muscles by ignoring individual muscle-tension
- inconsistent gait patterns, or step lengths

Consequentially, the constraint and limitations set were speculative. In pursuit of a systematic understanding for measuring body movements, mechanics, and activity of the muscles, a special branch of human motion analysis known as *gait analysis* became the specific study of human walking to assess, plan and treat subjects with conditions affecting their ability to walk [34].

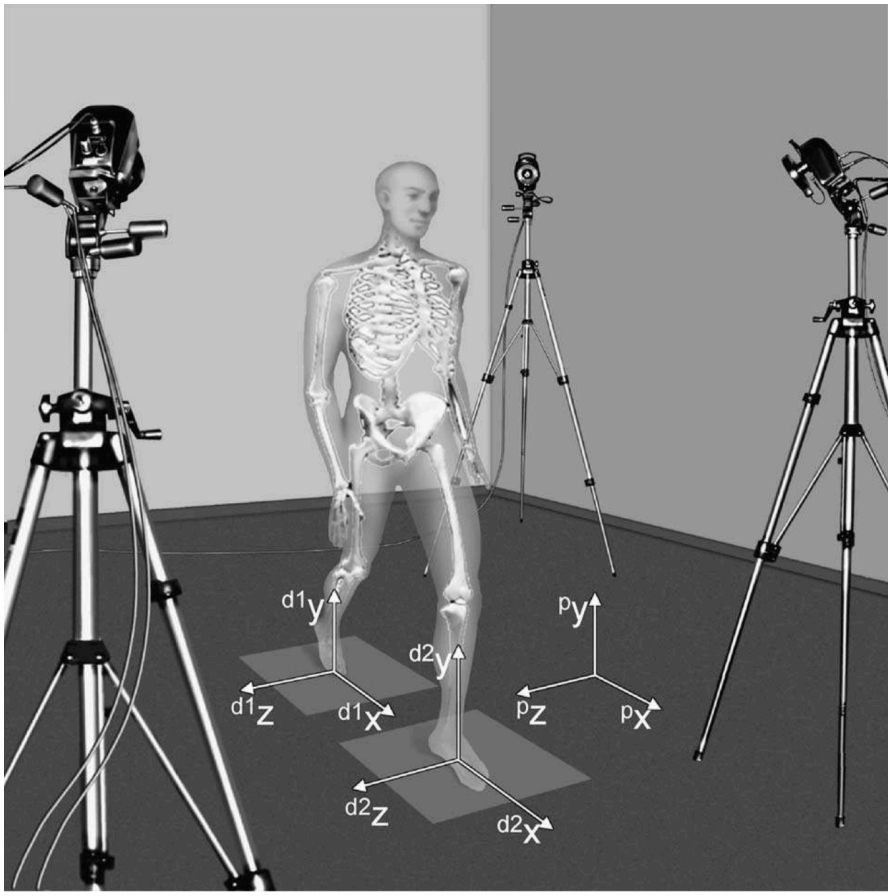


**Figure 2.2:** Stereophotogrammetry involves the 3D coordinates of pointing at an objects by employing 2 or more photographic images taken from different positions. The calculation is a collection of points obtained along a Cartesian coordinate system [2]

Some of the earliest findings for achieving mental and physical excellence for athletic activity dates back to when Aristotle wrote the first book on scientific analysis of human movement as mentioned by [35, 34]. Even though detailed anatomy of the human body existed [34], proper quantitative measuring techniques did not. The first true study of human motion occurred when a series of human locomotion exerted at each moment was measured using glass-plates and celluloid film chronophotography [35, 34]. During that time, Carlet added a heel and forefoot to pressure-recording shoes quantifying vertical reaction forces

[34]. It was not until Eadweard Muybridge (considered the "Father of Modern Gait Analysis") improved photography to 1/100 of a second to record motion and led to stereophotogrammetry [36, 37]. Using stereophotogrammetry (Figure 2.2) and ground reaction forces (GRF), they estimated 3D position data from images and linked it with the mathematical methoodology for gait analysis developed by Fischer all before computers were invented [1, 33, 34].

Due to the laborious and erroneous nature of manual involvement for determining specific markers on the human body in individual images, the modern era ($20^{th}$ century – today) led to exponential advancements in analysis of human motion. During the 1940s, Edgerton was able to photograph at several million exposures per second which eventual led to the 1970 "golden standard" of motion capturing with optical systems, such as infrared high-speed cameras as cited by [34]. The advancements in optical motion capture systems produced detailed motion analysis results with the collocation of computers. However, most of the interest for clinical applications (e.g., injured patients, limb replacements, assistive mobility devices) did not gain traction until after the World War I.

## 2.2 Assistive Technologies for Mobility

As bad as it sounds, war drives innovation. The application for lower limb augmentation or alternatives (for those who are incapable of mobility) research has been geared for disabled people, patients, soldiers, and ordinary people [38]. This section intends to cover the evolution in mobility devices ranging from assistive, training, or external devices such as crutches, canes, and walkers.

Wheelchairs are a consistent and reliable form of transportation for any individual where walking is difficult due to illness, injury, or disability [39]. The first invented wheelchair was for Philip II of Spain in 1595 (Figure 2.3A). Today,


**Figure 2.3:** The evolution of the wheelchair from the first manual to a fully powered and sit-to-stand version. (A) 1595 manual wheelchair (B) $21^{st}$ Century manual wheelchair (C) Powered wheelchair (D) Powered sit-to-stand wheelchair

the manual wheelchair shown in Figure 2.3B has not made any significant design changes and functions essentially the same. One critical update to the design of a wheelchair was motorizing the wheels. Powered wheelchairs (Figure 2.3C and Figure 2.3D) have made great use of human-computer interfaces (HCI) such as Brain Computer Interfaces (BCI) and electromyography (EMG) signals [38, 40, 41]. BCI directly measures the electrical activity in the brain to and from an external device like a computer or wheelchair in this example [40]. EMG similarly senses electrical activity but instead with the nerve-muscle connections in the body. The sense of self-reliance in wheelchairs (powered in particular) increases by reducing the dependency on caregivers and family members. This device represents the fundamental element behind developing assistive technology, giving users the ability to live more independently.

Those who did not have a high degree of disability, or were only temporarily affected by an injury, took great assistance from external devices like canes, crutches, or walkers. Rehabilitative and mobility aid devices were first introduced and patented in 1917 during World War I [42] by Emile Schlick (Figure 2.4(A)). The design of the crutch since then has not changed since Anders R Lofstrand, Jr. designed the height-adjustable feature for personal customization yet again during


**Figure 2.4:** Examples of passive, or unpowered crutches. (A) 1917 Crutch (B) 1945 Height-adjustable Crutch (C) 1953 Forearm Crutch (D) 1999 Hands-free crutch

the end of World War II in 1945 [42] (Figure 2.4(B)). By 1953, Thomas Fetterman [43] designed the forearm crutch (Figure 2.4(C)) that remedied the impact on the armpit but still required a heavy amount of use on the upper body. The design comes off to be very similar to that of a cane. After 40 years, Lance Matthews designed a hands-free crutch primarily due to the annoyance of not doing things with upper extremities (Figure 2.4(D)). Although these were all functional compensations to support walking, balance and increasing gait stability, they were also useful for rehabilitation training [38].

Other mobility-training, or rehabilitative technologies, include parallel bars or treadmills to regain strength for gait [38]. This form of contraption assists patients with concise and repetitive movements to improve their ability to walk independently. However, the main caveat is the cost and how these devices are considered less effective than therapist-assisted training, proving there is room for improvement on monitoring repetitive motions in a reliable, portable, and cost-effective manner.

The last form of mobility devices covered in this review includes external devices such as exoskeletons and prostheses. Research of powered human exoskeleton devices began in the late 1960s and focused on developing technologies for augmenting able-bodied humans with a future intent for developing assistive technologies for physically challenged persons [44]. In 1962, Cornell discovered that even after using master-slave robotic system as a *man-amplifier*, the structure and shape is similar to the human body has far fewer degrees of freedom than the average human [45]. Berkeley's exoskeleton unveiled in 2004 was a hydraulic actuated device that was capable of enhancing the strength of the user [3].

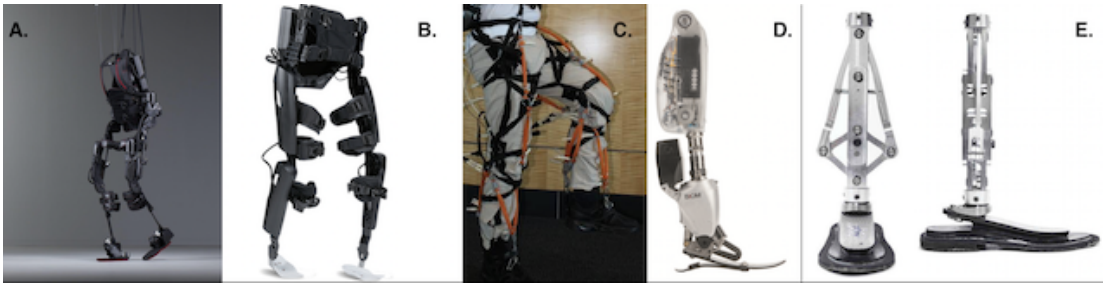


**Figure 2.5:** A: Ekso Bionics exoskeleton [3]. B: ReWalk exoskeleton [4] C: Soft gait-assistive exoskeleton [5]. D: Clutchable Series-Elastic Actuator (CSEA) Prosthetic [6]. E: Mediolateral Prosthetic [7]

Companies like Ekso Bionics (Figure 2.5A), Indego, and ReWalk (Figure 2.5B) all follow very similar dynamics, but gear their devices towards rehabilitative purposes. For this review, exoskeletons are referenced to be an active mechanical device that acts essentially anthropomorphic in nature and fits closely to the human body. *Active orthosis* is used to describe a device that increases the ambulatory abilities of a person who suffers a leg pathology [44]. Currently, there are problems people are still facing when creating the *ultimate augmenting* or *assistive system*. Having technology accurately comprehend the interaction between human and such technologies for complex kinetic movement is competitively researched. Oddly enough, Schiele found joint torques can be generated by joint misalignment,

and cause time delays on the exoskeleton's moves related to the user [46]. The weight of the exoskeleton and the misalignment of joints can disturb the gait and generate resistance [47]. The inertia of the leg can be changed by additional mass to the legs that increases the metabolic cost during movement of the legs with acceleration [48] [49]. Due to that fact, it requires so much energy for the users to operate these powered exoskeletons, soft wearable exoskeletons came back into the picture in 2011 [5, 47]. Park created an active soft orthosis specified for assisting ankle movements, Stirling made an ankle and knee assistive device, Kawamura made a proposed hip flexion robot [50], and Wehner created a soft pneumatically-actuated exosuit for assisting gait. Asbeck developed a soft exoskeleton that uses wire-driven mechanisms to disperse the center of mass (COM) up to the upper body to reduce the metabolic usage [51]. Unlike traditional exoskeletons, this system was lightweight and portable. Advantages of using wire-driven mechanisms include the weight of the system producing lower inertia and reduced user effort to lift the device. Another upside is the humans' kinematics is not restricted like most traditional rigid exoskeletons due to the flexibility and solved misalignment problems.

Powered systems usually increase the load carrying capacity through increased electrical current and allow for a greater degree of control of the system as a whole [3, 52]. Conversely, passive systems do not have any electrical power source and utilize weight re-distribution, energy recapturing, dampening and locking mechanisms by means of springs or shock absorbers to alleviate strain on users [3, 53]. This variant of actuation allows for a higher degree of unassisted motion whilst still providing some of the basic advantages of a robotic system. In addition to the traditional hard and soft robotics, quasi-passive exoskeletons (Figure 2.6) were created for people who just needed a bit of assistance or enhancement of their


**Figure 2.6:** Quasi-passive knee exoskeleton that varies spring levels by the timing of engagement/disengagement to accommodate for mechanical performance and reliability [8].

daily tasks [8, 54]. These exoskeletons help reduce the carrying load of individuals while requiring little to no power consumption [55, 56, 57].

The combination of prostheses, wheelchairs, and crutches works harmoniously to help those in need with mobility. Both have their trade-offs that help complement and compensate for limitations between devices. Since wheelchairs have made significant improvements in the development and variety of mobile applications with powered systems [39], there is much room for innovating crutches and prostheses.

In summary, we made a brief overview of existing assistive mobility devices. The rehabilitation clinical research and therapy assists patients with gait abnormalities and rebuild insufficient muscle strength [47]. Soldiers and ordinary people use exoskeletons to enhance their current body strength for either military applications like moving war supplies and weapons easily, or assist workers in the industrial site with construction [44]. This specific area of technology has made great advances over the past years, but there will always be room for improvement:

- wheelchairs – reliable for flat and even surfaces, but it is not great for extended use (e.g., osteoporosis, bone loss, low blood circulation) or inclines and stairs

- crutch – useful for rehabilitative exercises to regain strength, but it is uncomfortably rigid for long periods of use and limited to those with a less severe degree of disability

- parallel bars or treadmill – monitoring is concise with repetitive movements, but it is expensive, less reliable than therapist-assisted exercises, and not portable

- exoskeleton or prostheses – capable of total or partial assistance or replacement for patients with a high degree of disabilities, but it is expensive and often lack feedback on human biometrics

## 2.3 Anatomically-inspired Robotic Mechanisms

Intricate systems such as the human body's anatomy illustrate how muscles and tendons distribute loads throughout the entire system. Maintaining structural stability and achieving flexibility allows biological systems to adapt to external impedance while structural integrity remains. The anatomical responses to outside forces with the internal distribution of that stress enable the ability to remain operating, and structural stability [27]. However, typically robotic manipulators or systems are very stiff. This is mainly due to the components, links, and revolute joints. When compressed beyond its limits or a large mass is applied, it will always fail due to its inflexible nature [29]. These rigid systems can be classified as either a powered [3, 52] or passive system. It is important to note that a passive system does not require any power to actuate. Instead, it uses stored energy to create a

motion similar to how springs or shock absorbers help reduce stress and strain on the system [51, 53].

In a robotic system, these rigid components are beneficial being used in a known environment since it is easier to predict and know (with the informative data from the closed feedback loop) the outcome of the movements and motion of the robotic system [3]. Robotic systems comprised of these components can bear a larger load capacity. However, there are robotic systems where rather than rigid components, the system consists of malleable parts that can accommodate and readjust to an unfamiliar environment. This mannerism represents the opposite qualities of a robotics system with rigid components [58]. These robotics can apportion the weight and stress due to the flexible nature of their soft elements. While these types of robotic systems can adapt to just about any environment, they are typically unable to withstand a sizeable load-bearing capacity when they are missing a solid support system which makes it more problematic [51].

Typically, in robotic models, we see revolute joints act similarly to an anatomically correct knee joint; however, it has one main caveat: the revolute joint only has one axis of rotation. To be anatomically accurate, we must understand that within joints, there are bones within the network of muscles, tendons, and ligaments that work in unison to allow the joint to flex, move, and contort [59, 60]. To build a bio-inspired joint, we must further understand the specifics behind the anatomic joint structure, which includes understanding these elements (i.e., ligaments, tendons, muscles) that prevent the joint from suffering injuries. This is essential as the connector between compression and tension elements within the body, often overlooked in most robotic joints.

From the literature in the previous section, we found that these exoskeletons' intelligence is limited to three main features: stand, sit and step. Also, there

seems to be a significant emphasis on finding cheaper alternatives and finding a comfortable mixture between rehabilitation-based and industry-based. Concerns from the Veterans Affairs (VA) hospital revolved around the limitations of the current exoskeletons they use, which have only three main commands for walking and the system itself using parameters that are pre-loaded on the machine for individual use or adjustments. There is a fine line between people with paraplegia who need complete assisted gait control and those trying to rebuild strength with gait. Possibly the way to go is by appealing to both. There were way more implementations for exoskeletons through powered actuators than passive, assistive methods through the literature review. Another proposed solution to reduce the amount of energy exerted by the user is by exploring distributing forces through passive tensile components.

The future objective of this research is to develop an innovative and affordable lower limb prosthesis or crutch that assists each user's current limitations. Our mechanisms use techniques from tensegrity robotics [14], rigid exoskeletons [3], and the human body [27] to create a device that imitates motions from the human leg.

### 2.3.1 Hard vs. Soft Bodies

Most robotic systems are either rigid to maximize load bearing
[61, 62] or soft to optimize compliance to the environment or promote soft interactions [63]
[64]. Rigid manipulators often consist of revolute joints with stiff linkages, which are suitable for precise movements (e.g., industrial manufacturing robots); however, sudden impacts can damage the structure
[3, 65]. The advantage of stiff linkages is that under normal operating conditions,

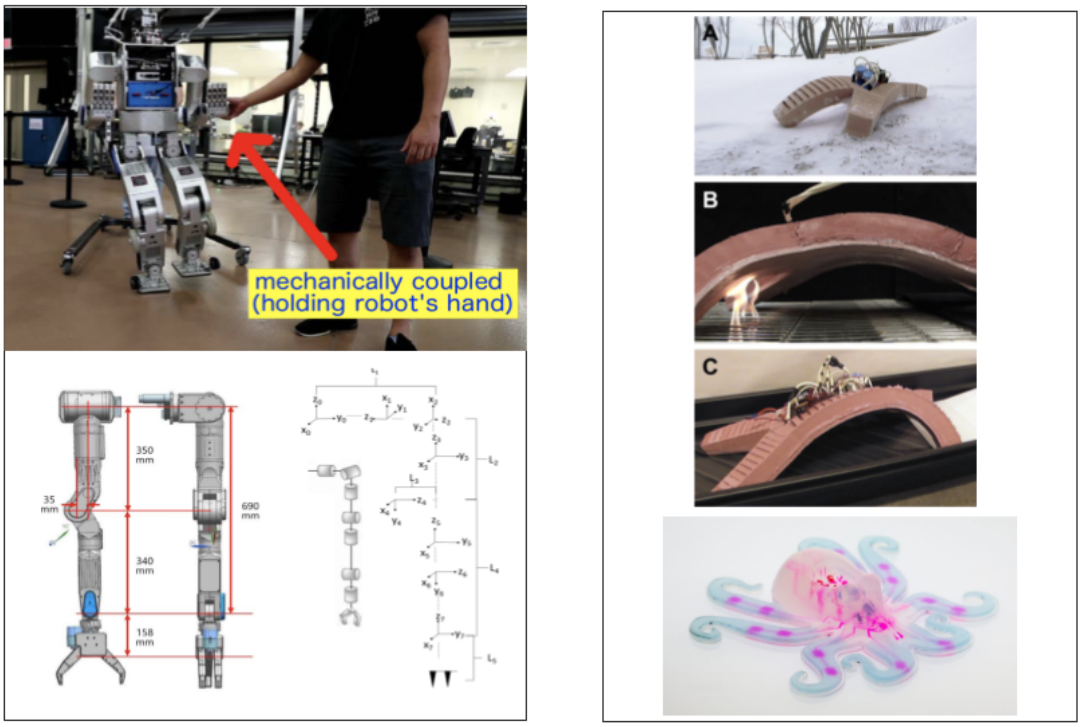


**(a)** Hard body **(b)** Soft body

**Figure 2.7:** (a) The *hard body* robotic structure showing seven actuators for a single arm [9]. (b) The *soft body* robotic structure can traverse uneven surfaces (in a variety of conditions) using pneumatic actuators [10, 11].

the behavior of these hard robotic systems is entirely predictable, leading to a manageable (ideally closed analytical form) solution for its kinematics and dynamics [3]. Soft robots distribute strain and load throughout the system adapting better to unpredictable conditions (e.g., uneven terrain, unexpected impacts). A significant limitation is the lack of a rigid support structure that lowers the load-carrying capacity of the robot [51, 58, 10]. The compromise solution often applied in assistive robotics connects rigid structural elements using compliant joints [66], or actuators [67].

### 2.3.2 Flexible-rigid Bodies

There exists a type of robotics that is a middle ground between hard and soft robotics called tensegrity. Tensegrity has rigid compression components surrounded by a network of flexible tension elements [14]. This particular type of robotics allows the ability to carry a more significant load than a soft robotic system while also allowing the flexibility of adapting to an unfamiliar environment by still distributing the stress and strain throughout the system [17, 68].


**Figure 2.8:** Tensegrity Robotics - A: Vertebra-inspired quadruped [12]. B: Wheeled spine-inspired robot (WTR) [13]. C: Tensegrity SUPERBall [14]. D: Laika quadruped robot [15]. E: Duct climbing robot (DUCTT) [16]

There have been a variety of different uses of tensegrity robots or structures in the past. Each of which had a different purpose, showcasing tensegrity's most significant advantage: it can adapt to various environments. Various fields can also apply this type of robotics. There have been tensegrity robots (Figure 2.8C) that can move by rolling as a result of relocating their center of gravity in the direction of the desired path [14, 69, 70].

As mentioned before, the significant advantages of tensegrity-inspired structures are the use of stiff, rigid elements to support the load and the elastic tension elements to deform and distribute the load throughout the entire system absorbing impacts in a similar way to passive robotics [14, 17]. There have been some

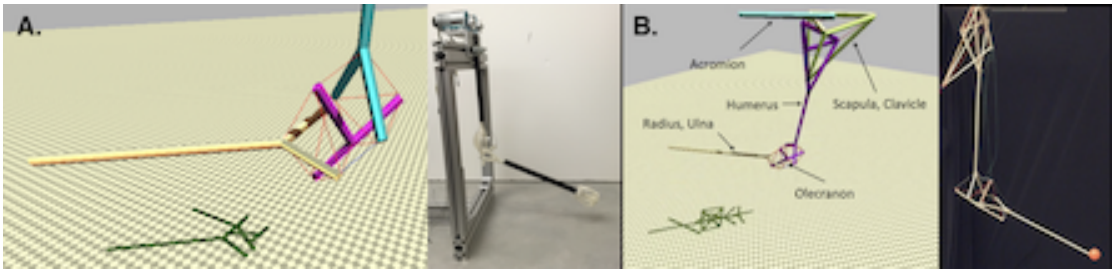


**Figure 2.9:** Joint-inspired Tensegrity - A: Elbow joint [17] B: Shoulder & Elbow joint [18]

breakthroughs in the field of bio-inspired tensegrity structures pioneered by Tom Flemons [71, 72]. Some projects include a malleable tensegrity spine whose purpose was to be able to navigate uneven surfaces [73, 74], a four-legged tensegrity structure (Figure 2.8A) that can move based on the actuation of the spine and legs [12], a tensegrity manipulator that was supposed to mimic a human "arm" [18, 59] which also lead to a soft body exoskeleton robotic suit [75], and a tensegrity structure that mimics the human "shoulder".

## 2.4 Dynamic Solvers for Biomechanics and Musculoskeletal Robotics

Biomechanics, as mentioned earlier, is the study of human movement that combines the laws of physics with concepts of engineering to address physical health and performance [76]. Human gait produces locomotion using the combination of the brain, nerves, and muscles in the lower extremities [77]. Balance and gait work uniformly as a complex sensory and motor coordination. Within this context, the gait assessment indicates levels of physical mobility and the effects of therapy or assistive technologies. A gait cycle starts at the point of initial contact of one lower extremity to the point where the same extremity touches

the ground again [77]. Skeletal-based arrangements like the human body rely on muscles and tendons to manipulate joints [27]. For gait, the human leg depends on three primary joints: hip, knee, and ankle [78]. The main objective for human motion analysis is understanding the mechanical function of the musculoskeletal systems during a given task (e.g., walking, running, etc.).

Earlier in the text, we explained how the analysis of human motion essentially understands the musculoskeletal system's mechanical function performing a given task like walking. Before high-speed computers could provide complex computations, mathematicians used non-invasive methods to calculate the nonmeasurable internal forces with inverse dynamics analysis. In the late 1900s, a common presumption used a spring to represent or measure how the muscles would displace or deform the spring. Using Hooke's law, they related the force and deformation of the spring to the muscles in the body:

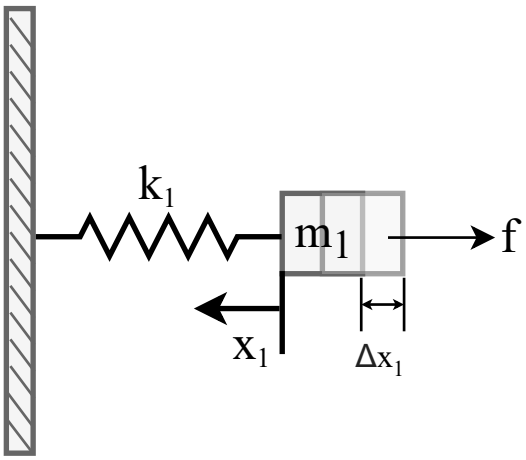


**Figure 2.10:** The forces (f from Equation 2.2) in the springs from the measured displacement of the spring (x in Equation 2.2) using Hooke's law. Before the $21^{st}$ century, human motion analysis was unable to noninvasively measure and understand the mechanical function of the musculoskeletal systems, so it all relied on mathematical modeling to estimate these quantities.

$$f = \begin{cases} k(x - l_i) + b\dot{x} & x > l_i \\ 0 & x \leq l_i \end{cases} \tag{2.1}$$

$$x = ||\mathbf{p}_{i,0} - \mathbf{p}_{i,1}|| \tag{2.2}$$

where $k$ measures the spring stiffness, $x$ represents the Euclidean distance between the spring-cable assembly, $b$ is a term for linear damping, and $l_i$ is the cable length. The variable $p$ represents the position in space for the fiber-length of the elastic elements.

Nowadays, there are many tools for handling experimental movement data and analyzing with open-source software packages (e.g., BTK [79] and OpenMA [80]), but have limitations for design optimization of custom multi-body models and lack the support for simulation development. Only a few worldwide have developed their own optimization and simulation software packages, but these privatized approaches limit the exchange of models and algorithms. Even though the field of biomechanical studies for modeling dynamics has matured over the past decade [81, 82, 83], there is an obvious need to control multi-body movements for complex structures (e.g., humanoids, human-assistive devices, etc.).

There exists many challenges listing all of the criteria to examine one dynamics simulator over another, primarily when a robot with rigid and flexible components physically interacts with the real world. Most users decide whether they want to have a strict environment obey the laws of physics (e.g., V-Rep [84]) or use it for animating virtual characters (e.g., Gazebo [85], video-games [86]) where time, computational burden, and physics can be less confining.

Literature suggested several simulation solutions for tensegrity-inspired structures. NASA Tensegrity Robotics Toolkit (NTRT) [87] simulates and controls the behavior of a tensegrity structure using C++ and MATLAB modules interfaced

with a Bullet Physics Engine [88], which was originally developed for video game animations and movies visual effects. The main advantage of using a video game engine to simulate dynamic behavior or robotics structures is the simulation speed. Bullet is a GPU-based simulation tool; the main disadvantage of this approach is that game engine solvers are primarily focused on the visual effect instead of the mathematical accuracy of the simulation. Modeling of Tensegrity Structures (MOTES) [89] is a MATLAB simulation package optimized for static analysis that determines the failure criteria using a non-linear optimization solver. ABAQUS has be used to predict the stress–strain relationship of three-dimensional tensegrity structures [90]. MOTES and ABAQUS are limited to static analysis, and we concluded OpenSim 3.0 provided kinematic and dynamic analysis that allows us to bridge robotic and human models.

Another element of discrimination is for users to adopt a simulator like Gazebo [85] or MojuCo [91]. These solvers either facilitate a connection between simulation and control over the virtual characters and the prototypes or physical systems or simulate the dynamics of complex systems without a seamless control of robotic platforms (e.g., OpenSim [23], Robotran [92]). These simulators view rigid-body structures and the joints as either constraints between bodies or a parameterized rigid-body dynamic where joints are a part of the structures. Both influence how forward/inverse dynamics are solved, and those who purely focus on simulating the dynamics of their robotics independent of physical interaction prefer newer physics engines like MuJoCo [91] that simplify contact forces as a Linear Complementarity Problems (LCP).

In this dissertation, we are primarily concerned with building multi-body complex structures similar to the musculoskeletal connections in the human body. All of the forces in OpenSim are a function of positions and velocities making the use

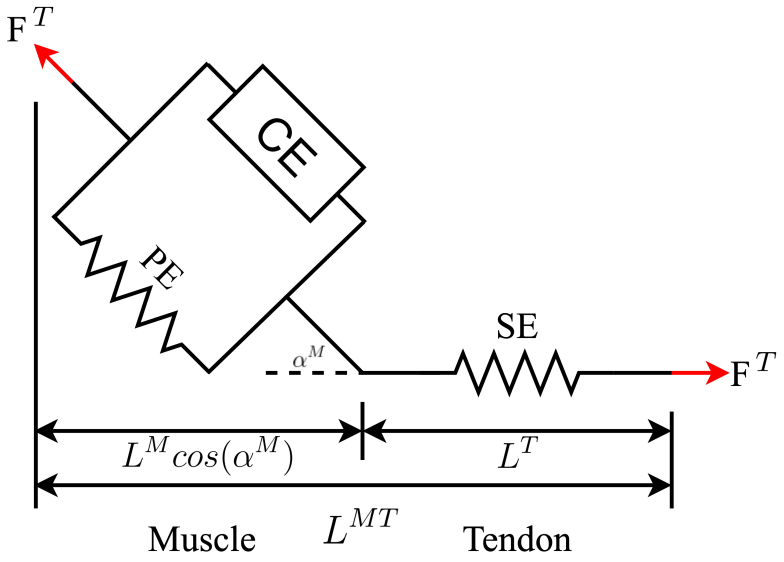


**Figure 2.11:** This schematic represents the elements of a single muscle in series with an elastic tendon ($F^{MT}$ from Equation 2.3) in OpenSim. $F^T$ is the force or tension (red arrow), and L is length with superscripts referring to M, the muscle, T, the tendon, or MT, the whole contracting element. $\alpha$ is the pennation angle for the mean orientation of muscle fibers in a muscle with respect to the line of action.

of sensors like IMUs beneficial. The dynamic equations for these active contracting elements assume that the muscle, $F^M$, and tendon $F^T$ are in equilibrium and massless (only under Newton's third law), at all times [24].

$$F^{MT} = F^T + F^M cos(\alpha) \tag{2.3}$$

The inverse kinematic, angle generation, and inverse dynamic analysis built-in with OpenSim solvers make it the ideal tool for introducing an alternative data acquisition method with a reliable platform [93, 94, 95]. Since OpenSim is one of the most widely used open-source biomechanics platforms, we demonstrate how it can play a crucial role in human biomechanics and robotic applications.

## 2.5 Quantitative Motion Tracking Systems

Quantitative movement analysis plays an essential role in understanding the process of body movement [96, 97], rehabilitative research [98], the performance of athletes
[99], and overall dynamic behavior. Model-based approaches define movement patterns and analyze high precision measurement techniques
[100]. The most popular form of measurement systems use camera-based (optical) approaches that track markers with either active (ultrasound) or passive (optical) placed on a subject following the Joint Coordinate System (JCS) presented by the International Society of Biomechanics (ISB) [101]. Marker placements require a constrained location and orientation setup (i.e., cameras mounted and directed at the subject), resulting in high accuracy for spatial positions of the markers [96]. Miniaturization of electronic devices allows wearable miniature sensors, such as an inertial measurement unit (IMU), to record quantitative movement data or predict system kinematics and dynamics in real-time using embedded hardware and sensor-fusion algorithms (e.g., Kalman-filters). The advantage of this approach is not limited by the use of a room-bounded localization system [102, 103, 104]. Studies have tracked the movement of a sitting knee and ankle flexion captured by IMU sensors about an optical motion tracking system yielding an RSME of 4° [105]. For more complex movements like gait, Vargas et. al used optical motion capture with a universal goniometer to calibrate the JCS for IMUs resulting in an RSME of 15.61° [106], where our maximum RSME of 10.21° is comparable.

Tracking the motion of human subjects performing gait can be done in various ways. Still, the most common include: optically monitoring marker trajectory [98, 21, 22] or wearable IMU sensors using sensor-fusion algorithms to record angular displacements [107, 108]. The majority of the subject data in this work

was provided by the public databases from Moissenet[1] , and Horst[2] that relied on optical marker-tracking systems [21, 76]. The additional data set for training purposes was from custom IMU sensors [109] collected under an IRB Exemption at UC Santa Cruz.

### 2.5.1 Optical Motion Capture (OMC)

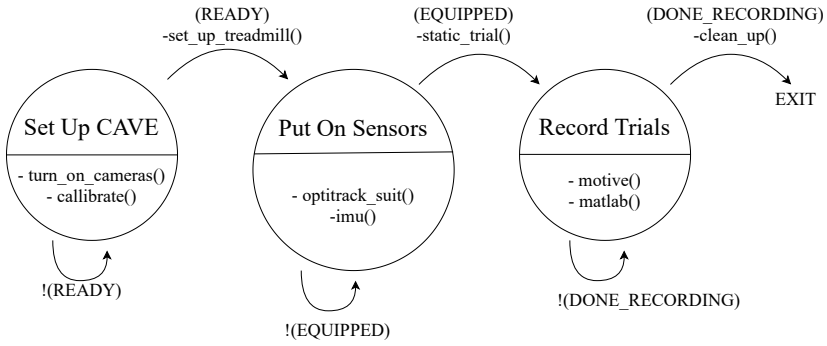


**Figure 2.12:** This diagrams a high-level process for preparing each experiment with both motion captures and importing them into the musculoskeletal models provided by OpenSim.

The most mature and traditional form of capturing body kinematics and importing it into biomechanic kinematic and dynamic solvers uses optical motion capture systems. These setups require a non-portable, room-bounded configuration viewed as the 'gold' standard in terms of joint angles, angular velocities, and moments at select musculoskeletal systems.

For my proposes, I used reflective markers placed on each subject (flexible-rigid structure or human body) where multiple cameras. In the DANSER Lab, we had a 3.5 (m) × 3.5 (m) × 3.5 (m) test area was instrumented with eight OptiTrack Prime 13 Watt infrared cameras that track retro-reflective markers at

[1]The public database provided by Moissenet et. al [21]: `https://figshare.com/articles/A_multimodal_dataset_of_human_gait_at_different_walking_speeds/7734767`

[2]The public database provided by Horst et. al [76]: `https://data.mendeley.com/datasets/svx74xcrjr/3`

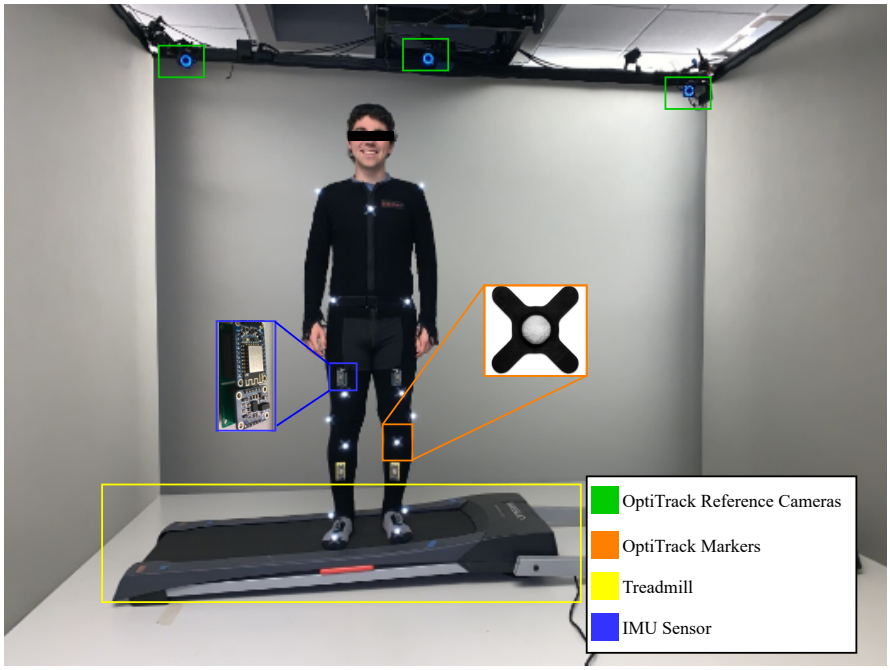


**Figure 2.13:** The setup of both OMC and IMC systems (Figure 2.13) of a user before the walking experiment. The configuration allowed direct and simultaneous comparison for both systems.

a frame rate of 120 Hz. Then the Motive post-processing package recorded the kinematic behavior of the robot and human subjects performing any prescribed motions. We imported the position of the markers in the OpenSim 3.0's inverse kinematics (IK) package to compute the torques and angles (Figure 3.2), which was further imported in the forward dynamics (FD) tool to generate an actuation scheme (Figure 4.9) that manipulates each active element.

### 2.5.2 Inertial Motion Capture (IMC)

The difference between camera-based and IMU-based systems are the methods for recording: camera-based use spatial locations of markers, and IMU-based rely on physical manipulation and orientation changes in space to derive acceleration vectors [104]. Recent advances in wearable measurement systems such as inertial

motion capture (IMC) systems have the potential to monitor body kinematics in diverse environments (e.g., virtual reality, clinical, or sports-related research). For example, IMUs have demonstrated a strong tool for assessing joint kinematics of the upper extremities [110, 111], lower extremities [112, 111], and spine [113] have been assessed for short periods of time with fairly non-complex movements. The direct numerical assessments lacking in this field addressed in this dissertation include:

- comparisons using **OMC vs. IMC** systems
- the use of **different models** with intricate movements
- extracting measurements to **benchmark dynamic behavior** of flexible-rigid structures and human joints

## 2.6 Applied Machine Learning for Motion Tracking

Complex biomechanic simulation environments (e.g., OpenSim [24], bioMechZoo [114]) focus on musculoskeletal models performing kinematic estimations. The inverse kinematics (IK) and inverse dynamic (ID) tools provided by OpenSim are used as a viable solution for enhancing gait phase classification by outputting a set of required joint-torques to transition between phases.

To better understand the large databases produced from motion capture systems or simulation environments, machine learning is critical for our gait assessment [115, 116, 117]. The development of classification models to determine phases of gait for a diverse group of subjects has not been popular due to the difficult task of generalizing the wide variety of human locomotion [118]. Instead, most

complex models focus on pathological gait recognition (e.g., detecting disabilities that affect gait) [119], or the stance-swing phase of gait for classification [118]. Often machine learning approaches are viewed as "black boxes", that can solve any problem. However, the unwise choice of parameters can lead to ambiguous decisions, or erroneous predictions [76]. As a reliable approach, literature has focused on gait recognition, or detection [116, 119] as the primary machine learning classification to facilitate automated discrepancies for fall detection or changes in activities (i.e., transitioning from walking to running) [77]. In Chapter 5.4, we go into detail on common techniques for preparing data (e.g., cross-validation [120], GridSearch [121]) to train several different types of classification algorithms (e.g., K-nearest neighbors, Random Forest, etc.) [122, 123].

# Chapter 3

# Modeling and Simulation

## 3.1 Introduction

Simulators for biomechanical studies tend to be offline to analyze complex structures and whole-body movements. These simulators are usually open-sourced, but they do not provide a seamless connection between simulations and real-world applications. It is certainly difficult to enumerate all the criteria to choose a dynamics simulator, especially when developers advertise everything as a “supported feature". Reasons as to why it is difficult include:

- Extensive comparisons require access to source code but not all software is open-sourced
- All open-sourced simulators run on different computer architectures
- Not all simulators have extensive documentation and examples

There exists a variety of software packages that rely on specific hardware and camera-based configurations [124, 125] to model kinematic behavior, but this can cost a lot of money. Alternatively, packages independent of hardware configurations [114, 126] use complex solvers to predict movement.

## 3.2 Simulating Flexible-rigid Mechanisms & Musculoskeletal Models

### 3.2.1 Introduction

The benefits of studying the musculoskeletal tools for biomechanical structures are undeniable: an understanding of rehabilitative progress, predicting outcomes of surgeries, and optimizing assistive devices [126]. To achieve the design of the presented flexible-rigid manipulators, we explored the overlap between tensegrity structures and the anatomy of the human body. Human joints are structurally and functionally intricate systems consisting of bones, muscles, and connective tissue. Joints are durable and adaptable to change, allowing humans to react to outside impedances while maintaining structural equilibrium. Through flexible-rigid mechanisms, the primary attributes are the ability to absorb non-axial impacts, and flex [127] similarly to the musculoskeletal systems.

### 3.2.2 Rapid Kinematic Solvers

As noted earlier, finding a simulator that supports a seamless connection with the physical world is difficult, especially for robotic systems with multi-body dynamics. Although the advancements for modeling the dynamic behavior of such systems are better, the need to control whole-body movements such as humanoids or assistive technology poses many challenges for rapidly prototyping controllers and designs:

1. **speed vs.complexity** - solvers have to compute dynamics and converge to physically reliable solutions quickly

2. **numerical stability** - extremely limiting for real-time applications

3. **modeling** - simulate rigid and soft bodies contact with different environments and materials

These criteria shift the solvers' expectations from animation or virtual characters towards describing and visualizing multi-body systems, which is why we leaned towards Bullet-based physics engines in our initial approach. NASA created a simulation tool called the NASA's Tensegrity Robotics Toolkit (NTRT) to help designers who would like to simulate their designs without being computationally heavy. Therefore, in this dissertation, the simulation process starts by analyzing the behavior of flexible-rigid designs in the NTRT simulation environment.

The first models assume that the compression elements are rigid and actuated by elastic, flexible cables. Early designs of the system were simulated using NTRT [14, 128], which uses Bullet, a physics engine to simulate contacts and impacts between elastic and rigid body dynamics [18]. This simulation environment uses a Cartesian mapping system to describe the geometrical shape of a tensegrity structure, Euler-Lagrange formulation to describe the dynamics, and Hooke's law to predict the elastic forces (Equation 2.2) developed inside cables [73].

The traditional approach with NTRT was unable to accurately initialize the density of rods and cable characteristics due to the unnatural behavior (i.e., density of rods was fixed at $\frac{k}{m^2}$ not $\frac{k}{m^3}$). This constraint led us to use complex biomechanical solvers for simulating the multi-body dynamic modeling and successfully did it within a complex biomechanic simulation environment. This work is significant, as custom models, specifically multi-body flexible-rigid mechanisms, have never been accomplished within this open-source environment. In the section below, we describe our work using NTRT and OpenSim.

### 3.2.3 Complex Bio-mechanical Solvers

Open-source packages like BTK [79], MujoCu
[129], and OpenMA [80] provide tools for collecting and analyzing experimental movement data. Still, it lacks the closed-form expression for faster computation or limits the exchange of models and algorithms. OpenSim 3.0 [23] is an open-source simulation environment developed by the NIH Center for Biomedical Computation at Stanford University (Simbios) that focuses on analyzing and predicting the biomechanics of the human body independent from hardware. I found that OpenSim provides an open-source, extensible and complex platform where users can span three crucial topics:

1. **build and manipulate** flexible-rigid and bio-mechanical models
2. **simulate** musculoskeletal dynamics for optimizing the design process
3. **predict** movements and adaptations without performing any experiments

Options for analysis include joint kinematics, muscle activation, and movement dynamics on provided or custom models for musculoskeletal models. Traditionally, OpenSim uses an order of operations that pairs models with the experimentally recorded marker positions for the locations of virtual markers placed on specific model body segments. The *Scaling Tool* generates subject-specific model instances (e.g., height, weight, etc.), while the *Inverse Kinematics (IK) Tool* extracts model-defined joint angles to create movement. Each model is represented by an XML-structured format that contains bodies, constraints, forces, and marker sets that are all accessible through the SimTK API call [130].

The *Gait2345_Simbody* model was adapted by altering the file and removing components (e.g., bones, muscles, etc.) into a suspended human leg to reproduce

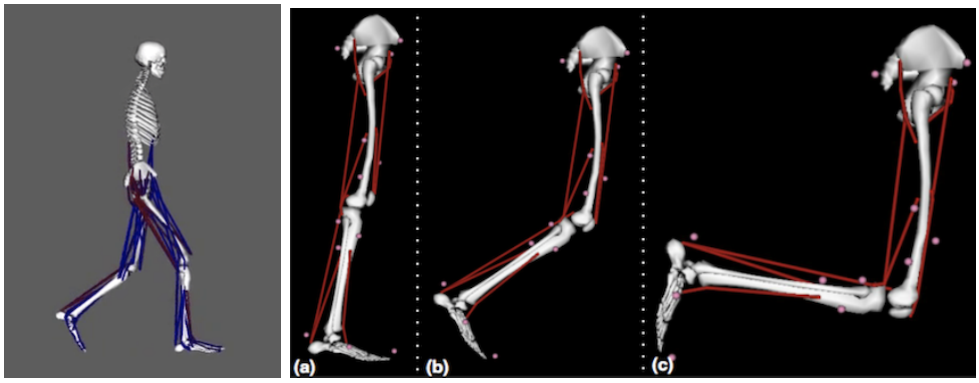


**Figure 3.1:** Transition from dissecting the *Gait2345_Simbody* musculoskeletal model and simplifying into the most prominently used muscles for knee flexion and in-place gait.

a target hinged gait pattern with similar constraints as the physical model (Figure 3.1). The "active" elements capable of actuation were modeled as muscles using OpenSim 3.0's *Thelen* muscle model [131], and the "passive" tensile elements as ligaments. This Hill-type muscular-tendon contraction mechanics model consists of several elastic elements connected in series and in parallel, where the active force-length relationship is assumed to be Gaussian. The equilibrium muscle model [126] consists of three main components: contractile elements $F_{CE}$, parallel elements $F_{PE}$ and series elements $F_{SE}$. The active, $F_A$, and passive, $F_P$, components in our models follow similar muscle-tension ratios to represent varying levels of force with length relying on a modified version of the equation given from the *Thelen2003Muscle* model [131]:

$$\dot{l}^M = F_v^{-1}\left(\frac{\frac{F_P(l^T)}{cos(\alpha)} - F_P(l^M)}{a(t) \cdot F_A(l^M)}\right) \tag{3.1}$$

$$\dot{l}^M = F_v^{-1}\left(\frac{F_P(l^T) - F_P(l^M)cos(\alpha)}{F_A(l^M)a(t)}\right)$$

$$\dot{l}^M = \frac{F_P}{F_v F_A(l^M)}\left(\frac{l^T - l^M cos(\alpha)}{a(t)}\right) \tag{3.2}$$

**Table 3.1:** Muscle element specific parameters used for simulation.

| **Muscle Element** | $\boldsymbol{F_0^M}$ **(N)** | $\boldsymbol{L_0^M}$ **(m)** | $\boldsymbol{L_s^T}$ | $\boldsymbol{\alpha^M}$ **(deg)** |
|---|---|---|---|---|
| Active | 100 | 0.128 | 1.8 | <1 |
| Thelen [131] | 1400 | 0.090 | 2.4 | 7 |

$F_0^M$ maximum isometric force; $L_0^M$ optimal fiber length; $L_s^T$ max tendon slack length in relation to muscle length; $\alpha^M$ muscle fiber pennation angle.

To predict the force velocity relationship using the equation above, we used data available in the published literature (Table 3.1 [126, 131]):

- Muscle activation value $a(t)$;
- Normalized length of the unit muscle $l^M$ and tendon $l^T$;
- Normalized velocity of the unit muscle $F_v$;
- Maximum Pennation Angle $\alpha$.

This approach extends the conventional acquisition methods and analysis to both native and custom musculoskeletal models in the OpenSim environment [20, 132]. By importing each configuration and marker set file into the Scaling Tool (Figure 3.2) to adapt to different sized users and models easily (e.g., varying lengths, masses, etc.). In most cases, the Scaling Tool matches the physical prototype and the participant according to the reflective infrared markers placed on both subjects with mm precision. The calibration process required a static file with markers matching the simulated model's exact placement and the physical subject.

Typically, OpenSim relies on coordinate data from participants wearing specialized suits with numerous markers allowing the motion capture system to reliably track the positions of these markers with high precision [130, 23]. Instead the

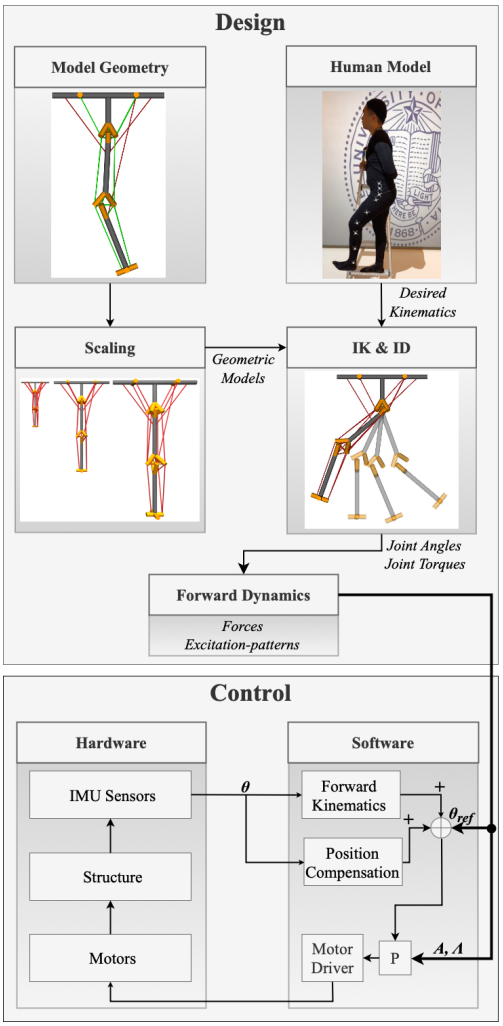


**Figure 3.2:** Flowchart illustrating the early design and simulation process.

Inverse Kinematics (IK) tool in OpenSim was used to analyze the recorded motion of the subjects in all of the experiments. It matches a set of marker coordinates recorded over time from the leg in motion to markers on the model and calculates the closest approximation of each joint angle of the model to reproduce the movement in the simulation. Reflective markers were placed on each rigid body of our subjects. Identical markers were placed on the model in OpenSim to match the position of the physical markers. Mathematically, the closest approximation of joint angles is expressed as a weighted least squares problem that minimizes both

marker and coordinate errors.

$$err_m = \sum_{u \epsilon m} \omega_u \left\| z_u^{exp} - z_u(q) \right\|^2 \tag{3.3}$$

$$err_c = \sum_{l \epsilon k} \tau_l (q_l^{exp} - q_l)^2 \tag{3.4}$$

$$\min_q \left[ err_m + err_c \right] \tag{3.5}$$

where $l$ and $q$ is the vector of generalized coordinates being solved for, $k$ stands for unprescribed coordinates, $z_u^{exp}$ is the experimental position of marker $u$, $q_l = q_l^{exp}$ for all prescribed coordinates, $m$ for markers coordinates, and $q_l^{exp}$ is the experimental value for coordinate $l$, $x_u(q)$ is the position of the corresponding model marker (which depends on the coordinate values). $\omega$ and $\tau$ are marker and coordinate weights, respectively [126].

For simulating the motion of models without inputs external to the program, the Forward Dynamics (FD) tool interprets approximated muscle excitation, along with all other forces acting on the model's bodies to simulate the model's physical behavior in the affected space. To validate a purely simulated motion of the leg, we compare the behavior of the physical prototype (Figure 5.3). The data from the simulation is a way to confirm the mechanics of the projected behavior of the prototype. This can estimate kinematic behavior and apply it to the structure. FD estimates the acceleration and displacement of the coordinates of the OpenSim modeled leg as forces are applied to it via the muscles. The accelerations are found by integrating the model's musculoskeletal dynamical equations:

1. $\tau_m = [R(q)] f(a, l, \dot{l})$ for moment due to muscle forces
2. $\dot{l} = \Lambda(a, l, q, \dot{q})$ for muscle contraction dynamics
3. $\dot{a} = A(a, x)$ for muscle activation dynamics

These equations root from the classical equations of motion [126] written together in the following form:

$$\ddot{x} = [W(x)]^{-1}(N + M(x, \dot{x}) + G(x) + F) \tag{3.6}$$

1. $x$ for the vector of generalized positions
2. $\ddot{x}$ for the vector of accelerations
3. $\dot{x}$ for the vector of velocities
4. $N$ for the vector of generalized forces
5. $[W(x)]^{-1}$ for the inverse of the mass matrix
6. $M(x, \dot{x})$ for the vector of Coriolis and centrifugal forces
7. $G(x)$ is the vector of gravitational forces
8. $F$ is the vector for optional external forces applied to the model

s $5^{th}$-order Runge-Kutta-Feldberg integrator to solve for coordinate trajectories over the specified time interval in these dynamical equations [126]. Running FD produced a motion that expresses the resulting simulated movement in terms of angles for each set of joints.

The last tool worth mentioning in this dissertation is the Inverse Dynamics (ID) tool. It began by importing a motion file (typically from IK) into ID to approximate forces, moments, and torques experienced at the joints of the model through a commonly used equation:

$$(R(\theta) + I(\theta))\ddot{\theta} + C(\theta, \dot{\theta})\dot{\theta} + G(\theta) = T(\theta) \tag{3.7}$$

where $R(\theta)$ are the reaction forces due to the model's interaction with the environment, $I(\theta)$ represents the inertial matrix, $C(\theta, \dot{\theta})$ represents the Coriolis and centrifuge matrix, $G(\theta)$ represents the gravitational matrix, and $T(\theta)$ represents the forces applied to the system with angular acceleration ($\ddot{\theta}$), velocity ($\dot{\theta}$) and joint angle as $\theta$ [126]. ID uses positions, velocities and acceleration solved with calls to OpenSim APIs (*OpenSim::InverseKinematicsSolver* and *OpenSim::InverseDynamicsSolver*) that interpret joint angles operated on single time frames to determine joint moments. The simulated platform and its constraints found from Hamner et. al [133] relied on the acceleration analysis to emulate the ground reaction forces and moments. ID serves as an impactful method for comprehensively estimating models based on kinematic trajectories and the simulated ground. The induced accelerations solved by IK use the foot-ground contact to estimate how muscles, gravity, and velocity-related forces contribute to ground reaction forces within the OpenSim environment. Since this system includes a comprehensive dynamic relationship for each joint, the solvers trained my algorithms further discussed in later Chapters.

## 3.3 Model Selection

### 3.3.1 Introduction

The first application of these flexible-rigid robotics imitates the human body rooted from the tensegrity elbow joint influenced by Graham Scarr [17, 134]. This mechanism presented a biologically inspired human elbow with a lightweight, multi-axis compliant joint. The physical prototype of our elbow consists of compression elements emulating bones and tensile parts imitating muscles excitation absorbed by tendon and ligaments. This innovative solution was able to demon-

strate the ability to rotate the structure around two axes independently by contracting and releasing tension elements to generate pitch and yaw movement [17].

As the prototypes increase in complexity, starting with the knee-inspired, then the gait-inspired (hip and knee joints), and the self-standing and weight-bearing designs (hip, knee, and ankle joints), I established a set of steps towards the methodology of creating hybrid-based (combination of hard and soft elements) robotics. Each model follows the parent-child dependencies between bodies which include: multiple degrees of freedom, muscle compartments that are capable of evaluating kinematics, muscle forces, and joint moments. The movement of models depends on the chain of each body segment and how it follows the relative motion of each child in respect to the parent. The joint coordinates determine manipulation of joints, or angle values, in proximal to distal order [135]. This parent-child hierarchy became the standard for how the technique interpreted joint-angle measurements from the data acquisition systems (Equation 3.8) discussed later in this chapter.

### 3.3.2 Knee-inspired Flexible-rigid Structure

The first set of models (Figure 3.3) were designed and simulated through NASA's Tensegrity Robotics Toolkit (NTRT) for rapid modeling, and efficient comparisons between the biological accuracy between each iteration
[18, 14, 128]. Tensegrity robotics proved its ability to act as a flexible manipulator with models focused on illustrating a degree of freedom similar to the human body from the bio-mimetic behaviors (shoulder model) and kinematic redundancy (tetrahedrons model) shown in Figure 2.9 [59]. As the progression of achieving biologically-inspired flexural joints furthered, the research shifted from imitating the human arm into the human leg. Underlying the critical fundamentals from the

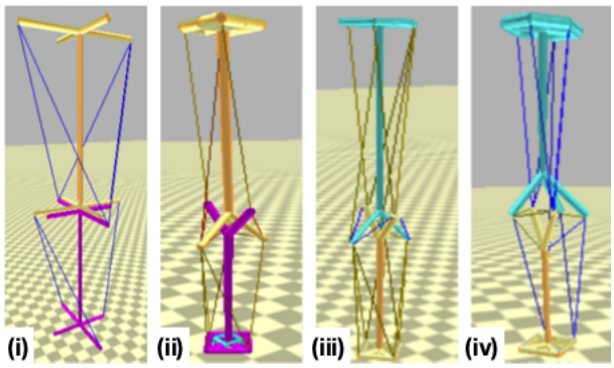


**Figure 3.3:** First iteration (starting on the left progressing to the right) was a simple leg model only capable of standing. The next was more accurately representing the muscles in the leg. The third was an extension of the previous with even more biologically-inspired muscle and ligament connections within the muscle system. The last was capable of knee flexion by contracting and relaxing the hamstring-inspired set of muscles in a hinged position.

shoulder and elbow flexural joint models, the progression of designs represents the level of complexity needed to maintain structural stability and achieve similar biological mechanics to the human leg. The NTRT simulation environment provided a method of approximating kinematics with these early designs. The configuration for each model (Figure 3.3) used the Cartesian mapping system where each node connected to rod-like components. From the final iteration, the hung model was developed into two different joint prototypes. In the first prototype, the angle between the individual branches forming the joint is shaped like an isosceles triangle. The range of motion seemed restricted since the compression elements touched at full flexion. The minor adjustment into an equilateral triangle led to a significant improvement in steady flexion without compression elements making contact with the second alteration.

Once the first model could maintain an environment with non-contact elements within a mesh of elastic components, the models were prototyped with AutoDesk Fusion 360, which led to our first physical prototype (Figure 4.1). Learning through the iteration of modeling and design from previous tensegrity manipula-

tors led to the latest structure configurations as intricate and biologically accurate to the human leg. With the full intent of furthering the newest flexural joints to be able to imitate a typical motion of gait or remain standing, the design began by first solving the knee joint [136] then the hip joint.

### 3.3.3 Gait-inspired Flexible-rigid Structure

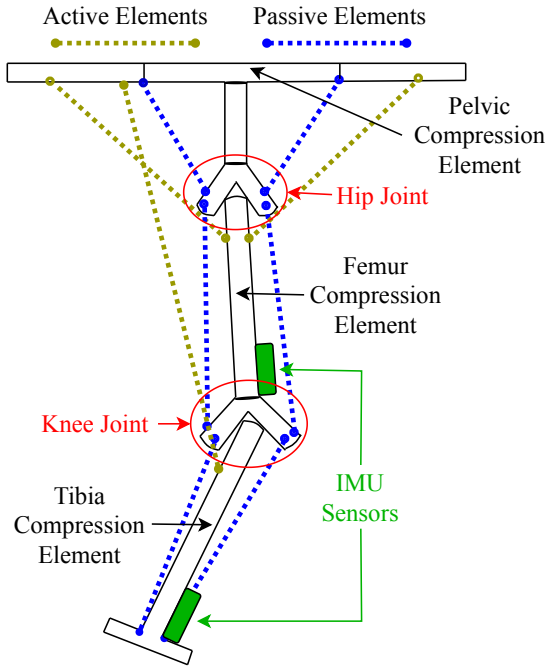


**Figure 3.4:** The proposed system, consisting of three compression elements ("Tibia","Femur" and "Pelvis") and two flexural joints ("Knee" and "Hip") controlled by three active tensile elements.

Expanding a similar modeling process for our knee flexing design, we applied it to a hanging model with an additional hip joint and used OpenSim for a more realistic representation. The suspended gait-inspired model actuates three groups of virtual muscles (equivalent to the quadriceps, the hamstring, and hip flex muscle groups) that activate both hip's and knee's flexion and extension. This custom six-degree-of-freedom leg model (Figure 3.4) was built in OpenSim showcasing the

passive tensile elements in the physical model shown in Figure 4.4a and 4.5a were approximated in the simulation by “passive muscles”. The *passive* tensile elements in the model used both *Thelen2003* muscles with zero ability to produce force and ligaments that prevented the structure from collapsing. The active muscles approximated the physical model’s active tensile elements (actuation cables).

The compression elements in the physical model used welded jointed rigid bodies (bones in a biomechanics OpenSim simulation) to form the “T" and “Y" shaped connectors (Figure 4.2) at the end of compression elements. Based on a human leg, the model’s dimensions are scaled up to visualize the knee easily, and hip flexion as the model undergoes various stages of gait. The structure’s weight is programmatically adjusted to the mass of the material in the prototyped, which ended up being carbon fiber rods. The model was actuated by exciting the active tensile elements, and we compared the predicted kinematic behavior of the system with one of the human legs. The predictions were used to design the physical prototype of the manipulator.

First among the two custom models was a suspended single-degree-of-freedom knee joint outfitted with a single actuating muscle acting in place of the biological Biceps Femoris. The choice of a single muscle was made for simplicity and ease of muscle placement on an initial prototyped physical structure. Due to the muscle placement, the structure used it solely for extension of the knee joint towards the negative range-of-motion limit, whilst gravity was responsible for knee flexion. Additionally, to ensure that the model’s joint coordinates obeyed physical constraints (i.e: the joints did not exceed their maximum range-of-motion), a coordinate limiting force was placed upon the joint, which generated a force that acted to limit the range-of-motion of the lower leg coordinate should it tend to exceed the maximum value. Although this restoring force could slightly deviate

the simulated motion of the model from the desired hinged gait, it was deemed necessary to ensure the model obeyed the physical limitations of the proposed model's movement. This particular model helped test the muscle's exertion force to place the leg's lower body into the necessary positions to achieve a desired hinged gait.

The second of the two models was a more complex structure with six-degree-of-freedom hip and knee joints actuated by three distinct muscles, each representing the Quadriceps, Bicep Femoris, and Hip Flexor groups respectively. Together the three muscles fully controlled hip and knee flexion and extension without the aid of gravity. To solidify the model's constraints, two more coordinate limiting forces were applied to the knee and hip joints to ensure they complied with the physical limitations of our proposed design. This particular model assisted in applying the findings from the first knee-only model with all of the influence of the dynamics from a moving upper leg. Moreover, the model was more reflective of a biological leg and provided more application for the results considering the goal was a biologically-inspired flexible-rigid joint.

### 3.3.4 Self-stabilizing Flexible-rigid Structure

The most recent flexible-rigid design (Figure 3.6) maintains structural integrity in the upright position due to the distribution of strain amongst the ankle, knee, and hip joints within. The lower half of the human body consists of many joints, and this design mirrors the hip, knee, and ankle joint along the sagittal axis, enduring a descent. The hip is capable of a variety of manipulated motions, including adduction, abduction, and extension—the knee joint flexes along one axis of rotation similar to revolute joints in rigid robotic systems. Plantar and dorsiflexion produced by the ankle joints also maintain innate flexibility to adhere

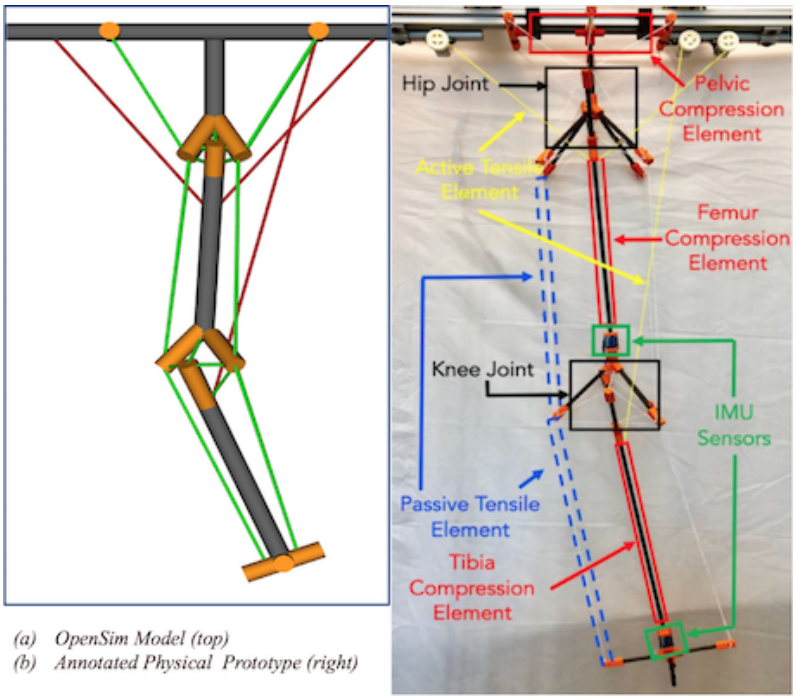


**Figure 3.5:** Side by side comparison to visually demonstrate the accuracy between OpenSim and Prototype.

to uneven terrain when performing gait [137].

The dependent muscle-inspired cables were relocated for bending the joints within the model along the forward axis in the human leg in place of the tibialis, calf, hamstring, and quadriceps (Figure 3.6 (Left)). The active elements in the OpenSim model follow calf and hamstring into a pair of muscles, and the tibialis and hamstring as the two antagonistic muscles. The two calf muscles pull the tibia body of the leg toward the ground, while the tibialis muscles pull the ankle angle back to an upright position. The two hamstring muscles keep the knee joint within its range of motion while leaning forward. The hip joint is held within its range of motion by passive elements and does not need active actuation for this specific experiment. Previous studies of muscle activation within the human leg during a squatting motion confirm the placement and excitations of the muscles in the OpenSim model [137, 138]. The hip joint is kept within its

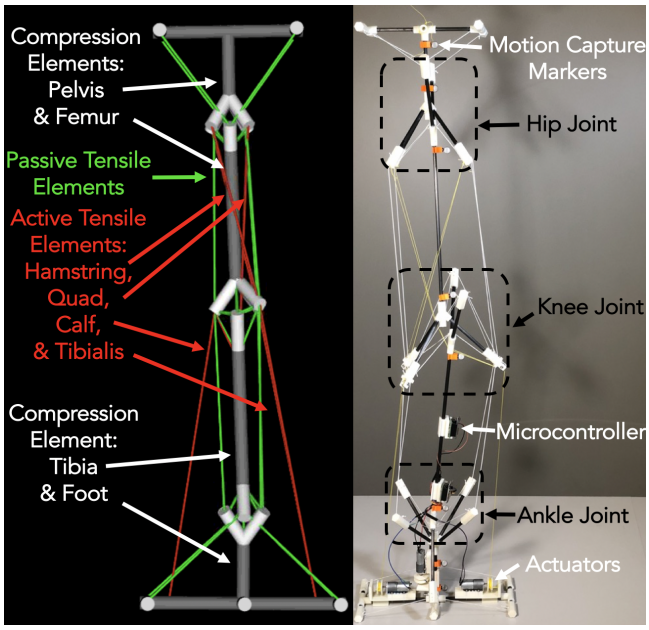


**Figure 3.6:** (Left) Proposed lower extremity joint inspired flexible-rigid design in Simulation - OpenSim and (right) physical prototype. The passive elements are represented on the left in green and on the right in white. These passive elements can be thought of as ligaments in the body. The active cables are represented in red on the left. These can be loosely compared to muscles in the human body.

range of motion by passive elements and does not need active actuation for the simulated experiment. Likewise, the lateral movement of the joints is restricted by the passive components.

For simulating the motion of models without inputs external to the program, the Forward Dynamics (FD) tool interprets approximated muscle excitation, along with all other forces acting on the model's bodies to simulate the model's physical behavior in the affected space. To validate a purely simulated motion of the leg, one can compare the behavior of the physical prototype (Figure 3.7). The data from the simulation is a way to confirm the mechanics of the projected behavior of the lower extremity tensegrity structure. With this information, the estimated kinematic behavior can be applied to the physical tensegrity structure. FD models the acceleration and displacement of the coordinates of the OpenSim

modeled leg as forces are applied to it via the muscles. The set of excitations found resulted in a similar motion to the experimental data. Evaluation from the simulation provides validation of kinematic behavior and an approximation towards producing the physical prototype. This form of calibration resulted in the combination of exertions that allowed the tensegrity design to successfully stand, which led to the experimentation of initiating a descent.

### 3.3.5 Human Subjects

For analyzing the kinematic and dynamic behavior of models with OpenSim, the gait-inspired [20] and standing [132] flexible-rigid models were mentioned. The last model for human subjects provided by OpenSim was the *Gait2345_Simbody* model. This model features 92 musculotendon actuators representing 76 lower extremities and torso muscles, where the unscaled version represents a subject about 1.8 m tall and has a mass of 75.16 kg. It contains all of the required bones and musculoskeletal connections in the human to facilitate gait. As mentioned previously, each model follows an XML-structured format that contains the marker sets to precisely translate the physical world into the simulation environment. This part of the file was essential to develop, calibrate and compare the biometric pipeline in this dissertation.

## 3.4 Biomechanic Analysis Pipeline

### 3.4.1 Introduction

As stated in Chapter 3, the modeling and simulation deal with computational modeling and simulation of the flexible-rigid designs and human musculoskeletal system. These models and simulations are essential because they can reveal inter-

nal muscle forces and joint loads in various scenarios such as standing, squatting, and walking.

This work created a low-cost acquisition method and pipeline to analyze kinematics and dynamics of both robotic and human motion using OpenSim and IMUs without relying on an optical MoCap system for data acquisition (Algorithm 2). The approach applies Algorithm 2 to track motion and compare wearable IMU with optical MoCap systems in a reliable simulation environment. The IMU method of acquisition uses orientation information to perform joint angle reconstruction [139, 140] to validate the calculations against optical measurement systems. Simulating the kinematic and dynamic measurements between humans and custom models proposes a better understanding of the relationship between mobility devices (e.g., prostheses, exoskeletons) and the human user to improve future designs. The sections below describe the experimental setup, data-acquisition process, and joint-angle measurements from each motion. In Chapter 5, I compare the difference in measurements of each joint between IMU and commercial optical MoCap systems and discuss the potential advantages of IMUs compared to an optical MoCap based system.

### 3.4.2 Data-acquisition

The difference between camera-based and IMU-based systems are the methods for recording: camera-based use spatial locations of markers, and IMU-based rely on physical manipulation and orientation changes in space to derive acceleration vectors [104]. The inverse kinematic, angle generation, and inverse dynamic analysis built-in with OpenSim solvers make it the ideal tool for introducing an alternative data acquisition method with a reliable platform [93, 94, 95]. Since OpenSim is one of the most widely used open-source biomechanics platforms, it

demonstrates that both forms of data acquisition can play a crucial role in human biomechanics and robotic applications.

**Algorithm 1:** Establish TCP connection and send joint angles to host device.

```
Result: θ_{h_xyz}, θ_{k_xyz} & θ_{a_xyz} measurements
Initialization: run host to open TCP port connections;
for all joints
    client connect → host IP;
    if ACK connection then
        while buffer not full
            measure θ_x, θ_y, θ_z at 100 Hz;
            if packet size ≈ memory allocation then
                push packet onto the buffer;
        end
        while buffer not empty
            pop off packet from the buffer;
            packet → host IP;
            if ACK packet received then
                continue;
            else
                re-send packet → host;
            end
        end
    else if no ACK connection then
        search for host IP;
    else
        connection loss → reconnect to host IP;
    end
end
```

The TCP protocol was used to ensure a fast, reliable connection for wireless communication with a host computer. Once the host or the IMUs get an acknowledgment (ACK), this guarantees a successful transmission of IMU data. Algorithm 1 starts with establishing a synchronous connection for each sensor for data acquisition. This way, experiments can away from the immobile camera-based environments of motion capture systems. IMUs include sensors (e.g., accelerometers, gyroscopes, magnetometers) and apply sensor-fusion algorithms to

compute angles in the x, y, and z dimensional axes.

The BNO055 Inertial Measurement Unit (IMU) is an orientation sensor capable of recording 9 degrees of freedom (Table 3.2) with robotics being one of its typical applications [94, 141]. The IMU was enhanced with sensor-fusion algorithms (the Madgwick sensor fusion filter [140]) to compute angles in the x, y, and z dimensional axes. For fast and reliable wireless communication, the ESP8266 WiFi module used TCP to send data and communicate to a host computer. The data-acquisition algorithm starts with establishing a synchronous connection (Algorithm 1) for each sensor. Once the host computer's IP receives a client connection from the IMUs, the IMU receives an acknowledgment (ACK), and we guarantee a successful transmission of IMU data. This WiFi module, combined with the IMU sensor, opened up the possibility to use this sensor system for more mobile or remote applications to move beyond the immobile camera-based environments of motion capture systems. Each sensor waited in a standby mode and simultaneously began recording when the host computer initiated a signal. The host records data by running a bash script to open TCP ports using the `netcat` function. It writes the data incoming from each IMU sensor to its respective output text files.

Each IMU contained a stack-based ring buffer that continuously recorded data sampled at 100 Hz from the IMU sensor to transmit it over WiFi to a host computer. The IMU sensor produced x, y, and z Euler angles packaged into a packet and stored in the ring buffer. The data-acquisition protocol in Algorithm 1 imports the data using a MATLAB script which parsed it into individual sensors and x, y, z planes. To align the measured angles from the IMU sensors, we use $\theta_{P\rightarrow C}$ for the parent-child relationship (Equation 3.8). The knee sensor is dependent on the hip angles rather than the normal plane. Likewise, the ankle angle shifts off of

the knee angle data. Manual thresholds were set for upper limits $\theta_{UL}$, and lower limits $\theta_{LL}$ based on the simulation's model-defined ranges.

**Table 3.2:** Data Acquisition Hardware Specifications

**Cost per Custom BNO055 IMU Sensor with WiFi:** $45

| | Gyroscope | Accelerometer | Magnetometer |
|---|---|---|---|
| **Axis** | 3-Axis | 3-Axis | 3-Axis |
| **Sampling Rate** | 100 Hz | 100 Hz | 100 Hz |
| **Resolution** | 16 bits | 14 bits | 13/13/15 bits (x/y/z) |
| **Max Range** | 2000°/s | $\pm 16$ G | X |

**Cost per OptiTrack Prime 13W Camera:** $2500

| | |
|---|---|
| **Sampling Rate** | 120 Hz |
| **Resolution** | $\pm$0.3 mm |
| **Latency** | 3.0 ms |

### 3.4.3 System Design

Algorithm 2 discussed the two different paths that both acquisition methods follow. The optical MoCap system presents a more conventional pipeline that begins with calibrating all 10 cameras. Optical MoCap systems like OptiTrack rely on Cartesian mapping to track displacements of markers, while IMUs use rotation and orientation of segments. As mentioned in the previous section, users can use a static trial of the subject (e.g., OMC or IMC) to scale the OpenSim model, allowing the analysis to be subject-specific. The IK tool traditionally interprets the displacements of markers to calculate angles, while IMUs innately measure joint-angles, making it easy to transition from recording data from experiments into the ID solver.

This traditional methodology also requires additional protocol before pre-processing, such as manually tagging individual MoCap markers after the motion trials have finished and transferring the data from the onboard OptiTrack system

**Algorithm 2:** Set of operations for OpenSim analysis pipeline.

```
Initialization: load model;
Data Acquisition:
if MoCap then
    calibrate system & set ground plane;
    record static trial;
    record motion trial;
    manually tag MoCap markers;
    convert MoCap markers → OpenSim markers;
    load OpenSim markers into models;
else if IMU then
    place IMUs on body;
    record motion trial;
    apply Equation 3.8 → OpenSim motion file;
end
Simulation Environment:
if MoCap then
    load static OpenSim markers → Scale Tool → scaled OpenSim model;
    load motion OpenSim markers → IK Tool → motion file;
else if IMU then
    import subject parameters with Scale Tool → scaled OpenSim model;
end
load motion trial → ID tool;
```

to a local computer. The positional marker data of the motion trial is then imported into OpenSim and applied to the scaled model of the subject to continue the analysis with the IK and ID tools.

This approach with IMUs has a more straightforward setup protocol that relies on Transmission Control Protocol (TCP) connections (Algorithm 1) where each IMUs is required to be turned on and connected to the host computer. Once the trial is complete, the data is imported into MATLAB to continue the preprocessing steps (Equation 3.8) to generate a motion file (.mot) for OpenSim. Models in OpenSim can be programmatically scaled using the *Scaling Tool*, bypassing the need for a static trial. The motion file of joint angles containing the parent-to-child relationship is the input for the IK tool, where the rest of the

analysis continues.

**Table 3.3:** Parameters for the Lower Body Models

| Segment symbols: | | Joint symbols: | |
|---|---|---|---|
| Name | Subscript | Name | Subscript |
| Left Thigh | lt | Left Hip | lh |
| Right Thigh | rt | Right Hip | rh |
| Left Shin | ls | Left Knee | lk |
| Right Shin | rs | Right Knee | rk |
| Left Foot | lf | Left Ankle | la |
| Right Foot | rf | Right Ankle | ra |

Table 3.3 outlines the variables for the hip, knee, and ankle joints for both the left and right side of the body. IMUs were placed on each model (Figure 3.11.a) to observe and record kinematics present on each joint (Figure 3.11.b). The data each IMU collected follows a similar parent-child relationship (Equation 3.8) that OpenSim implements with IK. Each recorded data set is initially independent of the other IMUs placed proximal or distal to the adjacent segments referred to as bodies. The parent-to-child relationship ($\theta_{P\rightarrow C}$) refers to the internal relationship of bodies in OpenSim models that is preprocessed into a motion file (Algorithm 2):

$$\begin{bmatrix} \vec{\theta_{lh}} \\ \vec{\theta_{lk}} \\ \vec{\theta_{la}} \\ \vec{\theta_{rh}} \\ \vec{\theta_{rk}} \\ \vec{\theta_{ra}} \end{bmatrix} = \begin{bmatrix} \theta_{lh_x} & \theta_{lh_y} & \theta_{lh_z} \\ \theta_{lk_x} - \theta_{lh_x} & \theta_{lk_y} - \theta_{lh_y} & \theta_{k_z} - \theta_{h_z} \\ \theta_{la_x} - \theta_{lk_x} & \theta_{la_y} - \theta_{lk_y} & \theta_{la_z} - \theta_{lk_z} \\ \theta_{rh_x} & \theta_{rh_y} & \theta_{rh_z} \\ \theta_{rk_x} - \theta_{rh_x} & \theta_{rk_y} - \theta_{rh_y} & \theta_{k_z} - \theta_{h_z} \\ \theta_{ra_x} - \theta_{rk_x} & \theta_{ra_y} - \theta_{rk_y} & \theta_{ra_z} - \theta_{rk_z} \end{bmatrix} \tag{3.8}$$

Each lower extremity-inspired model views the movement of the ankle to be dependent on the values of the knee, which are consequentially reliant on the hip, creating a parent-child relationship (Equation 3.8). The knee is dependent

on its parent body, the hip, meaning that the parent's position determines the angle at the knee joint. Following that scheme, the ankle depends on the knee joint position. The tensegrity models follow the same principle. The hanging model (Figure 3.8.i) has two IMUs on the two distal bodies. The support of this model comes from a long rod that holds the leg up. In the standing model (Figure 3.8.ii), three IMUs can observe a descending movement, relying on the base of the model for stability. Before applying it to the models, this parent-to-child relationship comes in the preprocessing phase. Each model's motion, human or robot, is repeated through multiple trials and then averaged to represent a general movement.

The experimental setup recorded motion capture data using custom wearable IMU sensors and the OptiTrack motion capture system. OptiTrack uses the Motive [124] software package for 10 cameras placed in a 12m x 14m x 2m configuration set at a 120 Hz capture rate to model a kinematic reconstruction of experiments with a Cartesian coordinate system. Then both sets of data are analyzed with the proposed pipeline using OpenSim to see how effectively the IMU data acquisition method to that of a MoCap system.

### 3.4.4 IMC System Limitations

The minimum tracking frequency for detecting human gait is $0.6-2.5$Hz during walking [142] and $\sim$ 50Hz during running or sprinting [143, 144]. The proposed system samples the motion of six wearable nodes at 100Hz, which should be sufficient for resolving the inverse dynamics problem and predicting the gait. As it was explained in §Section 2.5, commercial infrared motion capture systems (e.g., OptiTrack) consist of a large number of passive nodes attached to the user. Their spatial location (and therefore motion) is monitored by several cameras that also

include the infrared excitation as a ring of LEDs surrounding the cameras. Because the entire system of cameras is hard-wired to a central control unit, the system latency and spatial synchronization is only limited by the length and quality of the wired connections. This system was used as a reference system here.

The proposed system consists of a distributed network of inexpensive nodes connected through a Wi-Fi network. There are several possible drawbacks that can make such a system significantly under perform a commercial motion camera system.

- **Problem:** the synchronization between individual nodes transferred using the Wi-Fi network. **Solution:** each node records locally the entire event and timestamps the data. The entire set of data is transferred only at the end of the experiment.

- **Possible problem:** The synchronization of the internal clocks of the individual nodes. **Solution:** The initial handshake synchronization uses the ESP8266 WiFi Module, which has a sending and receiving rate of 4ms, which corresponds to a frequency of 250Hz, which is significantly higher that the one required for monitoring the walking gait ($0.6 - 2.5$Hz).

- **Problem:** BNO055 Clock Stretching Error. **Solution:** The I2C timing included in the BNO055 datasheet [141, 145] states that you can set the intervals between I2C commands under normal power to be around 2 - 3 $\mu$s. For single sensor communication, we suggest using a time delays of 10ms to avoid any 100 - 200 $\mu$s gaps from the data being sent to the register.

## 3.5 Conclusion

The methodology created in this dissertation systematically analyzes models and estimates the required dynamics to reproduce the experimental motions. Each experiment compares the effectiveness of monitoring human biomechanics and robotics through simulation with two different methods of data acquisition: cameras tracking reflective markers and wearable IMUs. The setup simultaneously monitors kinematic behavior using the OptiTrack motion capture system against wireless 9-axis IMU sensors.

Although motion capture systems are the standard solution for tracking the kinematic behavior of systems in the real world, IMUs are a far more mobile and cost-effective alternative that has demonstrated promising results for analyzing multi-body dynamics. Wearable sensors rely on physical manipulation and orientation displacement in space to translate into joint-angle relationships for OpenSim motion files. In addition, IMU sensors demonstrate modularity for incorporating sensor feedback on kinematic behavior with flexible robotic systems. This low-cost mobile kinematic monitoring system demonstrates the capability for future analysis of non-room bounded activities and the ability to simulate both human and robotic applications within the same environment.

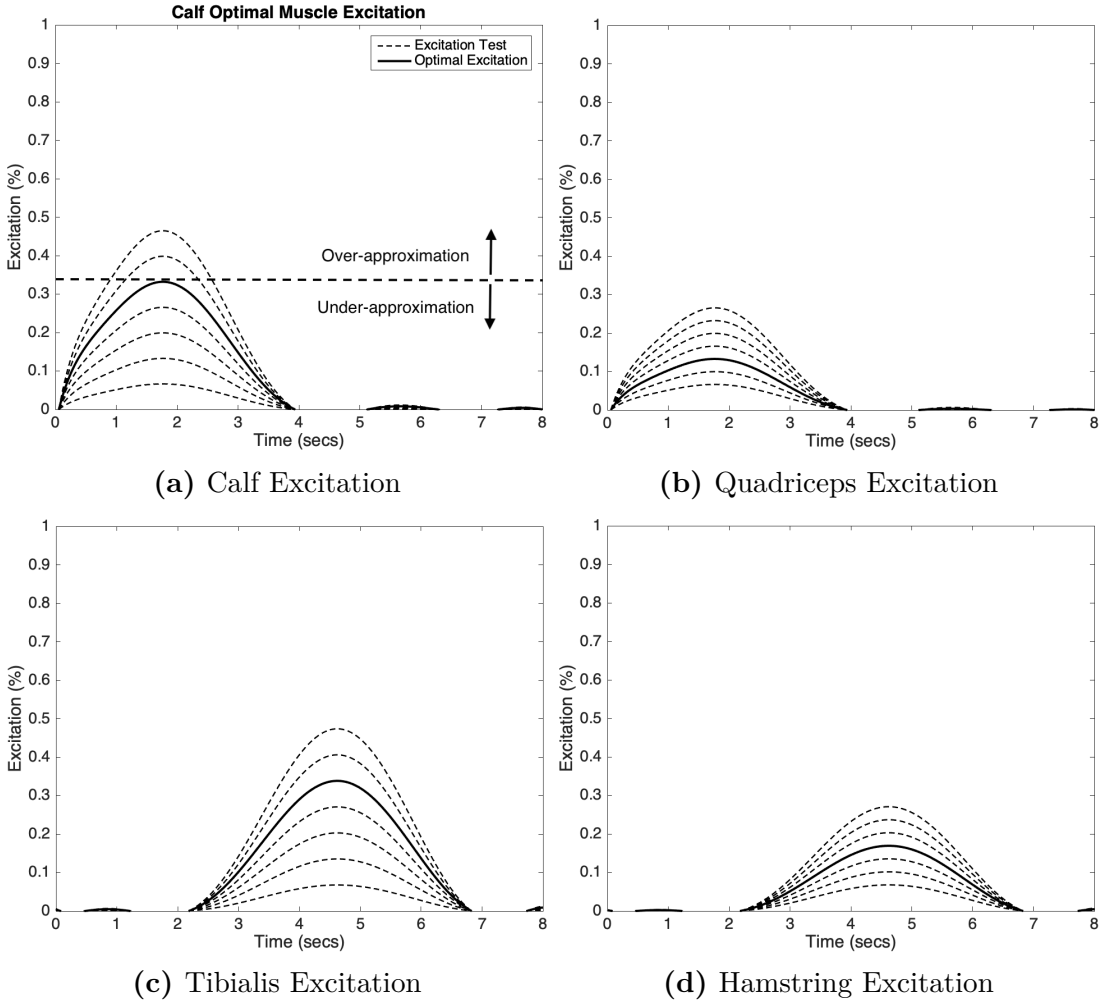


**(a)** Calf Excitation

**(b)** Quadriceps Excitation

**(c)** Tibialis Excitation

**(d)** Hamstring Excitation

**Figure 3.7:** Muscle activation patterns for a squat-like descent were increased incrementally 10% of the maximum to isolate the optimal excitation pattern. The undershoot (under the optimal line) is an under-approximation limiting the range of depth, while the overshoot (above the optimal line) to over-exertion causing the structure to fall over.

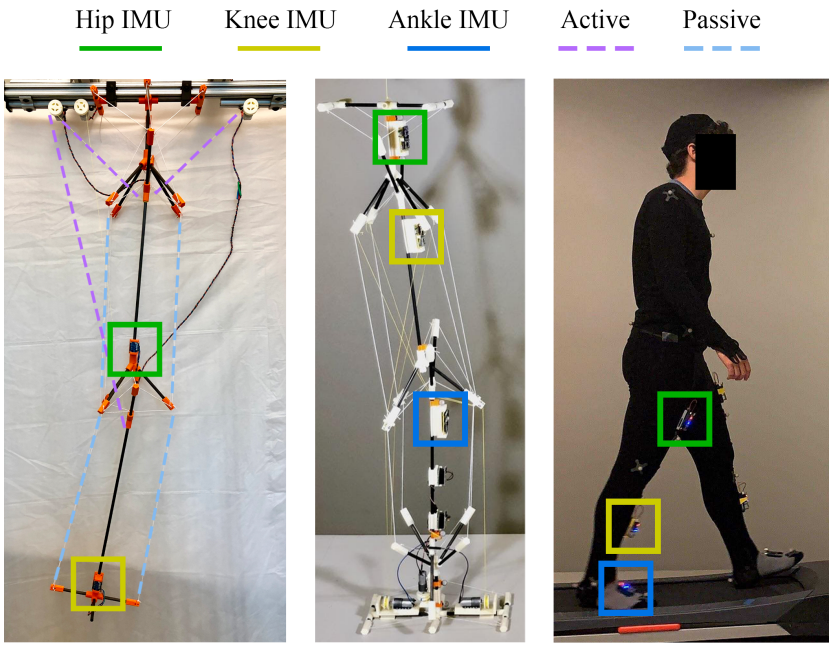


**Figure 3.8:** The suspended-gait flexible-rigid structure (i), flexible-rigid standing structure (ii) and the full body motion capture setup (iii).

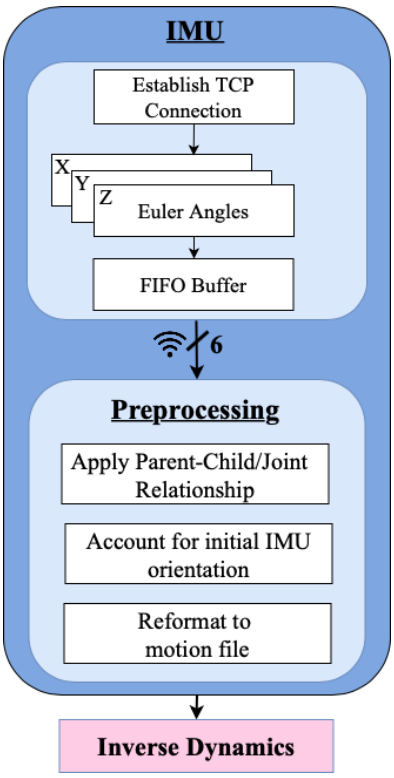


**Figure 3.9:** This IMU data analysis pipeline represents the process of data acquisition from the sensors into the an executable motion file for OpenSim analysis.

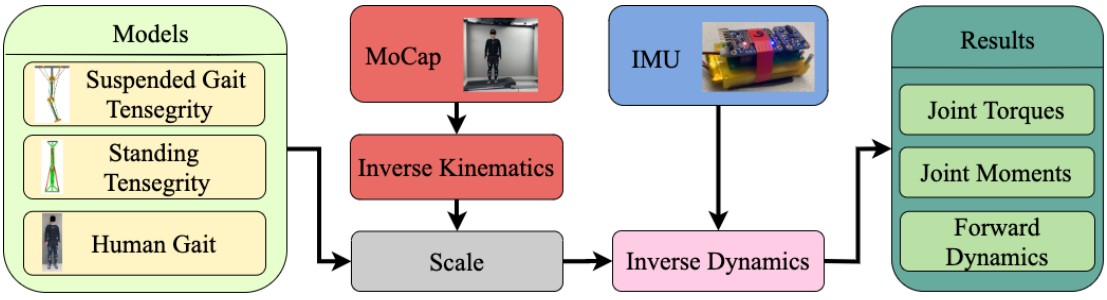


**Figure 3.10:** This pipeline represents how individual models are used in tandem with MoCap and IMU acquisition methods to analyze kinematic and dynamics behavior.

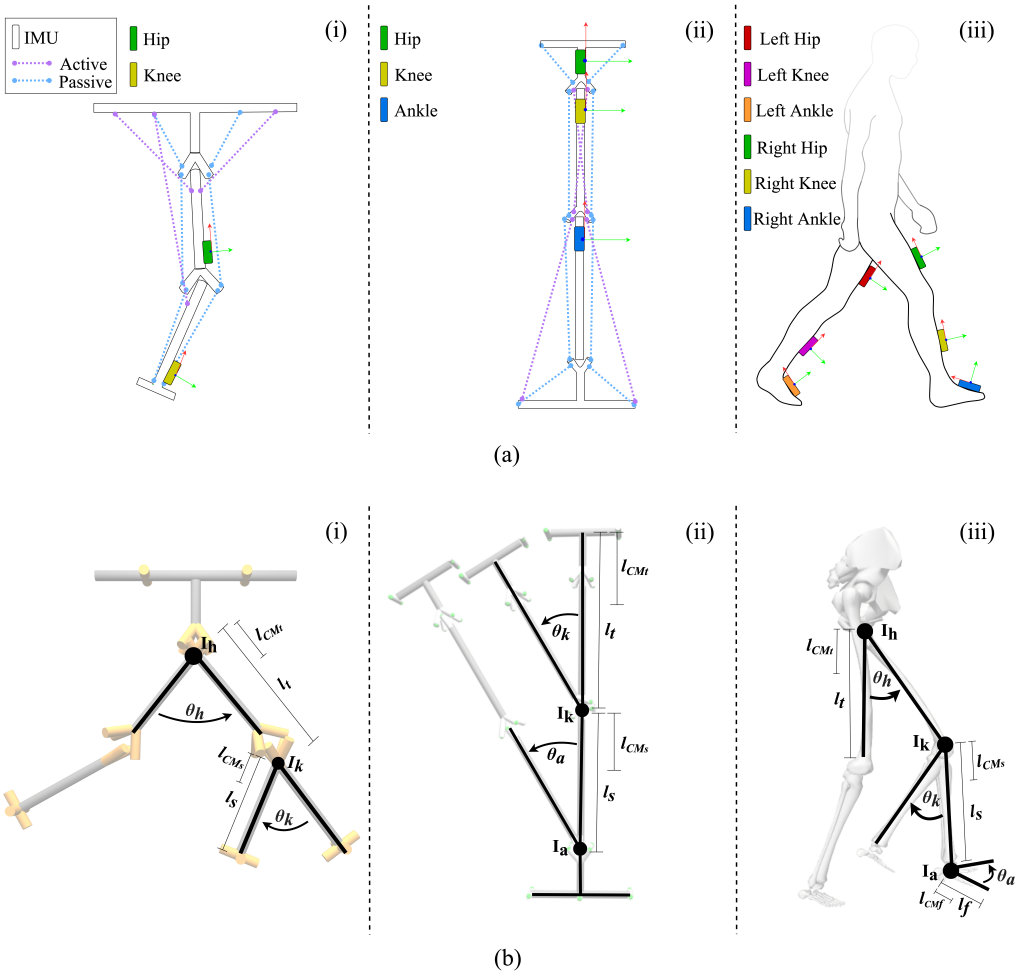


**Figure 3.11:** (a) IMU Location Diagram. (i) The suspended gait-inspired tensegrity model has sensors for hip and knee orientated on the saggital plane. (ii) The self-stabilizing tensegrity includes an additional sensor for ankle displacement. (iii) Represents the placement for each IMU on the lower extremities of the human body. (b) Visual diagram of the mathematical model (Equation 4.5) representing the moment of inertia required to overcome by implementing the contraction of active tensile elements for the same (i), (ii), and (iii).

# Chapter 4

# Prototyping and Sensing

## 4.1 Introduction

The process for designing, prototyping, and testing an inspiration from Nature to flexible-rigid structures has been widely adopted in the field of robotics. These biomimetic mechanisms have characteristics for adaptability, flexibility, and robustness; however, they come with their own set of challenges and limitations (i.e., design parameters can be inversely related). For example, the design needs to be mechanically robust and flexible, while components need minimal mass and non-restrictive fluid movement. The methodology from design to prototype breaks down into three parts:

- translation from conceptual design into components and materials
- iterative prototyping of the flexible-rigid designs
- sensor network to measure kinematics and translates it into the right movement at the right time

Simulations are crucial for modeling the interaction between the flexible robotic

structure and biomechanical designs before experimentation. Therefore, it is implemented simulations before each design. Because OpenSim is designed with a parent-child relationship when building models, the mechanics are analyzed similarly to how our self-localization was developed. The importance of modeling in simulation and CAD establishes the size, shape, and dynamics for assembly.

## 4.2 Structural Design

### 4.2.1 Human Lower Extremity Inspired Joints

Musculoskeletal connections within the human body rely on the cohesive efforts between bones to support excess amounts of forces and muscles and ligaments to manipulate joints while maintaining poise. Anatomical systems in human bodies are structurally and functionally complex: bones, muscles, and connective tissues. These intricate systems are stable, durable, and adaptable to external loads. When acted upon by an outside force, these structures can react and distribute the strain across other tensile forces and return to a relaxed and fortified state. The lower half of the human body consists of many joints. This work focuses on mirroring the hip, knee, and ankle joint along the sagittal axis in these designs.

In humans, the hip is capable of a variety of manipulated motions, including adduction, abduction, and extension. The knee joint flexes along one axis of rotation similar to revolute joints in rigid robotic systems. Plantar and dorsiflexion produced by the ankle joints also maintain innate flexibility to adhere to uneven terrain when performing gait [137] or maintaining an upright position. Manipulation of the joint in the flexible-rigid structure were generated by the cable-driven actuation, and forces are dispersed throughout the structure using tensile elements

[59, 127].

One of the first representations of a functional human body tensegrity-inspired manipulator was proposed by Graham Scarr [146]. This concept uses two rigid and several tensile elements interconnected into a flexible-rigid structure to replicate aspects of the functionality of a human elbow joint. Baltaxe et al. [18], Lessard et al. [59], Jung et al. [20] and Castro et al. [136] proposed several concept manipulators that replicate the behavior of elbow, shoulder and knee joints. Figure 3.4 schematically shows the physical model comprised of a "hip" joint (Figure 4.4) and a "knee" joint (Figure 4.5). The interconnected web of passive and active tensile components mimic the biological tendon and ligament connections ensuring system compliance, while preventing direct contact between the rigid components.

### 4.2.2 Rigid Bodies

The chosen length of the compression elements to match the dimensions of the bones in the OpenSim 3.0 model *Gait2345_Simbody* described in Chapter 3. In older models (Figure 4.1), the physical prototypes used compression elements created from wooden dowel sticks. The recent prototypes use carbon fiber rods assembled with 3D-printed acrylonitrile butadiene styrene (ABS) pieces to make the rigid bodies. The carbon fiber rods act as an equivalent bone structure of the human body. Joints shown in Figure 4.4 and 4.5 display both the CAD assembly and prototype versions of the structure that rely on the designs of each three-dimensional printed component. The angles at which the carbon fiber rods extrude allow the structure to route cables and maintain a frictionless network that manipulates in motions similar to the mechanics of a human body.

In Figure 3.4, the upper compression element is equivalent to a human pelvic bone, the middle piece mimics a femur bone, and the lowest segment acts as the

tibia and fibula, simplified into one rigid body. The hip joint performs similar to a ball and socket joint, is not confined to one axis of rotation like most conventional robotic joint designs (Figure 4.4a,b). The knee joint has a dominant degree of freedom during flexing using a single actuating muscle, which resembles the biological biceps femoris (Figure 4.5a,b). The latest designs consist of four main rigid elements representing the human pelvic bone (for one leg), femur, tibia, and foot. The lower extremity tensegrity structure in Figure 3.6 has rigid bodies similar to the location of the pelvis (hip joint), femur (above the knee joint), tibia (below the knee joint), and foot (below the ankle joint).

### 4.2.3 Tensile Elements

The essential component that maintains stability and achieves characteristics similar to muscles, tendons, and ligaments in the leg within flexible-rigid structures are the tensile elements [14]. Using cables for our tensile elements in the manipulator (bungee cord and fish-line spectra cord in our physical model), they belong to two categories: passive and active [20]. The passive cables represent the biologically inspired fascial connections of the hip and knee joints: the ligaments and tendons. The arrangement of passive elements absorb impacts and maintain structural compliance in response to external forces. Active tensile elements allow the structure to create motion similar to the human leg and couple into antagonistic pairs. Within each contraction of an active cable has an antagonistic duo, which lengthens and relaxes, demonstrating how muscles contract and extend.

Secured by a complex network of tensile components, the flexural joints perform similarly to muscles, and other tendon-based bone-element connections [20]. For example, our hip joint is secured by a complex tensile component network that performs similarly to muscles and other fascial connections to the bone-mimicking

elements. To achieve multi-axis compliance, the *Y-shape* design for the femur and tibia compression elements (Figure 4.4) is capable of generating flexion, extension, adduction, and abduction motion. The positional displacement of the suspended hip joint produces a lifting motion advancing the structure to begin gait (see Figure 4.4). When the cable-driven actuators pull the tibia segment, it shortens the hamstring element causing knee flexion to trigger. Pretension passive cables aid the tensegrity in the original formation and adjust in response.

For instance, the gait-inspired hanging structure can maneuver and provide one fluid gait motion as the femur and tibia are manipulated. The tibia compression element is attached to a three-rod base, designed similarly to the patella and femur. It creates a knee joint that flexes along one axis of rotation (as shown in Figure 4.5). When the cable-driven actuator shortens the hamstring, it pulls the tibia segment to flex the knee joint. This also pulls the femur, allowing the structure to maneuver and provide one fluid gait motion.

### 4.2.4 Directed Cable Routing & Actuator Selection

The flexible-rigid joints in this work are inspired by the anatomical characteristics of the muscular, tendon, and ligament connections within the human leg joints. Cable-driven actuators shorten the cables to resemble muscle contractions and perform knee flexion, hip swings, or ankle plantar and dorsiflexion. Each cable is actuated by a dedicated motor, which can either turn in one direction to tighten the line or in the opposite direction to loosen it to generate a motion. With our suspended gait-inspired design, the cable-driven actuator acts similarly with the iliopsoas (front hip motor) and pulls the femur-inspired element forward. The antagonistic active tensile element to the iliopsoas, the gluteus maximus (back hip motor), moves the structure back to produce a follow-through motion. The

bicep femoris long-head (hamstring motor) is essential in emulating human knee flexion.

The design is orientated towards cable-driven actuation, which has motors located off-centered from the robot to reduce the structure's weight and centralize the moment to overcome lower. The location of the actuators is critical for applying the optimal forces and actuation patterns (Figure 4.6) on the deforming structure while minimizing the power consumption and found when simulating the model. Varying the size of the models (50% Scaled, Unscaled, and 150% Scaled in Figure 4.7) within the simulation guided the hardware requirements. Figure 4.7A shows the predicted forces necessary to actuate the structure during a complete gait cycle. To maximize the torque to weight ratio, we select three Polou 3454 DC motors with a 100:1 gear ratio and 0.64 Nm stall torque (the most significant predicted force is 100N, which translates to a 0.44 Nm applied torque). The power consumption of the OpenSim 3.0 simulated robot was computed using the *ProbeReport* and the *JointInternalPowerProbe* analysis [126].

## 4.3 Prototyping

### 4.3.1 Introduction

Most robotic structures that replicate the gait of human legs consist of rigid elements, equivalent to natural bones, connected by revolute joints. The revolute joints act similarly to anatomically correct knee joint; however, they have one main caveat: revolute joints have only one axis of rotation [3]. Anatomically inspired joints consist of rigid and flexible elements suspended in a network of muscles, tendons, and ligaments that work in unison to allow the joint to flex, move and contort in many degrees of freedom [59, 147]. Hence the decision to make a

flexible-rigid design consisting of rods and cables. This approach has advantages including, but not limited to: numerous degrees of freedom, switchable actuation locations, and mechanical flexibility.

This section proposes an alternative approach: A design pipeline that develops flexible–rigid structures that recreate the kinematics of human legs. The solvers help in the production and planning process, acting as an important role in assuring that a successful system is designed. This iterative loop of modifying designs and testing them through a virtual environment will ease the manufacturing process and the time spent on manipulation strategies. It also discusses the design decisions of the types and placements of the sensors that can detect movement and users (as input) and actuate the manipulator (as output) at the right time and with the right amount. The design arrangement given from the virtual environment will be drafted in a Computer-Aided Design and drafting (CAD) environment (AutoDesk's Fusion 360) that is then to be manufactured in first 3D printing materials to analyze kinematic behavior.

### 4.3.2 Knee-inspired Design

The first flexible-rigid manipulator developed began by creating a biologically inspired human knee joint. The first models created through both simulation and physical prototyping focused on imitating the motion of knee flexion. After testing different designs in the NTRT environment, we found that the last model (Figure 3.3(iv)) has suspension that achieves flexion with the bicep femoral muscle group. This aligns with the anatomically correct muscles required for flexion.

For prototyping, we constructed our model using dowel sticks and 3D-printed joints (Figure 4.2) to create the overall geometry. In the first iteration of the physical model the attachment points at the knee joint became too congested,

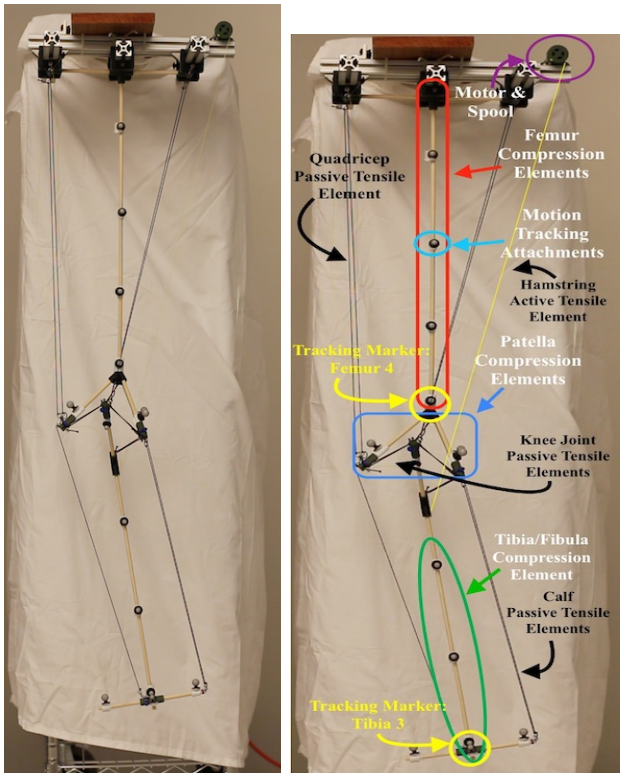


**Figure 4.1:** Proposed flexible-rigid knee joint, connecting femur and tibia equivalents. The joint is controlled by an active pair of strings tuned for stiffness creating a variable level of flexibility within the structure [19].

which could cause cable interactions. To resolve this issue, new end parts (Figure 4.2) were printed for the knee model that contained holes to tread the elastic cord through and still keep it in the correct line of action. For the actuation a simple torque analysis was done on the knee model with a total weight, estimated at $0.74N$, with length of the model at 116 cm. To find max torque needed to lift the entire model the total weight and length were used in the following equations:

$$\tau = F \cdot L \tag{4.1}$$

Equation 4 shows $\tau$ is Torque, F is the force in Newtons and L is the length in centimeters. To calculate torque required by motors:

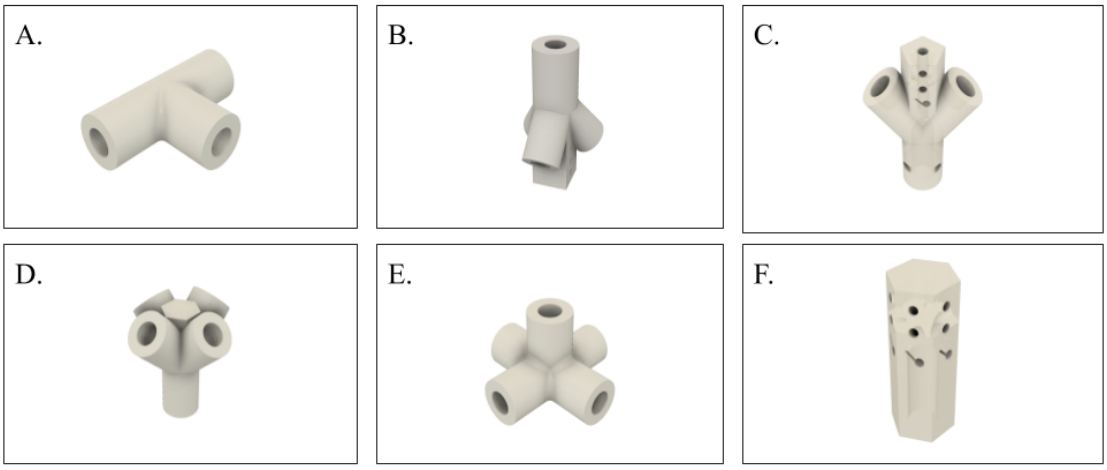


**Figure 4.2:** Close up of the 3D printed end pieces with holes to keep the elastic cord in the proper line of action. (A) T-joint (B) Tri-joint (C) Y-joint (D) Quad-joint (E) Quad Base (F) Endcap

1. The minimum torque is when the length of the cable is $0.58m$ and the total mass is at the end of the length

2. The max torque at max length of $1.16m$ and the total mass is at the end of the length

The peak torque required is a maximum of $0.85N \cdot m$ to actuate the knee joint [136].

### 4.3.3 Gait-inspired Joints Design

This suspended flexible-rigid gait model, (Figure 4.3), emulates the motions of the human hip and knee flexion. The design consists of three main rigid elements representing the human pelvic bone, the femur and the tibia (Figure 3.4). The compression elements are carbon fiber tubes (equivalent to the bone structure in a human body), and the tensile elements are cables (muscles, tendons and fascia), which keep the structure in equilibrium through varying levels of tension.

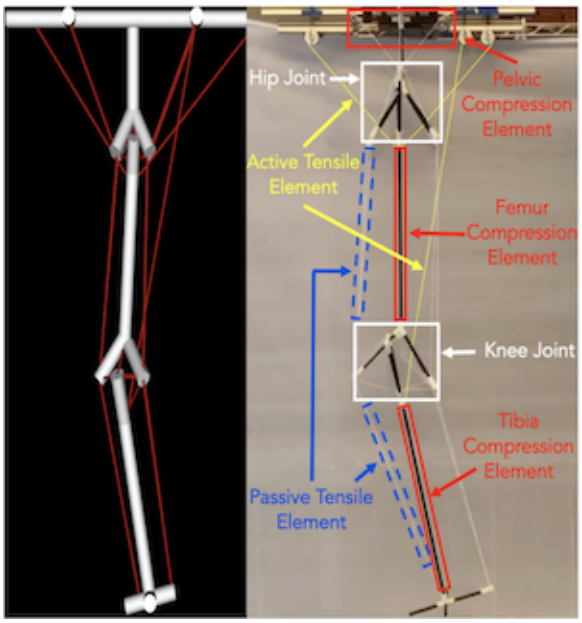


**Figure 4.3:** Tensegrity flexural knee and hip joint [20] connecting the pelvic, femur and tibia rigid bodies.

The joints are constructed similar to before by interlocking Y-shaped and Quad-pronged compression elements (Figure 4.4 and 4.5) suspended by a network of passive and active tensile components, which gives the tensegrity manipulator the ability to produce the specified four stages of gait: *Heel Lift, Extension Forward, Step Through, and Equilibrium.* These three primary muscles are vital and must work in unison in order to flex different segments of the leg. Through the design with three-dimensional-printed components, we were able to easily build the rigid compression elements in the exact same representation from the simulation. Referring to Figure 4.4b and 4.5b (the 3D printed pieces in orange), each printed component works as a puzzle where prototyping simply pieces together to create this multi-body system. The actuators are then constructed in the places of designated active tensile elements, annotated in Figure 3.4, while the rest of the passive tensile elements create a complex network of cables holding the system in one piece.

The most prominent active muscles throughout one cycle of in-place gait are are the hamstring, iliopsoas and gluteus maximus [148]
[149]. Normal gait requires a complex configuration and due to this being a proof of concept flexible-rigid design, we focused our attention on aligning the biomechanics and robotic manipulators within the same system to prove that it is capable of precisely simulating custom models.

The behavior of this manipulator was comparable to a suspended human leg performing in-place gait and was never intended to carry a load. Our model has an equivalent cable-driven actuator for each muscle one of them. Figures 4.4 and 4.5 show the "hip" and "knee" joints. The 3D printed connections in orange (Figures 4.4a and 4.5a), work similarly to a puzzle, where prototype extrusions are assembled to create a multi-body system. The actuators positioned at one end of the active tensile elements annotated in Figure 3.4, while the rest of the passive tensile components create a complex network of cables holding the system together. For easier manipulation and to match the geometry of the simulated structure, the Y-shaped pieces have through holes for the actuating cables. The active–passive pairs of tensile elements support the structure and prevent direct contact between the compression elements.

The Y-shaped designed pieces contain holes located to feed cables through the compression elements of the joints for easier manipulation and matching placement to the simulator. One method to reduce friction is by guiding the cables directly to the rigid compression elements rather than feeding it within the structure. The endcap piece design simple contains three places of attachments for the cables to connect to. Our quad piece composition allows for the pelvic compression element and four separate extremities to attach to the femur-inspired component through a network of passive cables (Figure 4.4). The angles at which the active tensile

elements are pulling the structure avoids surface friction by keeping the structure suspended with the passive cables.

As mentioned earlier, bungee cords were used for the passive tensile elements and fish-line spectra cord for the active ones. Passive tensile elements distribute forces upon impact and maintain structural compliance in response to external events. The flexible-rigid manipulator contains sixteen pairs of antagonistic passive elements (six in the hip, and ten in the knee), which deform due to the applied force, then return the leg to its equilibrium position. Pre-tensioned passive cables allow the tensegrity structure to return to its original shape.

Active tensile elements allow the structure to create motion similar to the human leg and generate human-like gaits. Each active cable has an antagonistic cable, which lengthens and relaxes, similar to how muscles contract and extend. The positional displacement characteristics from the hip joint produces a lifting motion advancing the structure to begin gait referring back to Figure 4.4a and Figure 4.4b. The tibia-inspired body is attached to a three-rod base of the femur composing a knee flexural joint focused on performing knee flexion shown in Figure 4.5a and Figure 4.5b.

The joints focused throughout this paper imitate the biologically inspired human hip and knee joint. Tensile elements are the cables that act as the require muscles, tendons and fascia that keeps the structure in equilibrium through levels of tension variation. Figure 4.3 shows the upper compression element is the equivalent pelvic bone, the middle being the femur bone, and the lowest segment acting as the tibia and fibula simplifying into one single component. The pelvic and hip joint are characterized to perform as a ball and socket joint that is not confined to one axis of rotation like most conventional robotic joint designs (figure 4.4a and 4.4b).

The final step was to see how the estimates on the actuator output requirements from our custom leg models compared to a biologically accurate model. This used one of the many provided models from the Simbios library (e.g., Gait2345Simbody) and placed it under the same custom angles of flexion/extension for the knee and hip joints required for the desired hinged gait pattern as was placed upon the second of the custom models. Although this prototype robotic manipulator was not intended to stand on its own, similar to the human hip, the two cables on the femur emulate an action similar to walking. The values received could then be compared to our custom leg models to see the biological accuracies for the range of motion from our custom models are discussed in Chapter 5.

Activation values $a(t)$ change the output of the forces generated from the muscles. At 100% of the activation values, it yields the maximum isometric force output to manipulate the model. The Inverse Kinematics (IK) and Inverse Dynamics (ID) tools shown in Figure 3.2 were used to predict the force applied on the active tensile elements, joint angles and torque values to manipulate the rigid elements:

$$\mu_n = r^n \cdot Q \tag{4.2}$$

$$Q = \frac{\mu_n}{r^n} \tag{4.3}$$

where $n$ represents the number of joints, $\mu$ is the moment, $r$ is the radial distance from the fixed point to the end of the rod, and $Q$ is the muscle force. After matching the properties (e.g., tensile connections, compression lengths, etc.) of each model with the Scaling tool, we programmatically adjusted and simulated the placement of active elements to isolate optimal placement of our actuators. This simulated process gauges the necessary muscle force to position the lower portion of the leg in the desired phases of gait and maintained consistency between the physical and OpenSim 3.0 models.

The cable-driven actuator corresponding to the iliopsoas (front hip motor), is designed to pull the femur-inspired element forward. The antagonistic active tensile element to the iliopsoas, the semimembranosus (back hip motor), pulls the structure backwards to produce a follow through motion. The bicep femoris long-head (hamstring motor) is essential in emulating human knee flexion. Although this initial prototype robotic manipulator cannot stand on its own, it should be noted that much like the human hip, the two cables on the femur could emulate an action similar to walking. The single cable actuation is controlled by a motor, which has a single line spool, that reels in, to tighten the cable, and unwinds to lengthen the cable as needed in order to create gait. Equation (4.2) was used to obtain the cable-driven actuation patterns (Figure 4.6), and Equation (4.3) to find the forces exerted by the muscle as a ratio of the moment and radial distance. It was known that the force exertion requirements on the actuators would be heavily increased again due to the moving upper leg and we used (Equation 4.2) to get our force estimates. The hip joint propels the leg forward, while the hamstring releases the knee in order to create the extension forward and step through stages for a more human-like gait motion as seen in Figure 4.9: Extension Forward. We based our goal trajectory positions off of the original five stages of gait motion [150, 151], but decided to reduce the number of stages to four to simplify the explanation of motion.

To further validate our simulation (Figure 3.5), we compared its power consumption with the physical prototype's (Figure 4.7c). The power consumption of the electrical motor is significantly larger than the other components. The microcontroller (290 mW) and sensors (25 mW) have a constant power requirement that was subtracted from the global power consumption to compute the power consumption of the motors. The model underestimates the idle power consump-

tion, but it predicts well the power consumption during the third and forth stages of gait. The initial mismatch is most likely due to the differences between the ideal behavior of the OpenSim 3.0 muscles and commercial electrical motors at low speeds.

### 4.3.4 Self-stabilizing Designs

The current tensegrity-inspired design maintains structural integrity in the upright position due to the distribution of strain amongst the ankle, knee and hip joints within. The combination of passive and active elements manipulating the structure in a downward or upward motion follows a similar kinematic pattern of muscle activity to experiments done by Dionisio et. al [137]. Activation patterns follow peak electromyographic (EMG) readings from user testing during the downward phase: calf and quadriceps, and standing phase: tibialis and hamstring. The location of the muscles (Figure 3.6) on the front of the femur-based rigid body represent the quadriceps, or vastus medialis, and the back of the femur represents the biceps femoris, or hamstring. The tibia-based compression element mounts the tibialis in the front, and the calf on the back. The system off-centers the actuators towards the bottom to distribute weight near the ground limiting the rotational moment of intertia to overcome.

The simulated model approximates physical characteristics to approach angular displacements. Each programmable chip (ESP-12S module) is set up with WiFi compatibility and a motor driver that controls both the ankle and knee active elements shown at the base of Figure 3.6. The ankle joint acts as a network host that receives commands from the controller, and reacts based from the assigned, $\theta_{target}$, given by the user. The ankle joint focuses on lateral movements, while the knee manipulates the muscle-inspired cables to create a squat-inspired

downward and upward phase. Figure 3.11(b(iii)) focuses on angular displacements for the primary joints to descend: ankle $\theta_1$, and knee $\theta_2$.

$$y = \begin{bmatrix} \theta_1 \\ \theta_2 \end{bmatrix} = \begin{bmatrix} \theta_{ankle} \\ \theta_{knee} \end{bmatrix} = \begin{bmatrix} \theta_{ankle_x} & \theta_{ankle_y} & \theta_{ankle_z} \\ \theta_{knee_x} & \theta_{knee_y} & \theta_{knee_z} \end{bmatrix} \tag{4.4}$$

$$c = m_2 l_1 l_{CM_2}$$

$$I[\theta] = \begin{bmatrix} m_1 l_{CM_1}^2 + m_2 l_1^2 + I_1 & c \cdot sin(\theta_1 - \theta_2) \\ c \cdot sin(\theta_1 - \theta_2) & m_2 l_{CM_2}^2 + I_2 \end{bmatrix}$$

$$M[\theta, \dot{\theta}] = \begin{bmatrix} 0 & c \cdot cos(\theta_1 - \theta_2)\dot{\theta}_2 \\ -c \cdot cos(\theta_1 - \theta_2)\dot{\theta}_1 & 0 \end{bmatrix}$$

$$G[\theta] = \begin{bmatrix} (m_1 l_{CM_1} + m_2 l_2) \cdot g \cdot sin(\theta_1) \\ (m_2 l_{CM_2}) \cdot g \cdot sin(\theta_2) \end{bmatrix}$$

$$U(\theta) = \begin{bmatrix} \tau_1 tan(\theta_1) \\ \tau_2 tan(\theta_2) \end{bmatrix}$$

$$I(\theta)\ddot{\theta} + M(\theta, \dot{\theta})\dot{\theta} + G(\theta) = U(\theta) \tag{4.5}$$

The $I(\theta)$ represents the inertial matrix, $M(\theta, \dot{\theta})$ represents the coriolis and centrifuge matrix, $G(\theta)$ represents the gravitational matrix, and $U$ represents the acting tensile forces on the system with $\tau$ is the torque generated from the actuators. To characterize each segment (e.g., 3D fabricated pieces, PCB boards, carbon fiber rods), the required moment of inertia to overcome at each joint is approximated at the ankle and knee joints with inputs:

1. $l_1$ and $l_2$ for the length of both linkages

2. $l_{CM_1}$ & $l_{CM_2}$ for the length of the center of mass from the base of the linkage

3. $m_1$ & $m_2$ for the mass of each linkage

4. $\theta_1$ for the angular displacement of the ankle

5. $\theta_2$ for the angular displacement of the knee

**Table 4.1:** Tensegrity Structure Characteristics

| | $l[m]$ | $l_{CM}[m]$ | $m[kg]$ | $I[kg \cdot m^2]$ |
|---|---|---|---|---|
| Femur: 1 | 0.5766 | 0.2110 | 1.7744 | 0.1966 |
| Tibia: 2 | 0.4064 | 0.3700 | 1.11 | 0.0611 |

The structure's angular displacements are directly affected by the contraction of tensile forces from active muscle-inspired cables to overcome the moment of inertia, the coriolis and centrifuge forces with consideration of the effect of gravity (Equation 4.5) throughout upward or downward motion.

## 4.4 Distributed Sensing Network

### 4.4.1 Introduction

The integration of both mechanical (e.g., transducers, encoders) and electrical (e.g., IMUs, bio-metric) sensors for human-robotic systems is still a new field. The dynamic and kinematic equations produced from the solvers will be implemented to report the current state of the subject's position. Applying the predictive model to the integrated sensor network will enable us to measure the current state of the user (i.e., bio-mechanics of human body), and predicts what the structure's the next movement should be. For example if someone lifts their leg with the intent to step forward, the model assumes the extension of the foot will follow then the rest of the stages of gait will follow.

### 4.4.2 System Design & Control Strategies

#### Open-loop Control

One of the goals of the paper is to propose a pipeline, where a flexible manipulator will be modeled and fabricated to match the "desired kinematics" of a human leg. With the gait-inspired design, Figure 3.2 shows an overview of the iterative design strategy and used the FD solver to provide the excitation pattern (Figure 4.6) that manipulates the hip and knee joints (Figure 4.7) throughout four the stages of gait in the sagittal plane (Figure 4.9). Stage 1: *Heel Lift*, starts from a neutral position, and contracts the hamstring-inspired cable to initiate knee flexion backward. Stage 2: *Extension Forward*, contracts the iliopsoas-inspired muscle causing the entire tensegrity structure to move forward, while the gluteus maximus-inspired and hamstring-inspired cables release the posterior hip and hamstring. Stage 3: *Step Through*, implements the combination of "leg-lift" and "swing". When the iliopsoas flexes the lower limb at the hip, it drives the entire leg backward until it is positioned behind the body. Stage 4: *Resting Position*, restores the tensegrity structure to its neutral position. Once in the *Resting Position*, one cycle of gait has been completed, and if desired, the structure can continue the gait cycle repeatedly.

Modeling the tensegrity hip and knee joint in OpenSim 3.0 provided analysis on both passive and active connections for our physical prototype. Forces imported into the FD tool generate motions for each model. Each stage of gait excites one active element to contract at a time while the others remain passive or release tension. Each actuator in the physical prototype correlates with one of the three prominent active muscles in a human leg. The tangential force generated by the

cable-driven actuators ($F_{T_{max}}$) during each stage of gait is computed as:

$$F_{T_{max}} = \frac{\tau}{r} \tag{4.6}$$

where $r$ is the radius of the spool attachment for the motors, and $\tau$ is the stall-torque. Each cable-driven actuator contraction follows a sequential state machine.

This approach begins with the virtual control strategies by interpreting the kinematic data retrieved from the motion capture system and generate a set of dynamic equations. For example, if the simulation is meant as a function of gait, it will use bio-mechanic movement from lower extremity joints as an input and output a set of muscle activation with forces applied. This directly influenced the design of a controller that actuates the mechanism, and achieve the projected goal of preforming human gait. The purpose of the control strategies is to introduce steps to make a widely adopted basis that can easily be introduced to human-robotic systems.

### Closed-loop Control

The closed-loop control system follows the same procedure for imitating one cycle that was described in the Open-loop control section. The movement imitates the "virtual" muscle activation patterns (Figure 4.6) using three motors and two low-drift 9-axis BNO055 IMU (Inertial Measurement Unit equipped with an accelerometer, gyroscope, and magnetometer) sensors located at the base of the hip and knee (Figure 3.4).

Each sensor underwent a calibration process recommended by the manufacturer using a series of sensor-fusion algorithms that blends the accelerometer, magnetometer and gyroscope data into stable three-axis orientation output [141, 140]. For calibrating the position of the sensors, we used the dynamics captured by the

open-loop system along with the simulation to find the model's limitations and available range of motion. This process executed a series of open-loop control motions for each stage of gait and used the motion capture recordings to correlate the angles of the compression elements with the IMU sensor readings. The sequential state machine requires a compensation for the forward kinematics and position. Here we monitor the hip ($\theta_{hip}$) and knee ($\theta_{knee}$) angles using the IMU sensors and update their values in the state machine at each time iteration (see the "Control" panel of Figure 3.2). The actuation strategy relies on tracking the angles using the IMUs, applied forward kinematics using the motor driver, then updated the target angle ($\theta_{ref}$) for the next stage of gait. This feedback loop incorporates a proportional controller that effectively manages the physical model to change the stages of gait once the system reaches a minimal steady-state error of 1.25% from the target position. In the event of an overshoot, the physical model is capable of correcting itself (Figure 3.2) when a gait stage has malfunctioned or is disturbed by an unanticipated outside force (i.e., pushing or pulling the structure out of the range of values).

The simulation environment provides an approximation for the amount of tensile forces required to approach the desired angular displacements. As illustrated in Figure 4.11, the tensegrity structure implements a self-standing localization system based on position compensation from angle movements read from the sensors. Each IMU sensor is packaged with the MPU-9250 9-axis module (3-axis gyro, 3-axis accelerometer and 3-axis compass) to measure kinematic movement. The programmable ESP-12S module is equipped with a microcontroller with WiFi compatibility acting as both as client (e.g., sensors, knee microcontroller), and access point (e.g., ankle). Within this wireless network (Figure 4.10), sensors representing the hip, knee and ankle angles report angular displacement to the ankle

through User Datagram Protocol (UDP). The ankle interprets the data and commands the motor driver to manipulate the ankle-inspired tensile elements while sending a command to the knee microcontroller responsible for the contraction and releasing of the tibialis and calf-inspired elements. During the squat-like descent, the actuators contract the quadriceps and calf-inspired cables while lengthening and relaxing the tibialis and hamstring-inspired cables. The rising motion works antagonistic to the previous where the tibialis and hamstring-inspired cables shorten, and contract releasing the quadriceps and calf-inspired cables bringing the leg to the upright standing position.

## 4.5 Conclusion

The internal/embedded localization system (Fig. 4.11) created provides positional-based feedback to achieve and maintain desired angular displacement. Monitoring hip, knee and ankle joints during each movement prescribed the cable-driven actuators to re-position the structure. Using the same hardware and algorithms for the wireless sensing network, this work extends the applications to more complex systems like the lower extremities of the human body performing gait.

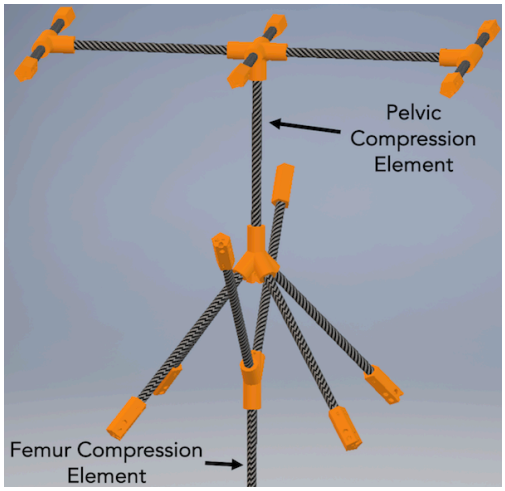


**(a)** 3D CAD showcasing the 1 Quad-joint, 1 Y-joint, 1 Quad base and 12 Endcaps

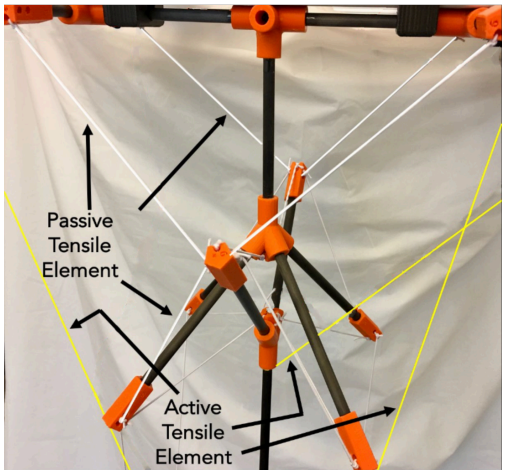


**(b)** Prototype

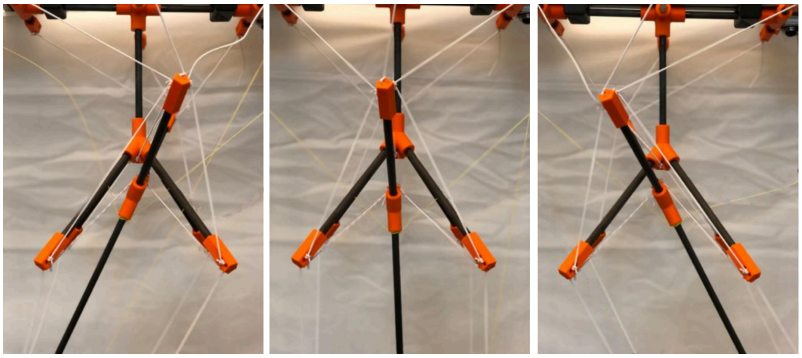

**(c)** Flexed & Extended Position

**Figure 4.4:** Tensegrity Flexural Joint: Hip (see Figure 4.2 for reference)

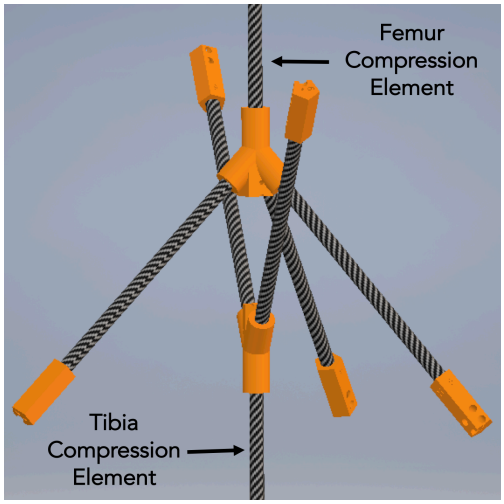


**(a)** 3D CAD showcasing the 1 Tri-joint, 1 Y-joint, and 5 Endcaps

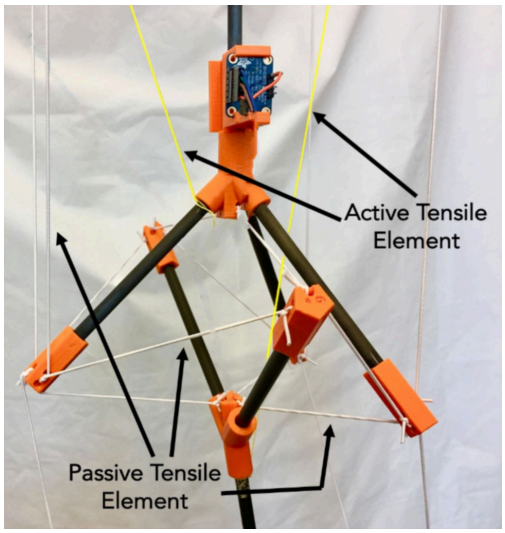


**(b)** Prototype

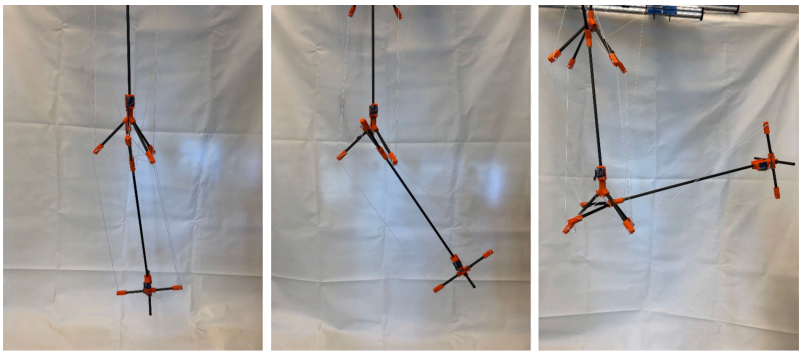

**(c)** Flexed Position

**Figure 4.5:** Tensegrity Flexural Joint: Knee (see Figure 4.2 for reference)

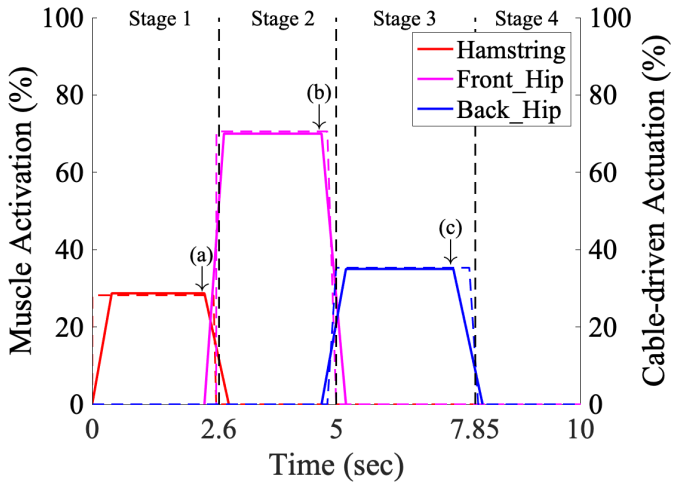


**Figure 4.6:** The applied activations by the three virtual "muscles" in the OpenSim 3.0 simulation environment (full line), and the intensity from the cable-driven actuators on the prototype (dotted lines). The varying levels of actuation (i.e., applied forces) input into the simulated models generalize an approximation for how to actuate the muscle-inspired cables in the prototype. Labels (**a**–**c**) indicate where the applied contracting muscles release.

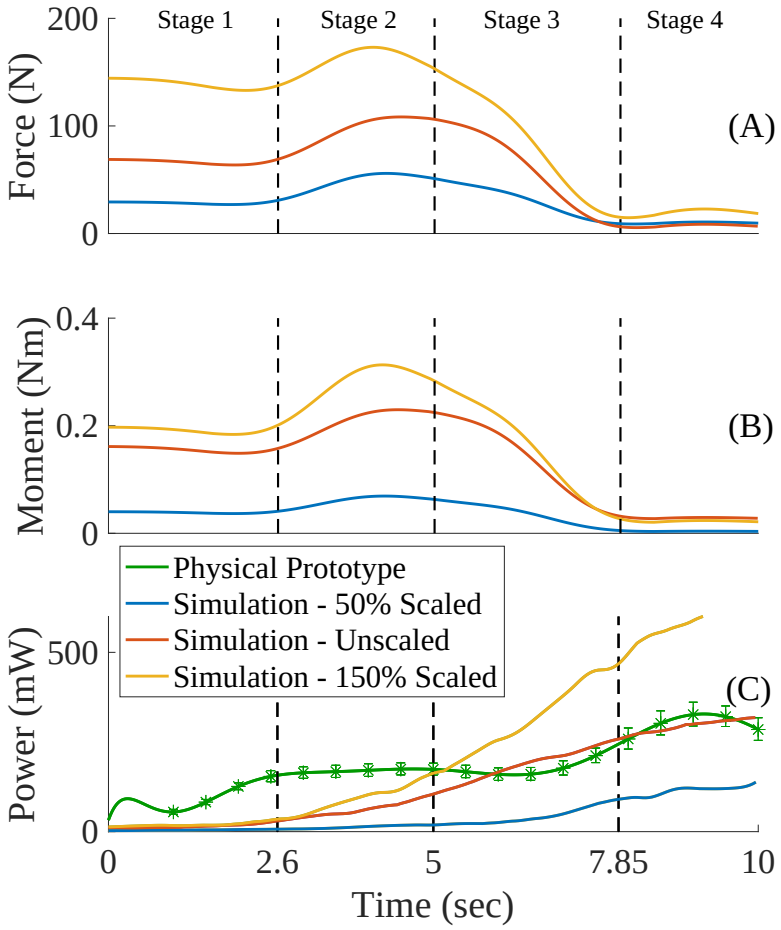


**Figure 4.7:** (**A**) Applied forces from all the active elements on the simulated model at varying sizes (50%, 100%, and 150% scales) show that a smaller model requires similar amounts of forces to replicate the four stages of gait. (**B**) Simulated moments ($N \cdot m$) on the hip joint throughout the four stages of gait estimate the required actuators. (**C**) Power consumption (mW) of the structure is similar to the simulation and the physical prototype performing the four stages of gait. The average of the few trials (solid green line) for the physical prototype created the upper and lower error bars. As we enlarge the model size, the forces necessary to produce the same motion increase. Increasing the size of the simulated models demonstrated a significant spike in overall energy consumption. It is worth noting that the 100% scaled simulation model is the same size as the physical prototype.

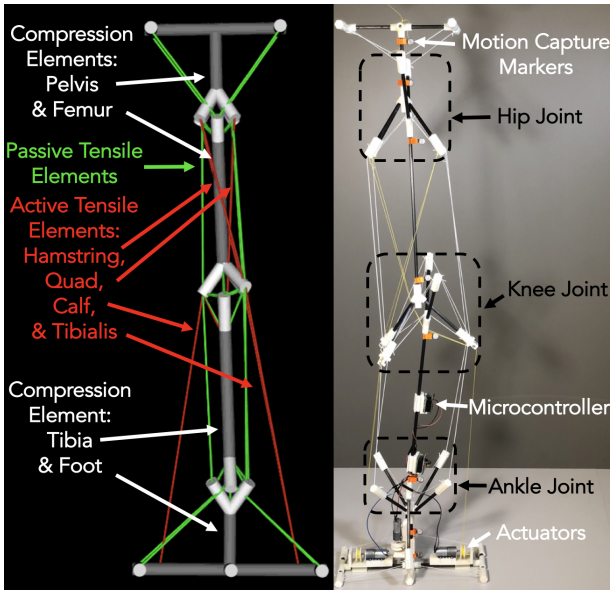


**Figure 4.8:** Current self-standing and stabilizing tensegrity structure inspired by ankle, knee, and hip joints.

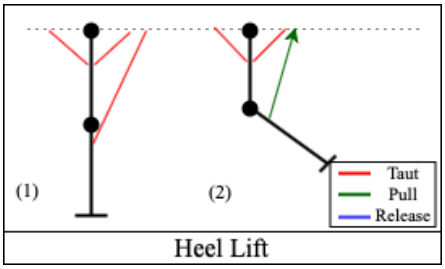


**(a)** Stage 1: Heel Lift—Contracting the hamstring

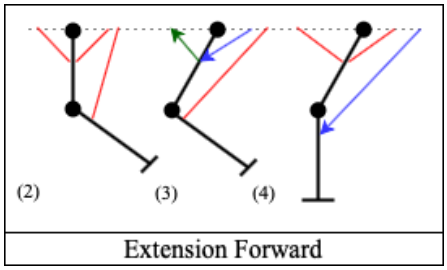


**(b)** Stage 2: Extension Forward—Contracting the iliopsoas, while releasing the gluteus maximus cable.

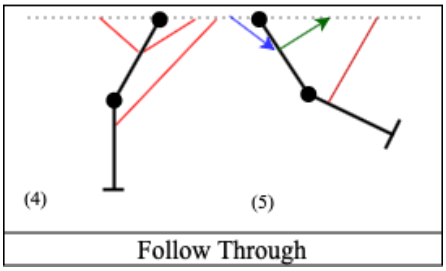


**(c)** Stage 3: Step Through—Releases the iliopsoas and contracts the gluteus maximus.

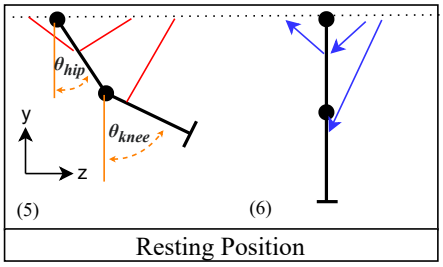


**(d)** Stage 4: Resting Position—Return back to equilibrium.

**Figure 4.9:** Outline of the active elements during the four stages of gait. Each pull (green) activates the cable-driven actuator to contract and shorten the muscle. The release of muscles (blue) reverses the direction of the actuator. In (**d**) the orange shows how the angles for the hip and knee were tracked.

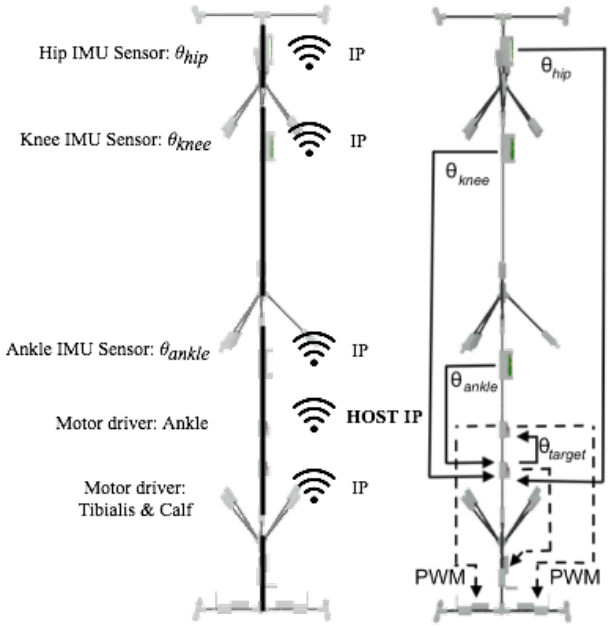


**Figure 4.10:** Each piece of hardware communicates throughout the tensegrity structure creating a self-standing localization wireless network connected with IMU sensors and motor drivers.

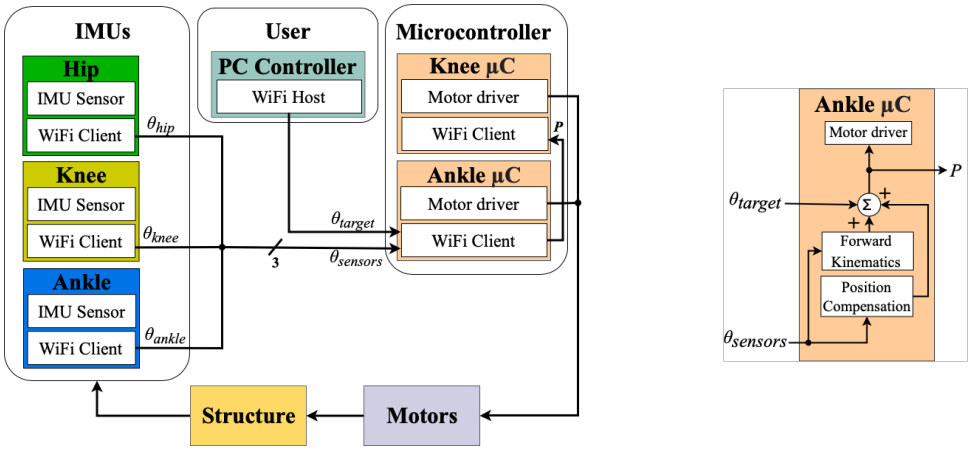


**Figure 4.11:** Block diagram (a) illustrates how the software interacts with the hardware. The tensegrity legs rely on IMU sensors for feedback on kinematic behavior. The self-stabilizing tensegrity structure interprets the angle measurements with the Ankle $\mu C$ (b) to manipulates the active tensile elements towards the desired position set by the user. Post-manipulation, the IMUs register the position change and the Ankle $\mu C$ awaits a new desired movement ($\theta_{target}$).

# Chapter 5

# Validation

## 5.1 Introduction

This chapter demonstrates the validity of the methodology that systematically analyzes models, and estimates the required dynamics to reproduce the experimental motions. Each experiment compares the effectiveness of monitoring human biomechanics and flexible-rigid prototypes through the simulation, OpenSim, with two different methods of data acquisition: optical motion capture (OMC) and wearable inertial motion capture (IMC). The experimental setup monitors the kinematics using the OptiTrack motion capture system simultaneously against wireless 9-axis IMU sensors.

## 5.2 Comparing Prototype vs. Simulation

The designs had a similar flexibility and range of motion to the human body for a specific gait-inspired experiment, as demonstrated by the kinematic results for joint angles (Figure 5.1). For the hip joint, the vectors stretch from the pelvic region to the bottom of the tibia element, and the knee's range of motion used the

lowest point of the femur to the tibia for the vectors. The structure was capable of extending the hip joint $\theta_{hip}$ flexion to approximately 40°, where human hip flexors are able to produce 35° across the sagittal plane throughout gait motions [152]. In the same plane, the knee joint, $\theta_{knee}$ was capable of flexing to 110°, which is comparable to a human with 130° of knee flexion [152]. To further the kinematic analysis, the position of the end-effectors were tracked (Figure 5.2) to result in a maximum error of 3.3% between the final positions of the simulations and the prototypes.

Figure 5.1 shows the comparison between the hip and knee rotation angles during a full gait event. The OpenSim 3.0 prediction is shown in green, the flexible–rigid manipulator is shown in red and the human leg testing in blue. Figure 5.1a shows the hip rotation angles, and Figure 5.1c the knee rotation angles along the sagittal plane. The convention used here to define the rotation angles for the hip and for the knee is shown in Figure 4.9(d—step 5). To compute the angles a vector associated with the direction of each component of the manipulator ($V_{hip}$ and $V_{knee}$) and compute the angle between that component and the unit vector $k$ associated with the $z$ axes of the Cartesian coordinate system, which is assumed to be the resting position Figure 4.9(a—step 1) and 4.9(d—step 6):

$$\theta_i = \arccos\left(\frac{\vec{V_i} \cdot \vec{k}}{|\vec{V_i}| * |\vec{k}|}\right), \qquad i \in \{hip, knee\} \tag{5.1}$$

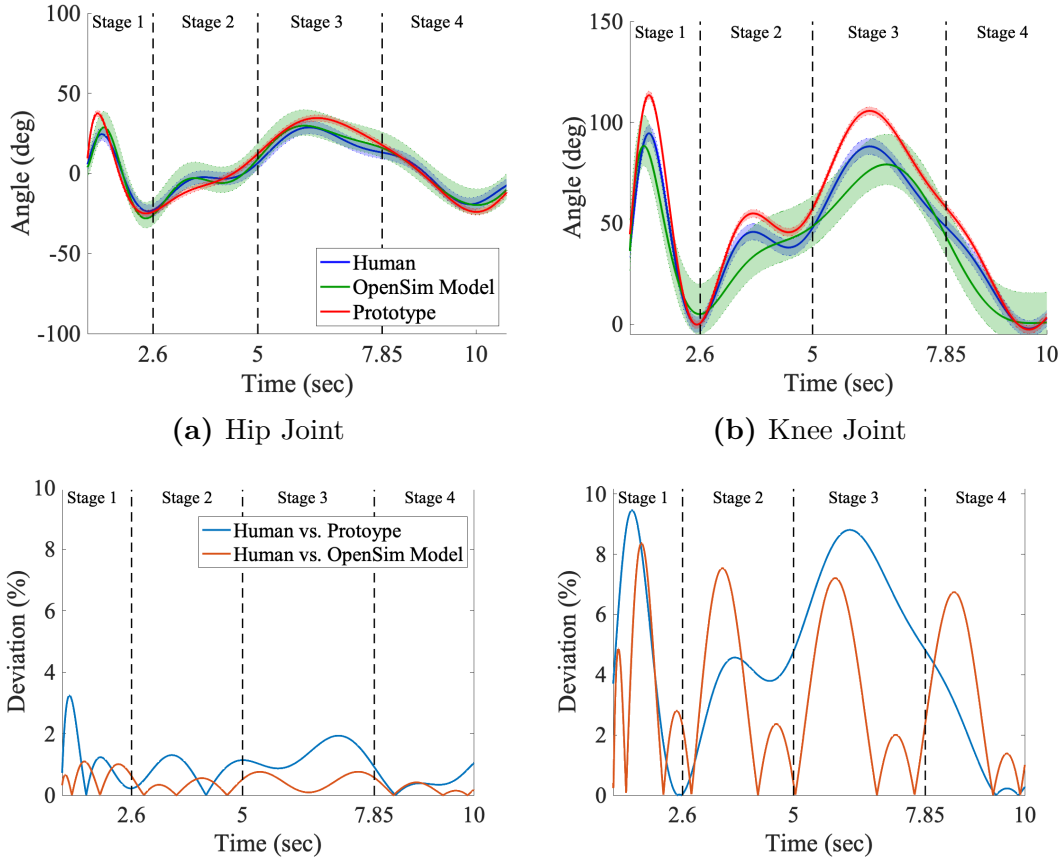


**(a)** Hip Joint

**(b)** Knee Joint

**(c)** Hip absolute error

**(d)** Knee absolute error

**Figure 5.1:** Simulated and measured angles of the hip (**a**) and knee (**b**) joints during the four stages of gait, and (**c**,**d**) the absolute errors, between angles across multiple trials (see Table 5.1). The shaded range represents the lower and upper limits of motion through simulated trials with the chosen configuration in a solid line.

All three systems demonstrated similar kinematics during the four stages of gait. Figure 5.1b show the absolute errors between the average measured and predicted hip angles and Figure 5.1d show the absolute errors between the average measured and predicted knee angles. The error between the human leg and the robotic prototype is shown in blue and the error between the human leg and the OpenSim 3.0 simulation is shown in red. It should be noted that the errors are very small. Due to the pelvic-inspired component suspended and confined to a

mounted position, there is limited variance in the range of motion resulting in a lower absolute error compared to the knee. Both the kinematics of the femur-inspired element and the large angular displacement shown in each stage of gait (Figure 4.9) effect the absolute error of the knee (Figure 5.1d). Table 5.1 indicated that the movements for both Stage 1 and Stage 3 were both the most dramatic causing the largest error for both joints. The results between the *OpenSim 3.0 model* vs. *Prototype* and *Human* vs. *Prototype* show the accuracy of replicating the recorded motions with this system. Figure 5.2 tracks the trajectory of the end effector of the femur and tibia along the sagittal axis. The Cartesian coordinates ($\vec{v}$ and $\vec{u}$) are computed using Equation (5.1) for each joint angle ($\theta$) from the start and end of the gait experiment. This demonstrates the kinematic similarities of the human, simulation, and prototype gaits.

**Table 5.1:** Maximum absolute error (%) for each stage of gait

| Human vs. Prototype Joint | Stage 1 | Stage 2 | Stage 3 | Stage 4 |
|---|---|---|---|---|
| Hip | 3.1 | 1.3 | 1.9 | 0.97 |
| Knee | 9.4 | 4.5 | 8.8 | 4.7 |
| Human vs. OpenSim 3.0 Model | Stage 1 | Stage 2 | Stage 3 | Stage 4 |
| Hip vs. Prototype Joint | 1.03 | 0.54 | 0.75 | 0.41 |
| Knee vs. Prototype Joint | 8.3 | 7.5 | 7.2 | 6.7 |

## 5.3 Custom vs. Commercial Motion Capture System

The motion capture system monitors the infared markers placed on the body and exports the Cartesian coordinates of each marker. This set of data is then imported into OpenSim to scale and interpret kinematics using the Scale and IK tool. Each experiment focuses on gait along a sagittal axis isolating the focus

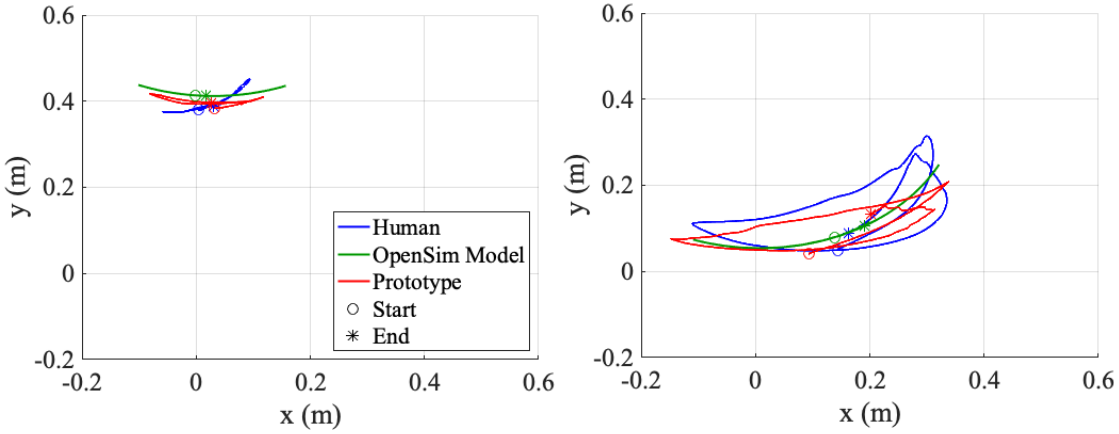


**(a)** Tracking the base of the femur (hip) **(b)** Tracking the base of the tibia (knee)

**Figure 5.2:** The bottom retro–reflective markers on the human and prototype are the motion–tracked end–effectors. Both end–effectors demonstrate similar behavior, validating the kinematics of the proposed design. During the gait motion, 'o' is the start, and the '*' is the end.

on the hip, knee, and ankle joints computing movements based off of the same parent-child hierarchy. The displacement of joints throughout time use a weight least squares error reduction (Equation 3.5) to best represent the motion within the simulation environment. The kinematics are superimposed with multiple trials averaged (Figure 5.3, 5.4 & 5.5) to validate consistent measurements during experiments. Variances throughout experiments are due to a minor drift along the sagittal plane, OpenSim's weighted least squares computation with the IK tool, and different sampling rates between the optical MoCap system (120 Hz) and the IMUs (100 Hz). It is worth noting that the optical system is down-sampled to 100 Hz for easier comparisons.

## Suspended Gait-Inspired Tensegrity Movement

The Suspended Gait-Inspired Tensegrity design has two flexural joints (knee and hip) along with three rigid bodies (pelvis, femur and tibia) inspired by the

major components of the human leg. The structure is operated and analyzed to better understand the importance of manipulation of tensile elements throughout a simplified form of human gait [20]. To achieve the gait-like trajectories, the tensegrity system shortened and lengthened the active elements that results in flexion and extension of the joints. The flexural hip joint propels the leg forward, while the hamstring releases the flexural knee joint to create the extension forward and follow through-inspired motions. During the motion, the same parent-child scheme with knee angles are dependent on the hip joint that can be directly ported to OpenSim. These movements were closely monitored and compared to the movement of a human in-place gait for one leg (Figure 3.11.b.i) [20].

The two IMUs on the model were used as a sensing network for measuring the current state of the structure and the required distance to achieve the next phase of gait. For motion capture, there were 9 IR markers used on the model. This parent-child relationship algorithm was applied to preprocess the data to be compatible with OpenSim and MoCap data was tagged and imported into OpenSim to scale the *Suspended Gait-inspired Tensegrity* model. This experiment was tracked through both of the data acquisition methods simultaneously for 10 trials with an average duration of 10 seconds. Each trial followed a gait-inspired movement and were parsed by their respective gait cycles. This work represented the motion between 0-100% and averaged both data acquisition methods discussed in this section to measure the angles in Figure 5.3.

## Self-stabilizing Leaning Movement

This flexible-rigid self-stabilizing (self-balancing) structure is inspired by lower body human musculoskeletal connections as a network of tensile elements in conjunction with rigid elements. This configuration focused on designing a robot that

achieves descent while maintaining a stable, up-right posture that would represent a paradigm shift for the artificial limbs and other assistive device research fields. While the previous model focused on the execution of a repetitive motion, the hanging model test the tensegrity model's ability to dynamically adjust to a change in stability.

The movement of the standing model involved the ankle and knee joints (Figure 3.11.b.ii.). The base of the robot provided enough stability and weight for when the leg leaned. The leg's ankle joint reached an angle displacement of 27° while the knee angle displacement was 13°. The model lowered and reached back to its upright position for 10 trials. Each trial's motion was represented between 0-100% and averaged using the same pipeline (Algorithm 2) to obtain the angles found in Figure 5.4. To compare the kinematic analysis, the optical MoCap system was used with 12 IR markers.

## Tracking Human Gait Movement

The IMUs were strategically placed to monitor the hip, knee and ankle joint as the subject walked (Figure 3.11.a.iii). The subject started by walking barefoot on a treadmill wearing a non-restricting suit equipped with 19 infrared OptiTrack motion capture markers strategically placed to fit the body segments in the simulation environment for accurate scaling. To monitor the ankle joint, an IMU was placed on top of the metatarsals. For the knee joint, an IMU was placed on the tibia directly below the patella. The hip was monitored by placing an IMU on the front of the quadriceps. The axis of each IMU was orientated in the same frontal plane as the motion capture environment, and was synchronized to record kinematics together.

Following Algorithm 2, once the IMUs were recorded for the length of a trial,

it was processed by Equation 3.8 to apply the parent-child relationship and formatted as a motion file for ID analyses. Similar to the other experiments, 10 trials recorded for the duration of 14 cycles of gait are all averaged into 0-100% of the motion (Figure 5.5). It is worth noting that 1 cycle of gait is interpreted as 0-100% of the motion resulting in 140 samples of tracked cycles of gait. Each motion file created for the experiments was passed into the ID solver to interpret joint-angles and output moments on the ankle, knee, and hip joints for both data acquisition techniques (Figure 5.6). The results from the simulation indicate a maximum of 0.073 $Nm/kg$ RSME demonstrating the potential and accuracy of using IMUs as a form of motion tracking for both robotic and human applications.

### 5.3.1 Results & Discussion

The similarities between the angle estimations from the IMUs and the optical motion capture are assessed in terms of Range of motion (ROM) and Root Mean Squared Error (RMSE):

$$ROM = [\wedge(\theta_{MoCap}) - \vee(\theta_{MoCap})] - [\wedge(\theta_{P\rightarrow C}) - \vee(\theta_{P\rightarrow C})] \tag{5.2}$$

$$RMSE = \sqrt{\frac{\sum_{i=1}^{S}(\theta_{MoCap_i} - \theta_{P\rightarrow C_i})^2}{S}} \tag{5.3}$$

where $S$ is the total number of samples, $\vee$ represents the minimum, $\wedge$ represents the maximum, $\theta_{MoCap}$ refers to the motion captured angles and $\theta_{P\rightarrow C}$ are the joint angles after applying the parent-to-child relationship. The results from MoCap are calculated with the IK tool and down-sampled to match the sample rate of the calculated IMU sensor. Each experiments' motion (Figure 5.3.a, 5.4.a & 5.5) takes the mean of 10 trials, and superimposes their results to illustrate the similarity in joint-angles and moments between the optical MoCap and IMU processed using

**Table 5.2:** Range of motion captured during experiments

| Model | Joints | Range of Motion (°) |
|---|---|---|
| Suspended Gait-inspired Tensegrity | lh | $(-20, 20)$ |
| | lk | $(-2, 60)$ |
| Self-stabilizing Leaning Tensegrity | lk | $(0, 15)$ |
| | la | $(-30, 2.5)$ |
| Human Model | lh, rh | $(10, 45)$ |
| | lk, rh | $(-10, 70)$ |
| | la, ra | $(-10, 25)$ |

the pipeline (Algorithm 2) in OpenSim.

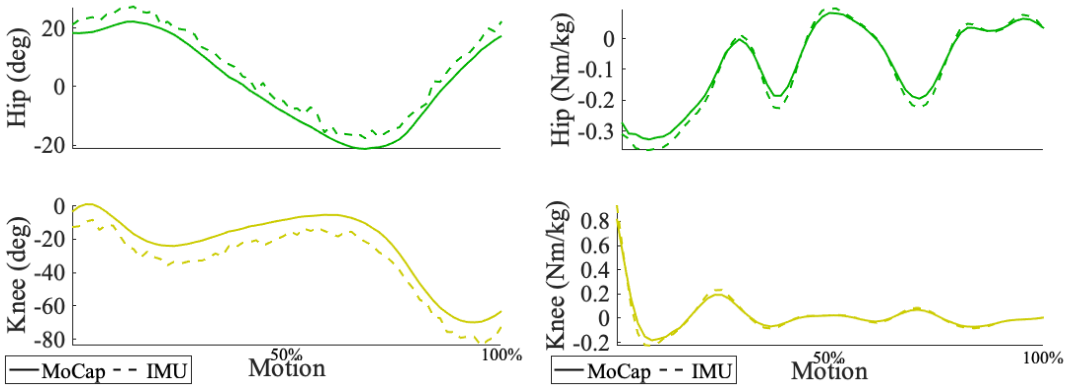


**(a)** Measured Angles **(b)** Simulated Moments

**Figure 5.3:** Average hip and knee angles (a) during 10 successive experiments using the suspended tensegrity structure shown in Figure 3.8(i). The average ROM error comparing optical MoCap to IMU for the hip is 1.5° (SD $\simeq$ 1°), and knee 4.6° (SD $\simeq$ 1°). The simulated moments for the optical MoCap and IMUs (b) come from the averaged measured angles of the suspended tensegrity throughout an in-place gait-inspired motion with an average RSME of 0.11 ($Nm/kg$). For color coordination for each joint refer to Figure 3.11a.i.

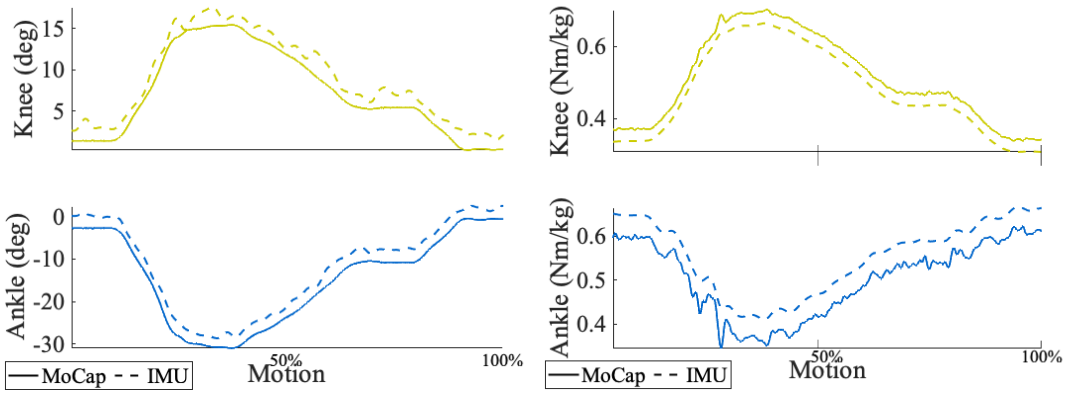


**(a)** Measured Angles **(b)** Simulated Moments

**Figure 5.4:** Average knee and ankle angles (a) during 10 successive experiments using the self-stabilizing leaning tensegrity structure shown in Figure 3.8(ii). The average ROM error comparing optical MoCap to IMU for the knee is 3.4° (SD $\simeq$ 1°), and ankle 2.8° (SD $\simeq$ 1°). The simulated moments for the optical MoCap and IMUs (b) result from the averaged measured angles of the suspended tensegrity throughout an in-place gait-inspired motion with an average RSME of 0.03 ($Nm/kg$). For color coordination for each joint refer to Figure 3.11a.ii.

Ranges from each joint vary across the three models discuss in this work (Table 5.2). Each joint range is dictated by the parent joint acting as the reference point of each measurement. The hip joint provides the reference point axis for the knee joint, which provides the reference point for the ankle joint (Equation 3.8). The local maximum and minimum angles of each joint can be used to annotate which phase of the gait cycle these respective angles are correlated with.

The Suspended Gait-inspired Tensegrity experiment had a max RMSE of 10.2° and ROM of 4.6° for the IMUs when compared directly against the IK results from optical MoCap (Table 5.3). Once the simulation environment interpreted the averaged angles shown in Figure 5.3 as motion files, and solved the ID results, the max RMSE between the two forms resulted in 0.18 $Nm/kg$ (Table 5.5). The Self-stablizing Leaning Tensegrity experiment had a max 3.01° RMSE and 3.4° ROM for the IMUs when compared directly against the IK results from optical MoCap (Table 5.3). Similar to the previous experiment (Fig 5.4), the ID results found

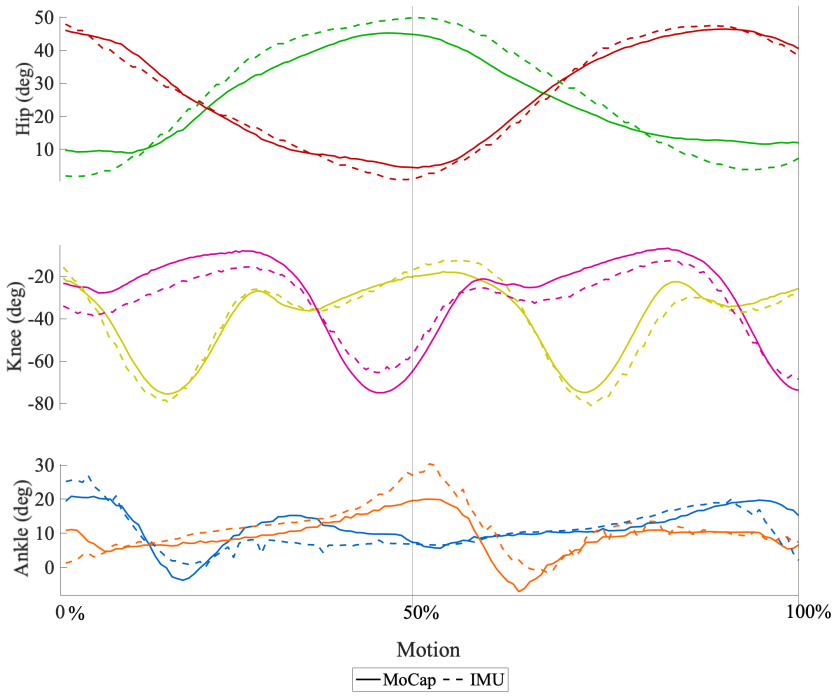


**Figure 5.5:** Average hip, knee, and ankle angles (a) during 10 successive experiments tracking human gait shown in Figure 3.8(iii). The average ROM error comparing optical MoCap to IMU for all the joints is 6.14° (for individual joint RSME and ROM error see Table 5.5). For color coordination for each joint refer to Figure 3.11a.iii.

the max RMSE between the two forms resulted in 0.034 $Nm/kg$ (Table 5.5). The human gait experiment (Figure 5.5) tracked a complex movement primarily focused on 6 joints along the sagittal plane resulting in a max 7.35° RMSE and 12.45° ROM for the joint-angles (Table 5.3). The ID results calculated a max 0.073 $Nm/kg$ RMSE demonstrating the potential use of OpenSim with IMUs data acquisition for human biomechanic analysis (Table 5.5). Each experiment (Figure 5.3, 5.4 & 5.5) calculated the maximum standard deviation across all trials with the averaged measured angles. These sensing algorithms demonstrate the potential for estimating gait patterns through wearable sensing.

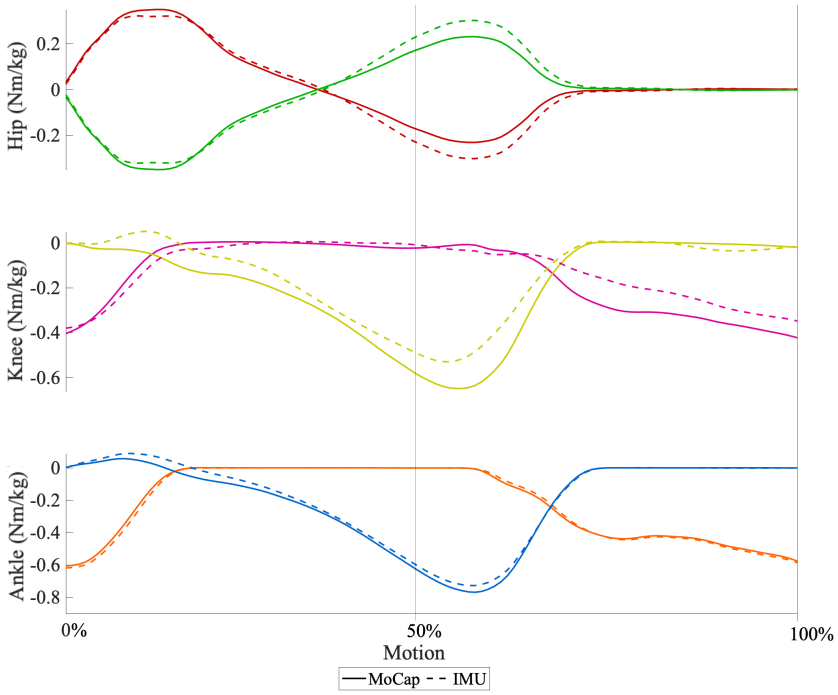


**Figure 5.6:** The simulated moments for the optical MoCap and IMUs based off of the averaged measured angles (Figure 5.5) throughout the human gait motion tracking experiment with average RSME of 0.04($Nm/kg$). For color coordination for each joint refer to Figure 3.11a.iii.

## 5.4 Applied Machine Learning for Biomechanical Analysis

The primary goal of this work extends the typical application of gait detection or stance-swing transitions to create a model that can accurately predict the phase of gait using joint angles. The author believes understanding a complex breakdown of individual phases of gait (Figure 5.8: Data Labeling) compared to just toe off, foot flat and heel off has potential for more applications (e.g., prostheses, exoskeletons, virtual reality, etc.). Other researchers have applied machine learning to detect a variety of motions with a single sensor which I believe has an different and more general application than this work [153]. It is a well-

**Table 5.3:** RMSE & ROM Errors for generated motion files. The Experimental Movements are: $A$: Suspended Gait-inspired Tensegrity, $B$: Self-stabilizing Leaning Tensegrity, $C$: Human Gait

| **Exp. Setup** | $\theta_{lh}(^\circ)$ | $\theta_{lk}(^\circ)$ | $\theta_{la}(^\circ)$ | $\theta_{rh}(^\circ)$ | $\theta_{rk}(^\circ)$ | $\theta_{ra}(^\circ)$ | $Avg.(^\circ)$ |
|---|---|---|---|---|---|---|---|
| **RMSE** | | | | | | | |
| $A$ | 4.0452 | 10.2116 | X | X | X | X | 7.1284 |
| $B$ | X | 1.8306 | 3.0109 | X | X | X | 2.4208 |
| $C$ | 2.5558 | 7.3520 | 3.5846 | 4.4574 | 5.1500 | 3.7519 | 4.4753 |
| **ROM** | | | | | | | |
| $A$ | 1.4635 | 4.6125 | X | X | X | X | 3.0380 |
| $B$ | X | 3.3782 | 2.8023 | X | X | X | 3.0903 |
| $C$ | 5.0607 | 12.4518 | 1.2148 | 5.8144 | 11.2868 | 1.0232 | 6.1420 |

**Table 5.4:** Rigid Approximations for the custom models. These values are basic calculations of the required moments to manipulate the joints on each experiment (Figure 3.11.b). These range of moments neglected tensile forces to ensure that the output from the simulation environment were sound and reasonable.

| **Experiment** | $l[m]$ | $l_{CM}[m]$ | $m[kg]$ | $I[kg \cdot m^2]$ |
|---|---|---|---|---|
| **Gait-Inspired** | | | | |
| Hip | 0.5766 | 0.2110 | 1.8892 | 0.314 |
| Knee | 0.4064 | 0.3700 | 1.1674 | 0.143 |
| **Self-stabilizing** | | | | |
| Knee | 0.676 | 0.2510 | 1.9592 | 0.6094 |
| Ankle | 0.3764 | 0.4100 | 1.5674 | 0.4643 |

known challenge to generalize the required moments from phase to phase for all human subjects so I confined my study on the sagittal plane.

The primary goal of this work extends the typical application of gait detection or stance-swing transitions to create a model that can accurately predict the phase of gait using joint angles. The author believes understanding a complex breakdown of individual phases of gait (Figure 5.8: Data Labeling) compared to just toe off, foot flat and heel off has deeper insights for applications such as prostheses, exoskeletons, virtual reality, etc. Machine learning has been applied to detect a variety of motions with a single sensor which I believe has an different

**Table 5.5:** RMSE Errors for ID Results. The Experimental Setup movements are: $A$: Suspended Gait-inspired Tensegrity, $B$: Self-stabilizing Leaning Tensegrity, $C$: Human Gait. All of the units are $[Nm/kg]$

| **Exp. Setup** | $l_h$ | $l_k$ | $l_a$ | $r_h$ | $r_k$ | $r_a$ | $Avg.$ |
|---|---|---|---|---|---|---|---|
| $A$ | 0.0367 | 0.1845 | X | X | X | X | 0.1106 |
| $B$ | X | 0.0341 | 0.0338 | X | X | X | 0.03395 |
| $C$ | 0.0338 | 0.0666 | 0.0151 | 0.048 | 0.073 | 0.0269 | 0.0439 |

and more general application [153, 107]. Since it is a challenge to generalize the required moments from phase to phase for *all* subjects, the study is confined on the sagittal plane. The process for preparing each data set began with using OpenSim, a multi-body biomechanic simulation package [24] and bioMechZoo, an open-source toolbox for analyzing and visualizing movement [114] to accurately label the joint-angle coordinates and phase of gait in Section 5.4.1. To make sense of the aggregated data set, machine learning classification algorithms such as random-forest [154, 155] was implemented to correlate all of the joint-angle recordings with a phase of gait [77] in Section 5.4.2. This section demonstrates that even with a large set of joints being tracked for a cyclical movement such as gait along the sagittal plane, there is no significant requirement for wearing additional sensors. Rather, there exists options to reduce the number of joints monitored and thereby yield which phase of gait with a range of confidence (See Table 5.7). To further the extraction of this same data, ID from OpenSim was used to produce a relationship between phase of gait, joint angles, and required moments, creating a valuable tool for future prosthetic, exoskeleton or biomechanics applications [97].

### 5.4.1 Data Preparation

This study considered one hundred and nine healthy adults who range in physical characteristics (e.g., height, weight, mass, age). Two public databases were

used to cumulatively provided 4079 full cycles of gait, and our own database, which provided 124 cycles of gait. Moissenet database [21] used 51 participants, Horst database [22] used 56 participants and our database used 2 participants (See Table A.7). The experiment used a set of in-house developed 9-degrees of freedom orientation IMU sensor with a 3-axis magnetometer, 3-axis gyroscope, and 3-axis accelerometer that used the Madwick sensor-fusion algorithm to calculate angular displacement and wirelessly transmit the information to a remote host using the TCP protocol [109, 140]. Figure 5.7 shows the correlation between the age, height and weight for all of the participants.

Since each database had its unique recording strategy (e.g., different marker placement and different sampling rate), the experimental data was preprocessed using Algorithm 3 to include marker numbers, frames, samples, mass, gender, and height into a single matrix representing each subject's biometrics
[156]. For example, the Moissenet and our own databases were sampled at $100Hz$, while the Horst database was recorded at $250Hz$. The Horst database was down-sampled to match the other two sets of data and generate a training data set that consists of over $700,000$ samples at $100Hz$. It is important to note that the markers and their locations for both Moissenet & Horst were interpreted by BioMechZoo solvers to output a joint-angle relationship that yielded similar ranges of motion. The Moissenet & Horst data-basis included foot-ground reaction forces. The ground reaction force was simulated using "the simulated force plate" component available in OpenSim.

The organization of the data structure for the recorded motion ($T$) shown in Equation 5.4, contains a Cartesian markers ($C^i_{m,f};\ \ m \in \{x, y, z\}$), frame number ($f$), and individual trials or samples ($i$).

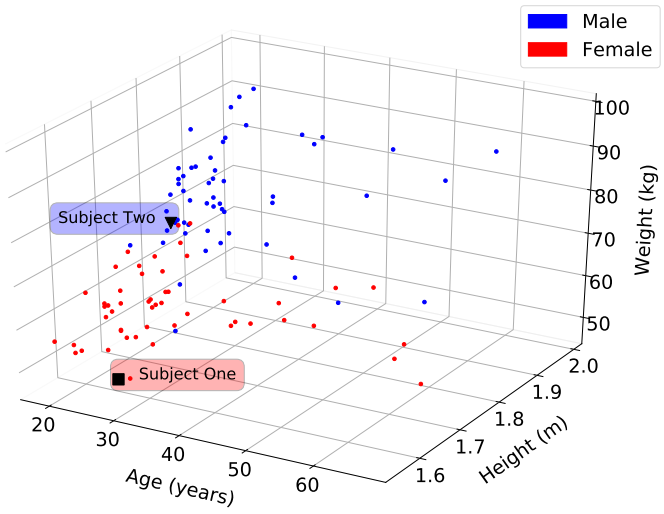


**Figure 5.7:** Distribution of all 109 participant information regarding age (years), height (m), weight (kg), and gender (e.g., blue for male, red for female). This large variation is a challenge for classification algorithms when every subject varies. For distinct comparisons, I chose 2 subjects (Subject One is red, and Subject Two is blue) at random with different height and weight. Subject One is a 28 year old female, 1.56 m in height and weighing 50 kg. Subject Two is a 23 year old male, 1.76 m in height and weighing 73 kg. See supplementary data in Table A.7.

$$T = \begin{bmatrix} C^1_{x,1} & C^1_{y,1} & C^1_{z,1} & \dots & C^1_{x,2} & \dots & C^1_{m,f} \\ C^2_{x,1} & C^2_{y,1} & C^2_{z,1} & \dots & C^2_{x,2} & \dots & C^2_{m,f} \\ \vdots & \vdots & \vdots & & \vdots & & \vdots \\ C^i_{x,1} & C^i_{y,1} & C^i_{z,1} & \dots & C^i_{x,2} & \dots & C^i_{m,f} \end{bmatrix} \tag{5.4}$$

Figure 5.8 illustrates the process of extracting Cartesian coordinates from raw marker data and convert them into joint-angles. This means that the system in this work is capable of accepting different sources of motion capture, and the pre-processing pipeline from Algorithm 3 that is then converted into the data sets as a consistent parent-child joint-angle relationship for all subjects. To clean up the data set, the scripted Equation 5.5 to determine the joint-angle representation along the sagittal plane (Figure 5.9) for the lower extremity joints [21, 22]. After the joint-angles were found for all participants, the alignment is verified for all

**Algorithm 3:** Data Preparation Pipeline. This extracts Cartesian coordinates from raw marker data (Moissenet, Horst or ouwer own experiment) and convert them into joint-angles

**Input**: Marker Data
**if** *File Type == .mot* **then**
    OpenSim Inverse Kinematics → Joint Angles ($\theta$)
    OpenSim Inverse Dynamics → Moments ($M$)
    Data Annotation in OpenSim
**else if** *File Type == .c3d* **then**
    biomechZoo Inverse Kinematics → .zoo → Joint Angles ($\theta$)
    Data Annotation in Mokka
*Target* Phases of Gait ($P$) from Data Annotations → Labeled Joint Angle *Features* ($\theta$)
Aggregate Participant Information ($S$)
**Output:** Joint Angle Feature Extraction

calculated joint-angles to ensure they are in the same range of motion.

$$\theta_{2D} = \frac{180}{\pi} cos^{-1}\left(\frac{(C_{x,1} \cdot C_{x,2}) + (C_{y,1} \cdot C_{y,2})}{\sqrt{(C_{x,1})^2 \cdot (C_{y,1})^2} + \sqrt{(C_{x,2})^2 \cdot (C_{y,2})^2}}\right) \tag{5.5}$$

$$S = \begin{bmatrix} g^1 & m^1 & h^1 & a^1 \\ \vdots & \vdots & \vdots & \vdots \\ g^i & m^i & h^i & a^i \end{bmatrix} \text{ and } L = \begin{bmatrix} P & S & \theta_{2D} \end{bmatrix} \tag{5.6}$$

In some cases there exists multiple trials of the same subject, but in the event the participant changed, all of the subjects attributes (S): gender (g), mass (m), height (h), and age (a) were assigned as a new person. After the data sets have been labeled for phase of gait (P), subject attributes (S), and joint-angle kinematics ($\theta_{2D}$), the process transitioned into training both the Gait Prediction and Moment Transition Predictions (Figure 5.10).

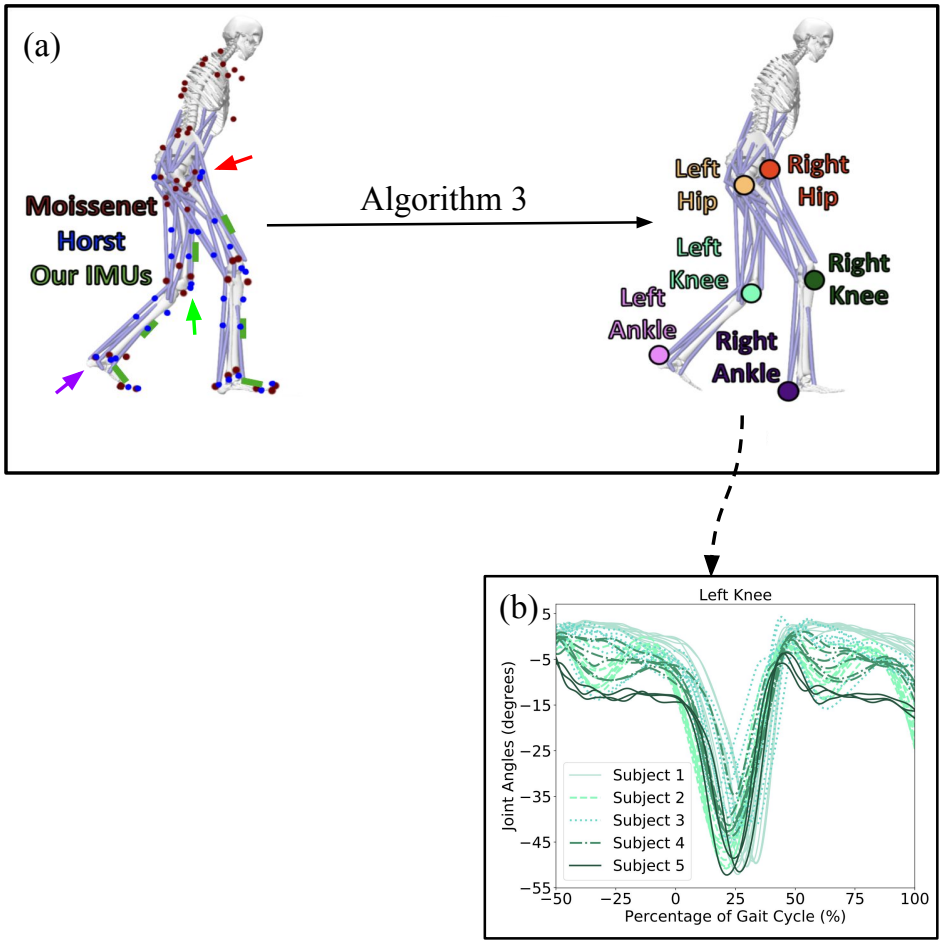


**Figure 5.8:** Each data set included unique configurations of markersets (T) to record the kinematics of each subject. (a) The location of the optical motion capture markers used by the Moissenet (red) and Horst (blue) databases, as well as the placement of our IMUs (green). Algorithm 3 was used to convert the marker data into a motion file interpreted by the biomechanic simulators. (b) The left knee angles throughout an experiment for 5 random subjects

### 5.4.2 Classification Techniques & Algorithms

Machine learning automates the process of interpreting large sets of data to learn and make estimations [157] as well as construct a model to perform data-driven classifications. One of the primary goals of this work was to create a model that can accurately predict the phase of gait using joint angles. The model is

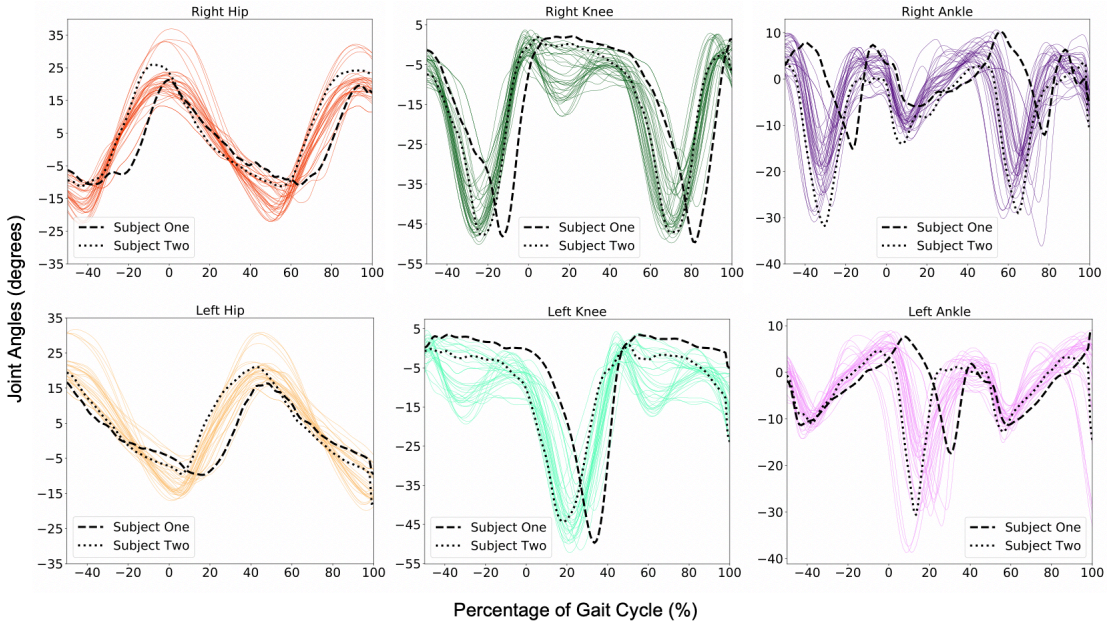


**Figure 5.9:** Joint angles are calculated using Equation. 5.5 using biomechZoo and OpenSim's marker set for five participants. The dashed lines represent the averaged joint angles for Subject One, and the dotted lines show the averaged joint angles for Subject Two. It is clear from this figure that both subjects have different ranges of motion during gait cycles (i.e., Subject Two has more ankle flexibility than Subject One), but still show a general pattern of gait. It is worth noting that the color scheme remains consistent throughout all other figures for each joint (e.g., right hip: red, left hip: orange, right knee: green, left knee: teal, right ankle: purple, left ankle: pink).

trained to find a correlation between the input *features* (i.e., the observed and recorded input data) and the output *targets* (i.e., different phases of gait). This correlation is used to calculate targets for stand-alone or unlabeled features. The accuracy of each model is evaluated by interpreting how well the correlation can be found by the algorithm to predict the target using the features with cross validation.

In this work cross-validation was used to quantify the performance of each model. This process split a certain percentage of the labeled data to use as test data, while the remaining data was used to train a model [120]. The training

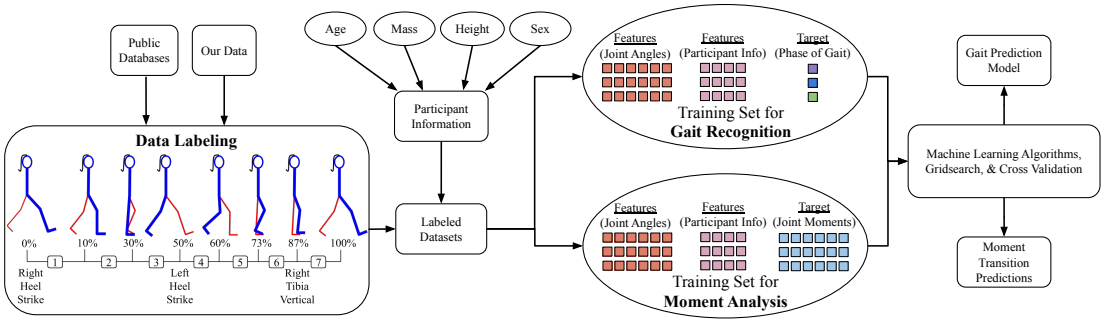


**Figure 5.10:** System overview illustrating the process from acquiring the data to exporting a model for gait recognition. The process begins by importing the data from either public databases [21, 22] or our own OpenSim simulated data. The features, or joint angles, are extracted into a labeled data set that simultaneously analyzes the moments for each phase of gait, and cross-validation to create a test-split for the Gait Classification Model. After the Gait Classification Model has been loaded, different feature combinations are tested to yield the optimal feature combination (minimum joint angles) along with Grid Search to find the optimal parameters for an Evaluated Model to best predict phases of gait.

data is used as an input into the model, and the output was compared to its observed target to evaluate the accuracy against the other portion of the data set. Cross-validation iterates through the set of data multiple times, where each interval selects a different set of data samples to test, providing a more consistent performance metric of the entire model [120]. The calculations from cross validation were used as a metric for accuracy to compare with the outputs of each model trained.

The $k$-Nearest Neighbors algorithm was used to classify the test features based on the most frequent phase of gait of their $k$ surrounding neighbors, or closest data samples [122]. The parameter, $k$, defines how many neighbors were used in each classification. A relatively larger $k$ results in a more accurate classification due to a larger scope of data. This reduces the effect of outliers and erroneous data for each prediction. The KNN algorithm has been used in other instances of training models for gait recognition based on different bio-mechanic features,

including accelerometer data [158], ground reaction forces [159], and human gait shape analysis [160].

To find the nearest neighbors of each test sample, the Euclidean distance, $D$, was calculated between the feature sets of the test and already classified samples [161]. Each feature can be represented as:

$$f = (f_1, f_2, ...f_n)$$

with $n$ representing the number of features in each sample, and every $f_n$ representing one feature. A feature vector for one sample combines all relevant features for training:

$$f_v = [P, f_1, f_2, ..., f_n]$$

$$f_s = \begin{bmatrix} P^i & \theta_1^i & S_1^i \\ P^1 & \theta_1^1 & S_1^1 \\ P^2 & \theta_2^2 & S_2^2 \\ \vdots & \vdots & \vdots \\ P^n & \theta_1^n & S_1^n \end{bmatrix}$$

The distance $D$ between the test feature set $x$ and the already classified feature set $y$ can be represented with the following formula:

$$D(x, y) = \sqrt{\sum_{i=1}^{n}(x_i - y_i)^2} \tag{5.7}$$

where the iterator, $i$, increments for every feature used to train the model [161]. Equation 5.7 was evaluated for all training data samples, $y$. The number of samples ($k$) used in the training data set with the smallest distance ($D$) was selected as the test sample's $k$ nearest neighbors. The mode target value, or most frequent phase of gait within the selected neighbors, was used as the classification

of the test sample $x$ (Figure 5.11) [122]. This process was repeated to predict a phase of gait for each test feature set. Cross-validation repeats until all 10 folds and splits are iterated and completed. Generally, as $k$ increases, the accuracy of the prediction increases as more data points are considered for the final classification. Decreasing $k$ heightens the effect of inaccurate data on classifications; the balance for an ideal value of $k$ is described using GridSearch. GridSearch finds specified parameter values through an exhaustive search process [121] (Table A.1). It sorts through all possible combinations of each parameter and finds the optimal values. Both GridSearch and feature extraction optimize the parameters of the model and the features considered to heighten the efficiency for training.

This part of the process used GridSearch to programmatically iterate through different combinations of parameter values (Table A.1) to find the ideal values to run the model with [162]. When applied to the KNN algorithm, it varies the number of neighbors in each classification, $k$, to find a balance between the model over-fitting and under-fitting the data. If the number of neighbors was small, the effect of noise on the classification become larger since the model only learned from a small subset of neighbor samples. When outliers heavily influence the model, there is a bias towards the minor details of the data (over-fitting) rather than finding a general trend [163]. However if $k$ is large, the opposite occurs since every test sample will be classified to the target (under-fitting). This happens to be more frequent than a smaller k in the overall training set, ignoring underlying trends in the data [163]. Finding a balance of the value of $k$ is crucial to achieve an accurate and precise model.

This work used the CART algorithm to focus on creating a decision tree that classifies the test samples [164]. Decision trees are commonly used in many situations where supervised learning is practical: forming gait pattern models using

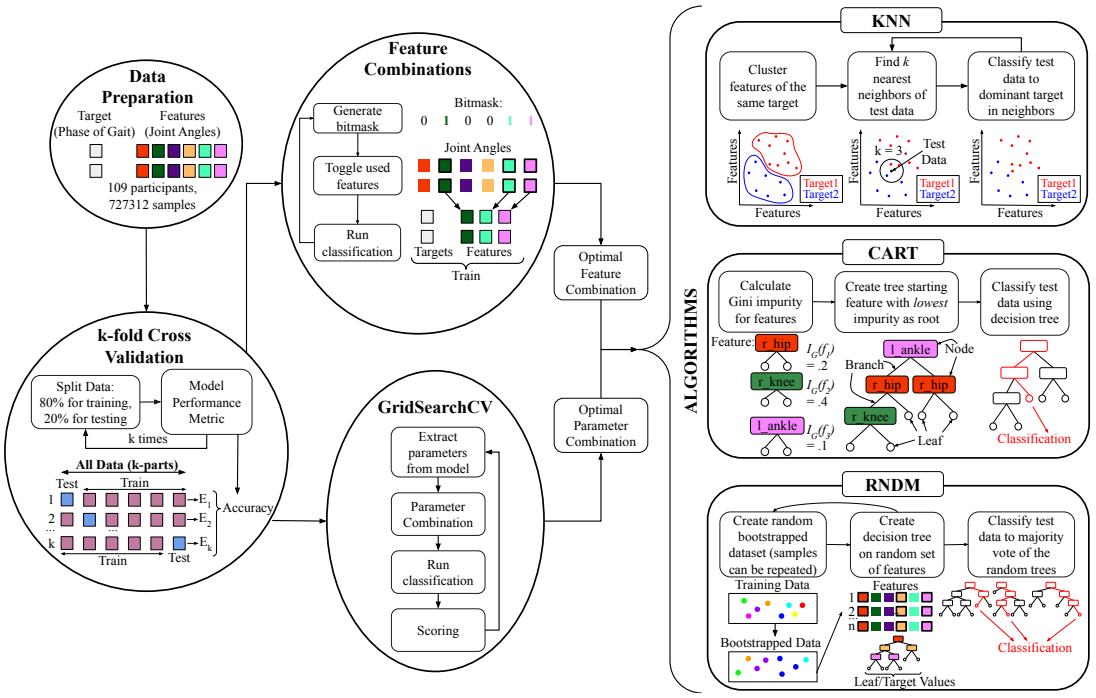


**Figure 5.11:** Machine learning pipeline for the labeling, splitting, and classification of data to optimize the accuracy of the gait recognition model. The process begins with the preparation of data, where the target, or phase of gait, is tagged onto a feature set of joint angles. Before classification, the labeled data set is split between training and testing to reduce variance and support a more generalized performance metric of each algorithm. To optimize each algorithm, a feature split and parameter tuning is iterated through. Each feature and parameter combination is then run through the preferred machine learning algorithms.

other features such as inhibitory factors of an injury [165], contact forces and angular velocity [166], as well as step length, walking speed, and stride time [167].

Each tree consists of nodes, branches, and leaves. Nodes are known as a "decision", or a comparison or split made on a specific feature in the data set. Branches are the outcome of the decision made by the node. A leaf is a node at the end of the tree that does not have branches extending from it. It is important to note that leaf nodes do not make decisions. Each leaf represents a target or a specific phase of gait. When making a classification, the data presented in this work's test feature set compares each node by traversing along the corresponding branches until it reaches a leaf node [164].

When training quantitative data, each node splits at a specific feature value. In this case, a node concerning right hip angles could split at $\theta = 20$. This creates the left branch at $\theta < 20$ for the right hip node, and $\theta > 20$ for the right branch. The ideal split yields both branches as a completely homogeneous pool of data points with the same target. Each branch splits into more nodes until every leaf node is either a product of a perfect split or until the tree reaches the maximum depth or width as specified by the parameters. The Gini impurity (I) is a quantitative measure of how accurate a split is. Ideal splits have a Gini impurity value of 0 [168], and is calculated as follows:

$$I = 1 - \sum_{i=1}^{t} (p_i)^2 \tag{5.8}$$

where $t = 7$ is the number of targets, and $p_i$ is the probability of selecting a data point with target $i$ within the entire data set.

The feature with the smallest Gini impurity is chosen as the root of the tree. In other words, if one were to randomly classified according to the target distribution of the data set, the feature with the smallest possibility of incorrect classification

is the root (see Figure 5.11) [169]. Once a feature is selected as the root node and splits according to the smallest Gini impurity value, choosing the next node and split is repeated with the data subset of each branch until a complete tree has formed. As seen in Figure 5.11, the classification in a decision tree followed the splits made by the nodes for a test feature set until a leaf node, or target, is reached.

The parameters of maximum depth and width of a decision tree prevent the common problem of overfitting in decision trees [164]. Suppose the tree grew until every split reaches an impurity of 0. In that case, every feature set likely traces a unique path to an individual leaf node due to noise in the data, making the classification overfitted and heavily affected by every outlier. To prevent this, one needs to restrict the number of splits and nodes through a tree's maximum depth and width. GridSearch iterates through different threshold values, so the parameter values shown in Table A.1 avoid underfitting and overfitting.

The random forest algorithm uses many different decision trees, as constructed in the CART algorithm, to create a forest [123]. The most frequent classification made among all the decision trees in the forest is the classification of test data points [123]. The logic behind using a forest of trees formed by randomly selected data samples and features is that the entire forest will have a low correlation between each tree. The product of uncorrelated models is far more accurate than any individual prediction. Similar to the wisdom of crowds, trees with erroneous data are protected by a more significant amount of trees with more accurate models.

The random forest algorithm began by developing each decision tree by creating a bootstrapped data set as portrayed in Figure 5.11 [123]. With repetition, a set of data samples randomly selected from the entire data set is the bootstrapped

data set that will form the tree. Every bootstrapped data set has the same number of samples as the entire data set, so that most bootstrapped sets include the repetition of random samples.

**Algorithm 4:** Classification of phase of gait in relation to joint angles using Random Forest.

**for** *Number of trees, t* **do**
- Create a random set of samples, $R$
- Select a subset of $N$ features, or joint angles ($\theta_{2D}$), from $R$
- Calculate Gini impurity, $I$, for $N$ using Equation 5.8
- Form decision tree starting with nodes of lowest $I$

**while** *Tree height != Max height or Tree width != Max width* **do**
- Calculate $I$ for remaining features, or $\theta_{2D}$
- Select feature with lowest $I$ as next node
- Branch node with lowest weighted $I$

Use most frequent output of the $t$ trees as test data classification

**Output:** Random Forest Classification Model

For each bootstrapped data set, decision trees were formed with a random selection of $m$ features. Typically $m = \sqrt{n}$, with $n$ being the total number of features in the data set (Figure 5.10). The process of creating a decision tree (Algorithm 4) uses each tree formed from calculating Gini impurity to determine the order of features as nodes and the optimal split per node. The process of building different bootstrapped data sets and creating decision trees with random subsets of features for each bootstrapped group repeats until the maximum number of trees $t$ is reached. When classifying a test sample with the random forest algorithm, a test feature set serves an an input into all the decision trees in the forest. The most frequent target output of the trees is the classification derived from the test data.

The random forest algorithm is optimized using the parameters $m$, the number of features used in each tree, and $t$, the number of trees in a forest (Table A.1). A GridSearch through both these parameters usually reveals an increase in accuracy

with the typically selected value of $m = \sqrt{n}$, and a larger $t$ to account for more significant variation in datasets. GridSearch is essential to prevent underfitting and overfitting in the RNDM algorithm due to the randomness of sample and feature selection.

### 5.4.3 Extra Trees Regressors

Regression is another approach of supervised machine learning that outputs numerical values as a target, rather than as a category [170]. The previous KNN and decision tree algorithms are applied as regression techniques by changing the target from categories into continuous values. For example, a KNN classification can be turned into regression by averaging the numerical targets of the $k$ nearest neighbors rather than taking the most categorical frequent target. Similarly, the leaves become prediction values rather than categories in a regression algorithm in algorithms with decision trees.

The extra trees algorithm is very similar to the random forest algorithm, creating many decision trees to form a forest. However, there are two critical differences between random forest and extra trees. Extra trees do not use a bootstrapped dataset like random forest. Each decision tree was formed by every sample in the entire training set [171]. Additionally, the extra trees algorithm uses a random split while creating decision trees, rather than calculating the optimal split with weighted Gini impurities like a typical decision tree [171]. Although, it is essential to note that extra trees still use Gini to calculate feature importance. Predictions in extra trees are made by averaging the output of all the trees in the forest for every test sample set [171]. When employing GridSearch in extra trees regression, the same parameters iterated through during the random forest algorithm are optimized (Table A.1) so that the decision trees that make up the forest do not

underfit or overfit the dataset.

### 5.4.4 Gait-phase Classification

The classification algorithms (KNN, CART, Random forest) use the feature set that included joint angles (right and left hip, knee, and ankle) and participant information (e.g., height, mass, gender, age). The feature set comprises 10 individual features, 6 joint angles, and 4 participant attributes. The target is the individual phase of gait for each data sample. This work employs a 10 fold cross-validation and a 20/80 train-test split across all models when evaluating accuracy. The data is iterated 10 separate times during cross-validation to evaluate the accuracy. Each iteration selects a different 20% portion of the data set to reserve as sample test data points while the other 80% is selected as training data for the model.

Before selecting specific algorithms to use, the mean accuracy (with the standard deviation) is bench-marked in Table 5.6 using cross-validation on 10-fold experiments for a sample set employing all available features to help us narrow the chosen algorithms to KNN, CART, and RNDM. It is important to note that the parameters found from cross-validation and GridSearch mentioned in the previous sections were consistent for all feature combinations. The Naive Bayes (NB) and Support Vector Machine (SVM) algorithm produced models with relatively low accuracy compared to the other algorithms. As a linear classifier, the NB algorithm was unfit for the human gait classification with natural variances. The inefficiency of the SVM classifier with the Radial Basis Function (RBF) kernel and its proneness to over-fitting given larger data sets makes it unsuitable for training this model, and its shortcomings are prevalent in a 22% average decrease in accuracy compared to the algorithms employed (Table 5.6). In addition, this

SVM algorithm is particularly sensitive to noise, which makes it unsuitable for classifying the data with human variation. Therefore, I chose a final selection of the KNN, CART, and Random forest algorithms for the phase of gait prediction.

Since joint moments are only calculated for the subset of *.mot* data processed through OpenSim, the use of regression techniques to roughly predict the moments corresponding to the joint angles from the *.c3d* files. In this scenario, the joint angles and participant information are the features, while there is a multi-class target: the moments for each of the six joints. By calculating moments for every test sample, I observed the trends of joint moments over each phase to approximate the maximum moment needed to move from one phase to the next, an addition to the overall gait pattern model.

To predict joint moments from the joint angles extracted from *.c3d* files, a model with the extra trees regressor was created using joint angles and moments from OpenSim. The features were joint angles and participant information, and the targets were joint moments. A separate model was created for each phase, as seen in Figure 5.12. The regression accuracy calculated by cross-validation for each model is recorded in Table A.6, where each model's coefficient of determination exceeds 0.5, meaning each model accounts for a majority of the variance of the outputted moments. For this application, where joint-angle trends varied greatly with each participant and even between each gait cycle, the extra trees outperformed all other regression algorithms due to the randomness in splitting nodes to smooth noise in the data set. It is important to note that due to the variance of subjects' physical characteristics (i.e., subjects can be very small to large), the regression accuracy per phase (Table A.6) may seem lower than normal. This does not affect the system's ability to take physical characteristics and derive a estimation on required moments to transition between phases of gait.

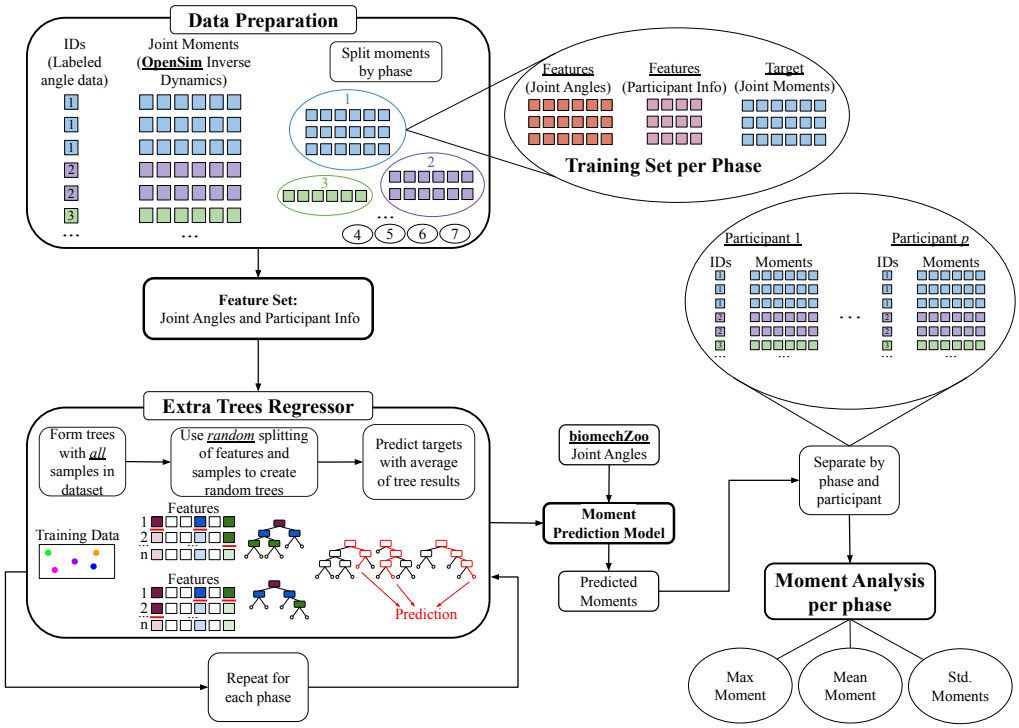


**Figure 5.12:** Pipeline for creating a moment prediction model that categorizes phases of gait and participant information to yield the max, mean, and standard deviation for moments ($Nm/kg$). The data preparation process groups all of the joint moments, angles, and participant information by phase of gait. This feature set is then split randomly to ensure that the model does not rely heavily on any individual feature, and repeated 7 times for each phase of gait.

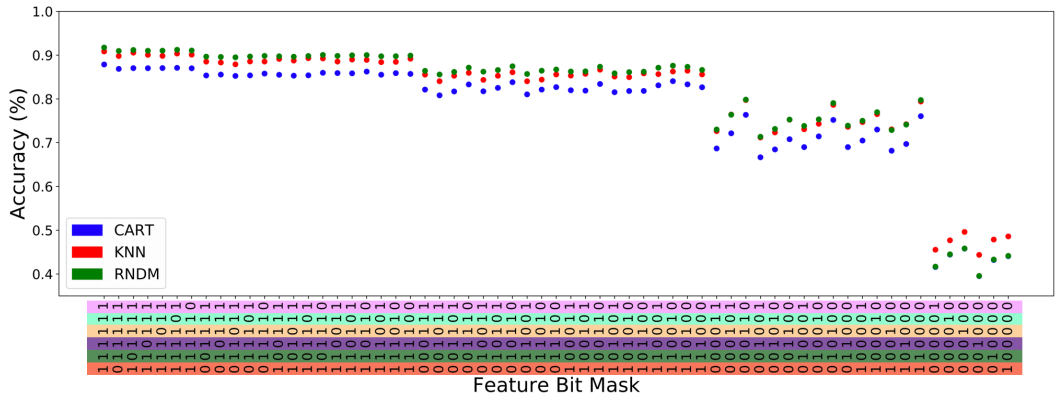


**Figure 5.13:** Relationship between accuracy yielded from predicting phase of gait from joint angles and the combination of used features: right hip (red), knee (green), ankle (purple), left hip (yellow), knee (teal), and ankle (pink). It is important to note that if there is only 1 feature there is no way a tree can be formed, so there are no decision tree outputs for those feature combinations. This method to find the optimal feature combination, or feature reduction, demonstrates there is no need to monitor all 6 joints to result in a high phase of gait predictive model. See Table 5.7 for a numeric representation.

The typical application for monitoring human gait focuses on the stance-swing transitions for cycle tracking (95% accuracy) [172], or rely heavily on the measurements on the foot (98% accuracy) [173]. This work aims to be less biased and dependent on a specific body part (in the event there is limb loss), and instead demonstrates the numerical trade-offs between tracking different joints on the human body. To increase the efficiency of the model, the number of features used was reduced while training to reduce the training run-time and ease the process of data collection [154]. The models used a maximum of $n = 10$ features to train: joint angles ($\theta_{2D} = 6$), and 4 participant attributes. Each test included the 4 participant attributes while training a model,

$$\sum_{i=1}^{\theta_{2D}} \binom{6}{i} = \sum_{i=1}^{6} \frac{6!}{(6-i)! \cdot i!} = 63$$

where the joint angle feature combinations are iterated through to find the ideal

combination of the least number of features $n$ and highest accuracy. This method trained the models ranging from just one joint angle, or all 6, meaning the model trains on a minimum of 5 features and a maximum of 10. Some joints reveal themselves to affect the correlation between features and target more than others after analyzing the accuracy of the model of each joint combination.

As previously mentioned, the feature set, or input into the model, compromises of 6 joint angles and 4 participant attributes. The target, and eventual output of the models, is the individual phase of gait for each data sample. A 10 fold cross-validation and a 20/80 train-test split across all models was used when evaluating accuracy in recognizing the collection of joint angles. The data is iterated during cross-validation to evaluate the accuracy between the labelled data set as well as for parametric configurations. To find the performance of the models against the labeled data versus predicted data, confusion matrices were used to find mean accuracy (Tables A.2, A.3 & A.4). If the models yields the correct phase of gait given the joint angle(s) compared with the labeled data set, that is considered a successful prediction. Hip joint angles are particularly effective in training the model (Figure 5.13), and models training with KNN using feature combinations with just 3 joint angles can reach over 85% accuracy with one or both hip joint features. The CART algorithm also undergoes the same feature selection process among 63 feature combinations and achieves over 84% accuracy with just 3 joint angle features, slightly underperforming the KNN algorithm. The RNDM algorithm involved the same overall feature selection in the data set as other algorithms with 63 feature combinations. Random forest outperforms both KNN and CART (Figure 5.13) and was able to reach over 87% accuracy with just 3 features, revealing the importance of randomness when analyzing human data. Refer to Figure 5.13 which shows a significant association between both

the hip joint angles and higher accuracy for all algorithms and combinations of joint angles.

### 5.4.5 Moment Predictive Model

Due to the nature of unique gait motions across individuals, this work focused on the strong connection between phase of gait, joint angles, and joints' moments. Focusing on the lower extremity joint angles for human gait is informative enough for phase classification. This approach can bridge this form of kinematic analysis toward joint dynamics. It is a well-known challenge to generalize the required moments from phase to phase for all subjects, but by taking advantage of OpenSim's inverse dynamics solver (ID):

$$\tau = M(q)\ddot{q} + C(q, \dot{q}) + G(q)$$

with the joint-angles for generalizing moments:

$$\tau = 2m\omega \times \alpha + m\omega \times (\omega \times \theta_{2D}) + G \times \theta_{2D} \tag{5.9}$$

where $\tau$ represented the generalized forces, $m$ as the mass, $\omega$ as angular velocity, $\alpha$ as angular acceleration, $G$ as gravitational forces, and $\theta_{2D}$ as the joint angles from Equation 5.5. The Moment Prediction Model (Figure 5.12) interpreted those joint angles ($\theta_{2D}$) and predicted the maximum moments ($Nm/kg$) to transition between phases of gait. This correlation between joint angles, moments, and phase of gait aim to deliver an extremely adaptable model. The output (Figure 5.14) has the potential to be applied as a bookmark or characterization for assistive technologies to replicate given the physical characteristics of their users.

Typically healthy humans follow a very similar gait pattern. However, it is important to note that there are still noticeable differences between each Subject One and Subject Two's phase of gait and joint-moment relationship (e.g., Phase 6 in Figure 5.14c). The results demonstrate that each person's gait is unique in

relying on different joints to move. Subject One, a 28 year old female that is 1.56 meters in height, and weighs 50kg. Subject Two, a 23 year old male that is 1.76 meters tall and weighs 73 kg, shows more of a minor moment requirement to transition between phases of gait than Subject One. It is essential to recognize that both subjects were chosen from different databases, yet they yielded similar trends. For example, monitoring the left knee in Figure 5.14(d) indicated that Subject Two had a larger moment to transition between Phase 3 to 4 with a 31% difference compared to Subject One (Table A.5). Yet, they followed similar moment requirements in a scaled proportion. The observation in Figure 5.14 showed that Subject One had a stronger dependency on the left side of the body, and Subject Two was more evenly distributed with a slight bias to the right side of the body. The assessment from both the gait classification and moment prediction models demonstrated a fundamental breakdown in the analysis of walking movement and can be further implemented as a valuable tool for biometric technologies.

## 5.5 Conclusion

Although optical motion capture systems are the standard solution for tracking kinematic behavior of systems in the real-world, IMUs are a far more mobile and cost effective alternative that have demonstrated promising results for analyzing multi-body dynamics. Wearable sensors rely on physical manipulation and orientation displacement in space to translate into joint-angle relationships for OpenSim motion files. In addition, IMU sensors demonstrate modularity for incorporating sensor feedback on kinematic behavior with flexible robotic systems. The results (Table 5.3 & 5.5) from the pipeline in Algorithm 2 validate the accuracy and reason for extending common acquisition techniques for quantitative movement analysis. It has been proven that simulations via OpenSim can pro-

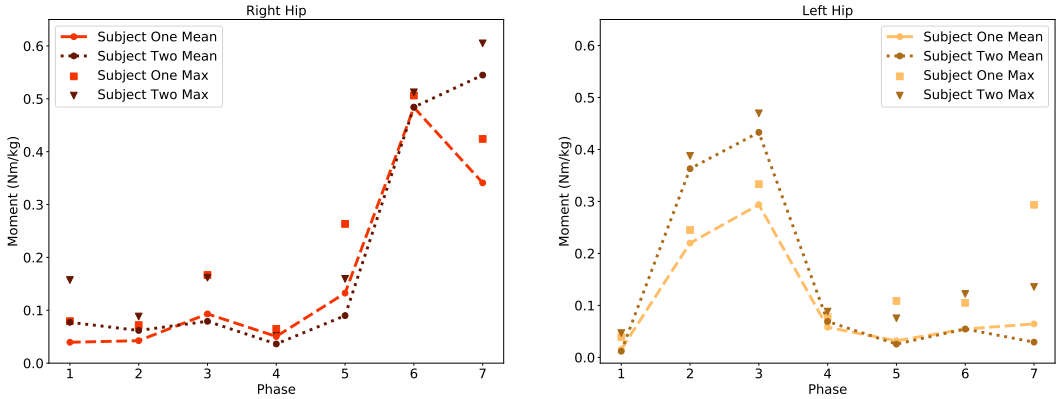


**(a)** Right hip




**(b)** Left hip

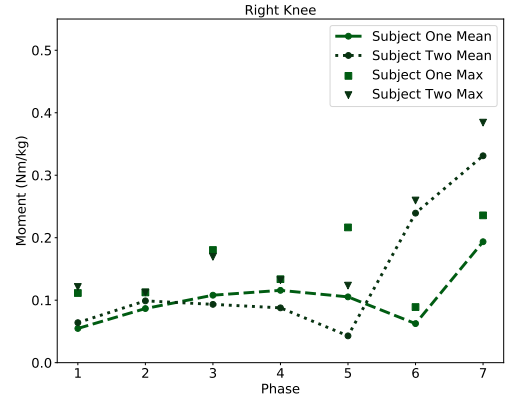


**(c)** Right knee

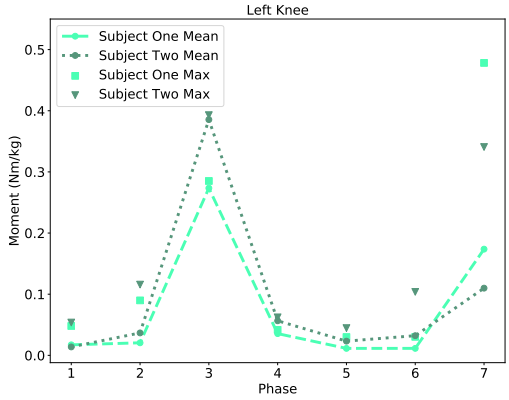


**(d)** Left knee

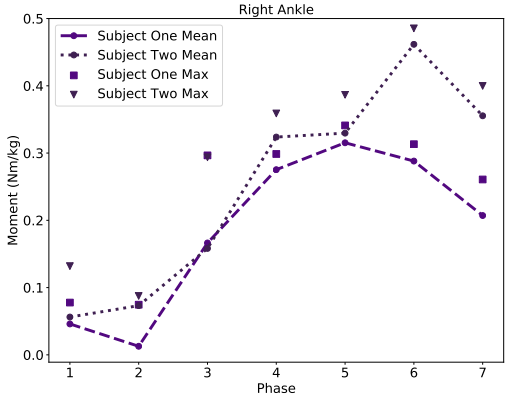


**(e)** Right ankle

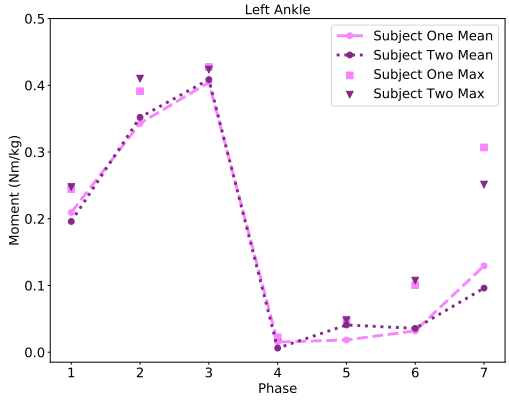


**(f)** Left ankle

**Figure 5.14:** The values as predicted by the Extra Trees Regressor (Figure 5.12) form predicted maximum moments ($Nm/kg$) for each joint. The average maximum moment required for the transition between each phase is plotted as a continuous line with the maximum for each phase based off of the subject pool. It is important to realize that every participant has a unique gait pattern, but the regressand, or outcome, yields a general approximation or trend for each phase. For numeric representations see Table A.5.

vide the forces and moments that would occur in systems with complex kinematic behavior. This low-cost mobile kinematic monitoring system demonstrates the capability for future analysis of non-room bounded activities and the ability to simulate both human and robotic applications within the same environment.

The validations from the custom IMC vs. OMC is extended using a machine learning method to identify the phase of gait from joint-angle measurements and generalize a set of required joint-moments between those phases of gait along the sagittal plane. This work used the algorithms KNN, CART, and RNDM to yield an 82%, 87%, and 92% accuracy in gait phase classification with all available features or lower extremity joints. The interpretations of how feature reduction affected the confidence of the RNDM classification model (Table 5.7) indicated how reliable monitoring fewer joint angles could be. Figure 5.13 proved this analysis by showing how the amount of joints required for monitoring each subject affects the accuracy of gait phase prediction. It is clear that the more sensors or features monitored, the higher the confidence; however, the difference between tracking 6 joints to 5 joints (0.5%), or 6 joints to 3 joints (4.04%) has a very minimal drop-off in accuracy. This finding indicates that reducing the number of joints monitored for complex gait phase-reliant applications will yield promising results. It is important to note that flexibility of joints is entirely individualized where age, or gender might demonstrate their own significant variance. This work focused on the relationship between the physical characteristics and angular displacement of joints for human subjects. The future applications of this work could include: biomechanic comparisons between age and gender, robotic assistive devices, motion not confined to the sagittal plane.s

This findings correlated the exact joint-angle measurements and phases of gait to yield each subject's moments. Figure 5.14 and Table A.5 demonstrate how

a smaller Subject One requires smaller moments to transition between phases of gait than a physically larger Subject Two. Generally, both subjects in Figure 5.14 follow similar trends, but differences like Phase 6 for the Right knee show a considerable uniqueness between persons. The difference between results demonstrated how body size affected the required maximum moments proportionally. Correlating the joint-angle relationships between the two modes for gait prediction and moment transitions (Figure 5.10) can be used as a powerful tool for biometric applications. Using the same database for two different applications bridges the IK and ID area of biomechanic analysis proving the impact of joint-angle measurement techniques. Implementing IMU sensors for biometric analysis reduces the cost, room-bounded configurations, and overall complexity of optical motion capture systems.

**Table 5.6:** Accuracy of prediction (%) of Cross-Validation (CV) on 10-fold experiments using Linear, CART, KNN, and RNDM using all available features.

| Classifier | **KNN** | **CART** | NB | SVM | **RNDM** |
|---|---|---|---|---|---|
| Mean (± SD) | 0.902 (± 0.012) | 0.857 (± 0.018) | 0.796 (± 0.017) | 0.665 (± 0.023) | 0.905 (± 0.011) |

**Table 5.7:** Using feature reduction can demonstrate the correlation between number of joints (features) and mean accuracy (%) using Random Forest classifier. It is worth noting that 6 has only 1 combination of features, but the rest follow the format: max accuracy % (mean %).

| Number of features | 6 | 5 | 4 | 3 | 2 | 1 |
|---|---|---|---|---|---|---|
| KNN | 90.8 | 90.6 (90.1) | 89.3 (88.7) | 86.7 (85.4) | 79.7 (75.0) | 49.6 (47.3) |
| CART | 87.9 | 87.1 (87.0) | 86.2 (85.6) | 84.1 (82.4) | 76.4 (71.0) | 45.8 (43.1) |
| RNDM | 91.7 | 91.2 (91.1) | 90.0 (89.8) | 87.6 (86.6) | 79.8 (75.3) | 45.8 (43.2) |

# Chapter 6

# Conclusion

## 6.1 Summary

The work in this dissertation took a holistic approach to the model and design process bridging bio-inspired robotics and user studies. It leverages the convenience of telehealth and the limitations of room-bound motion capture systems and applies this work to several areas. With flexible-rigid robotics, it modeled, simulated, monitored and controlled a series of prototypes that replicate the musculoskeletal connections by connecting the rigid (e.g., bones) and tensile elements (e.g., muscles, tendons). Designing custom simulations in an open-sourced biomechanical environment is essential to understand how the physical models would interact with or represent humans subjects.

The wireless inertial motion capture network with off-the-shelf components was created to assess the kinematic behavior of a variety of subjects. This distributed sensing network created for the prototypes was then compared and validated against commercial optical systems to demonstrate how the accuracy our system along the sagittal plane. An additional feature with this approach provided joint kinematics and dynamics creating new opportunities for those who cannot

afford expensive motion capture systems. Lastly, we generalize all of the human subject evaluations, and created an algorithm enhanced with machine learning to determine the joint-angle relationship between phases of gait. The system interpreted a complex breakdown of phases of gait (7 parts) and estimated the required moments for each joint to transition between.

## 6.2 Future Work

The pandemic put limitations on how we ran user testing. We had a small pool of our subjects to test with and heavily depended on publicly available databases for gait. As stated throughout the paper, this work has many applications in healthcare, entertainment, or sports. Our vision for other applications include:

- Deeper interpretation of how physical characteristics such as age and gender affect bio-mechanics like joint flexibility or general trends
- Many physical therapists and those going through a physical rehabilitation process could use our sensors enhanced with bio-mechanical solvers to help physical therapists monitor patients' recovery remotely or at home
- Movement recognition for certain activities (e.g., walking, running, surfing, etc.)
- With unlimited money and resources, build an assistive flexible-rigid crutch equipped with the sensors and dynamic algorithms for different users

### Model Optimization

As the prototypes increase in complexity, the work in this thesis established a methodology of creating hybrid-based (combination of hard and soft elements)

robotics. Figure 6.1 shows an iterative design approach that uses a Monte Carlo process to "test" different model sizes (e.g., weight, length or rods, etc.) to find the optimal conditions to operate the model. Models with specific femur and tibia length could be analyzed using the methodology proposed here. The process could be automated, so the all of the possible geometries are tested separately. The "desired kinematics" is dictated by the user's gait. For each configuration the dynamics behavior and the gate can be predicted so only the optimal assembly is considered for testing.

Future applications of this process may include:

- Automate the process of model generation.
- Find optimal size conditions (e.g., weight, length, etc.) of existing models and provide feedback on controls or design changes

**Longevity Experiment**

As previously mentioned in Chapter 4.4.2, the custom motion sensors used 9-axis IMUs equipped with the Madgwick sensor fusion algorithm to provide tracking data by measuring velocity, orientation, gravitational forces [174]. Typically, they tend to drift over long periods of time just like Figure 6.2(b), but when using the Madgwick filter [140] the drift is significantly reduced especially for short trials like in this work. A simplification of the Madgwick filter [140] can be broken down into these steps:

1. Obtain sensor measurements
2. Gather an orientation computed from accelerometer data (gradient step)
3. Orientation calibrated from the gyro (numerical integration)

4. Fuse measurements to estimate attitude

5. Compared previous with current time data

This work proposed a novel calibration process for each sensor (explained in Chapter 4.4.2) by generating a point of origin in a static position. Before capturing an experiment with motion, each individual started with a static trial with both the OMC and IMC (Figure 3.10). Additional tests were conducted with the same system to measure a drift on both a flat and tilted surface for day long experiments (Figure 6.3). Due to the Madgwick sensor fusion filter imposing comparisons between time points, if there exists no change in motion (i.e., a sensor flat on the table not moving), the algorithm assumes no change and therefore no drift. If there exists motion, there is a significant drift in the Frontal and Traversal planes as seen in Figure 6.2. It is clear that there exists a correlation between time and angles when the sensors are moving for a longer duration (Table A.8). As a future extension of this work, it would be interesting to monitor the effect of a longitudinal tuning algorithm (potentially including a Kalman filter) to track the movement of limb joints precisely, and result in a drift-free measurement all completely independent from OMC systems [174].

To summarize some of the existing limitations of this work, I mentioned solving the drift in all planes (Figure 6.2 and Table A.8), as well as increasing the power capacity for longitudinal studies (i.e., hour long recording sessions instead of minute long trials). This can be achieved by either purchasing expensive sensors, or developing additional algorithms to detect, compensate, and use less power demanding wireless communication protocols. Longer recording sessions with this system could provide:

- Fatigue in patients during longer therapy sessions

- Better physical assessments, such as strength, over months of rehabilitation
- Teletherapy sessions that mitigate commute times and other physical and financial obstacles

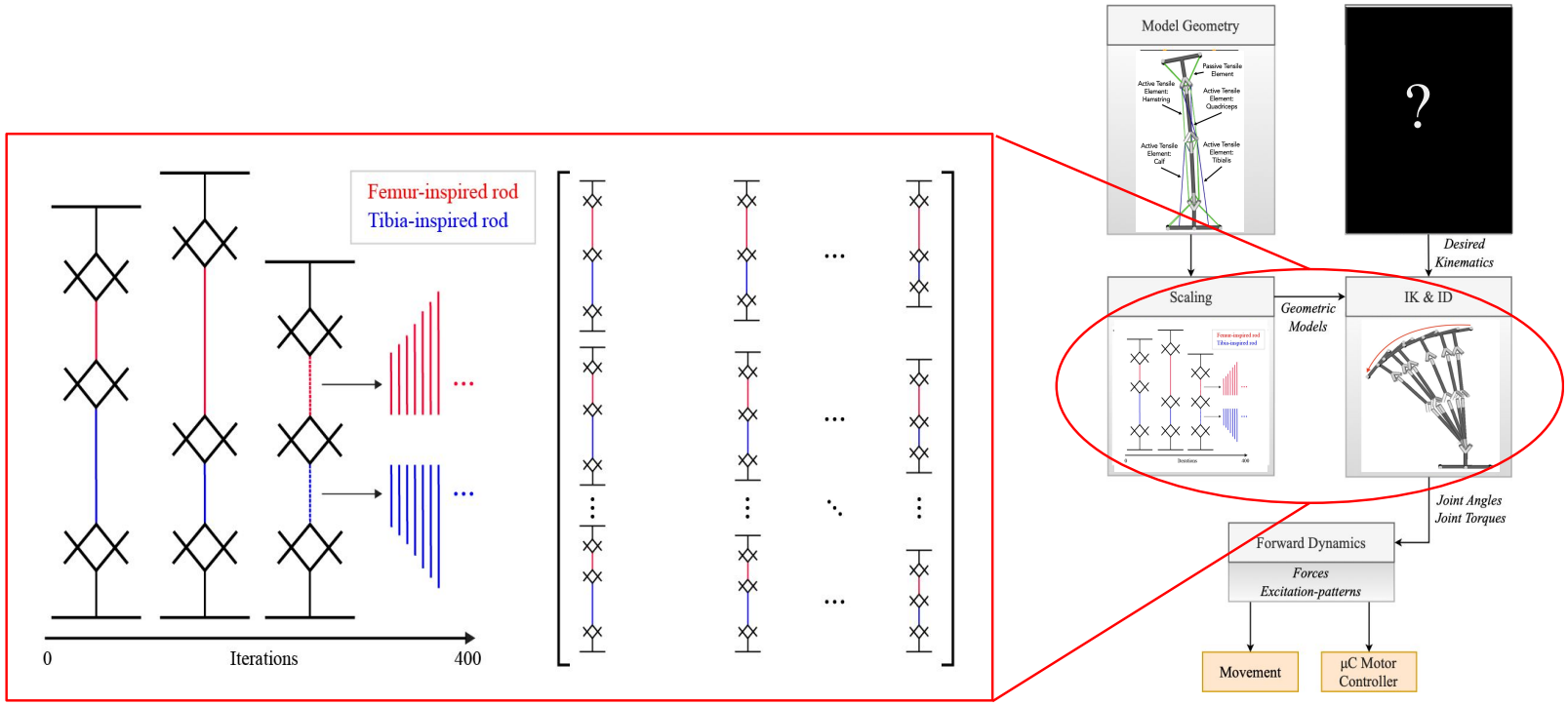


**Figure 6.1:** To optimize the design process of each model, we iteratively sweep across different sizes and weight parameters to evaluate optimal operating conditions to complete desired motions. This scaling process is an addition to how we test each geometric model in Figure 3.2.

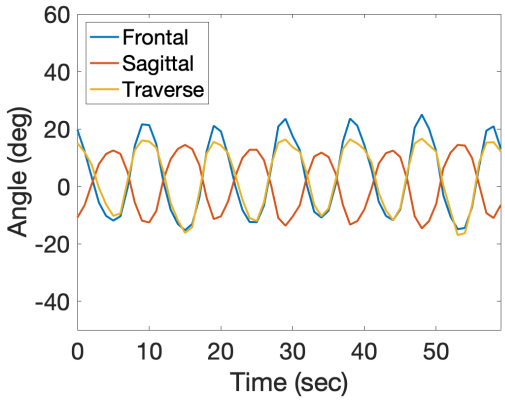


**(a)** 1 minute

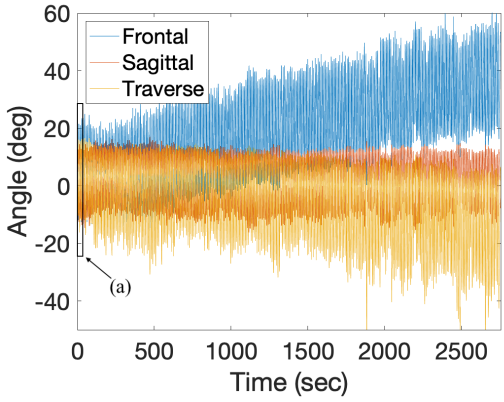


**(b)** 45 minutes

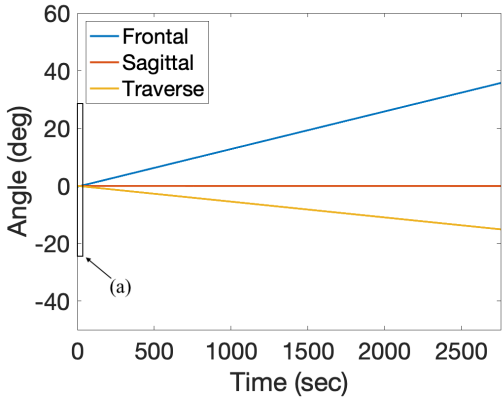


**(c)** Linear fit

**Figure 6.2:** The drift from the custom sensors during a 45 minute recording sessions demonstrates how significant the drift in the frontal and traversal planes. All experiments in this work was done in short sessions (1 minute trials like (a)) along the Saggital plane, meaning there was low drift of $-6.93 \cdot 10^{-4}$ (deg/sec) according to Table A.8). For longitudinal studies (b) & (c) shows a significant drift in the traversal and frontal planes, whereas the Saggital plane remains consistent.

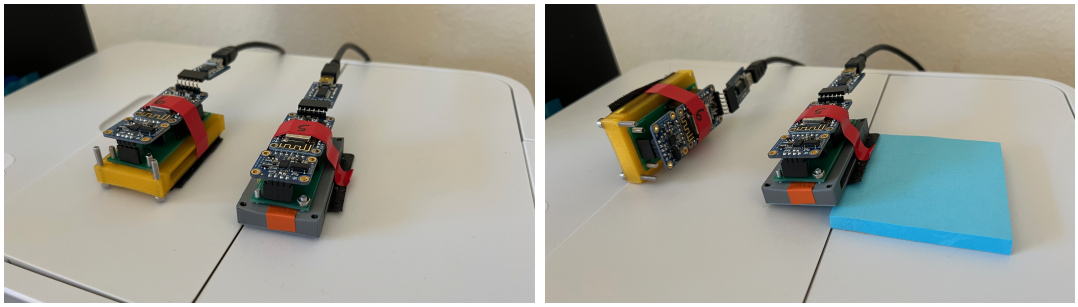

**(a)** **(b)**

**Figure 6.3:** Demo of the static longevity experiment in the flat orientation (a) and tilted orientation (b).

# Appendix A

# Appendix

**Table A.1:** Using GridSearchCV with the scikit learn tools, the best parameters were found for KNN, CART and RNDM where each algorithm went through a 10 fold and split using cross-validation.

| **KNN** | | **CART** | | **RNDM** | |
|---|---|---|---|---|---|
| algorithm | auto | ccp alpha | 0.0 | bootstrap | True |
| leaf size | 30 | class weight | None | ccp alpha | 0.0 |
| metric | minkowski | criterion | gini | class weight | None |
| metric params | None | max depth | None | criterion | gini |
| n jobs | None | max features | None | max depth | None |
| n neighbors | 10 | max leaf nodes | None | max features | sqrt |
| p | 2 | min impurity decrease | 0.0 | max leaf nodes | None |
| weights | distance | min impurity split | 1 | max samples | None |
| | | min samples split | 5 | min impurity decrease | 0.0 |
| | | min weight fraction leaf | 0.0 | min impurity split | None |
| | | presort | deprecated | min samples leaf | 1 |
| | | random state | None | min samples split | 5 |
| | | splitter | best | min weight fraction leaf | 0.0 |
| | | | | n estimators | 250 |
| | | | | n jobs | None |
| | | | | oob score | False |
| | | | | random state | None |
| | | | | verbose | 0 |
| | | | | warm start | False |

**Table A.2:** K-Nearest Neighbors Classification report with a confusion matrix for all the phases of gait (left) and scores (right).

| | **1** | **2** | **3** | **4** | **5** | **6** | **7** |
|---|---|---|---|---|---|---|---|
| **1** | **18,885** | 1140 | 19 | 7 | 54 | 18 | 1149 |
| **2** | 1145 | **17,179** | 864 | 10 | 33 | 47 | 8 |
| **3** | 25 | 928 | **14,827** | 807 | 28 | 100 | 37 |
| **4** | 13 | 7 | 814 | **10,169** | 778 | 37 | 51 |
| **5** | 29 | 28 | 20 | 765 | **22,132** | 824 | 32 |
| **6** | 9 | 27 | 55 | 18 | 889 | **28,913** | 1183 |
| **7** | 1194 | 5 | 20 | 28 | 26 | 1200 | **14,700** |

| | **Precision** | **Recall** | **F1-Score** | **Support** |
|---|---|---|---|---|
| **7** | 0.89 | 0.89 | 0.89 | 21,272 |
| **6** | 0.89 | 0.89 | 0.89 | 19,286 |
| **5** | 0.89 | 0.89 | 0.89 | 16,746 |
| **4** | 0.86 | 0.86 | 0.86 | 11,869 |
| **3** | 0.92 | 0.93 | 0.93 | 23,830 |
| **2** | 0.93 | 0.93 | 0.93 | 31,094 |
| **1** | 0.86 | 0.86 | 0.86 | 17,173 |
| **accuracy** | | | 0.90 | 141,270 |
| **macro avg** | 0.89 | 0.89 | 0.89 | 141,270 |
| **weighted avg** | 0.90 | 0.90 | 0.90 | 141,270 |

**Table A.3:** Classification And Regression Trees Classification report with a confusion matrix for all the phases of gait (left) and scores (right).

| | **1** | **2** | **3** | **4** | **5** | **6** | **7** |
|---|---|---|---|---|---|---|---|
| **1** | **17,894** | 1404 | 51 | 22 | 67 | 27 | 1807 |
| **2** | 1321 | **16,452** | 1366 | 25 | 49 | 55 | 18 |
| **3** | 38 | 1411 | **14,037** | 1041 | 57 | 118 | 44 |
| **4** | 26 | 23 | 1099 | **9334** | 1264 | 61 | 62 |
| **5** | 50 | 35 | 72 | 1229 | **21,234** | 1171 | 39 |
| **6** | 32 | 64 | 94 | 64 | 1267 | **27,874** | 1699 |
| **7** | 1847 | 13 | 54 | 70 | 43 | 1735 | **13,411** |

| | **Precision** | **Recall** | **F1-Score** | **Support** |
|---|---|---|---|---|
| **7** | 0.84 | 0.84 | 0.84 | 21,272 |
| **6** | 0.85 | 0.85 | 0.85 | 19286 |
| **5** | 0.84 | 0.84 | 0.84 | 16,746 |
| **4** | 0.79 | 0.79 | 0.79 | 11,869 |
| **3** | 0.89 | 0.89 | 0.89 | 23,830 |
| **2** | 0.90 | 0.90 | 0.90 | 31,094 |
| **1** | 0.79 | 0.78 | 0.78 | 17,173 |
| **accuracy** | | | 0.85 | 141,270 |
| **macro avg** | 0.84 | 0.84 | 0.84 | 141,270 |
| **weighted avg** | 0.85 | 0.85 | 0.85 | 141,270 |

**Table A.4:** Random Forest Classification report with a confusion matrix for all the phases of gait (left) and scores (right).

| | **1** | **2** | **3** | **4** | **5** | **6** | **7** |
|---|---|---|---|---|---|---|---|
| **1** | **19,106** | 855 | 18 | 8 | 46 | 10 | 1229 |
| **2** | 974 | **17,381** | 850 | 4 | 31 | 40 | 6 |
| **3** | 33 | 990 | **14,833** | 737 | 24 | 98 | 31 |
| **4** | 13 | 9 | 823 | **10,118** | 839 | 31 | 36 |
| **5** | 32 | 22 | 22 | 785 | **22,207** | 741 | 21 |
| **6** | 15 | 28 | 39 | 16 | 881 | **29,053** | 1062 |
| **7** | 1228 | 5 | 19 | 26 | 22 | 1304 | **14,569** |

| | **Precision** | **Recall** | **F1-Score** | **Support** |
|---|---|---|---|---|
| **7** | 0.89 | 0.90 | 0.90 | 21,272 |
| **6** | 0.90 | 0.90 | 0.90 | 19,286 |
| **5** | 0.89 | 0.89 | 0.89 | 16,746 |
| **4** | 0.87 | 0.85 | 0.86 | 11,869 |
| **3** | 0.92 | 0.93 | 0.93 | 23,830 |
| **2** | 0.93 | 0.93 | 0.93 | 31,094 |
| **1** | 0.86 | 0.85 | 0.85 | 17,173 |
| **accuracy** | | | 0.90 | 141,270 |
| **macro avg** | 0.89 | 0.89 | 0.89 | 141,270 |
| **weighted avg** | 0.90 | 0.90 | 0.90 | 141,270 |

**Table A.5:** Required moment transitions between gait cycles as predicted by Random Forest regression for Subject One, Subject Two, and All Partipicants. See Figure 5.7 for physical characteristics (e.g., mass, height, weight).

| **Subject One** | Moment ($Nm/kg$) | | | | | |
|---|---|---|---|---|---|---|
| Gait Transition | Right Hip | Left Hip | Right Knee | Left Knee | Right Ankle | Left Ankle |
| $1 \longrightarrow 2$ | 0.080 ($\pm$ 0.014) | 0.040 ($\pm$ 0.011) | 0.110 ($\pm$ 0.013) | 0.048 ($\pm$ 0.015) | 0.777 ($\pm$ 0.013) | 0.244 ($\pm$ 0.021) |
| $2 \longrightarrow 3$ | 0.072 ($\pm$ 0.018) | 0.245 ($\pm$ 0.025) | 0.112 ($\pm$ 0.020) | 0.090 ($\pm$ 0.018) | 0.075 ($\pm$ 0.013) | 0.391 ($\pm$ 0.021) |
| $3 \longrightarrow 4$ | 0.167 ($\pm$ 0.036) | 0.333 ($\pm$ 0.033) | 0.180 ($\pm$ 0.029) | 0.285 ($\pm$ 0.030) | 0.297 ($\pm$ 0.017) | 0.427 ($\pm$ 0.029) |
| $4 \longrightarrow 5$ | 0.065 ($\pm$ 0.010) | 0.078 ($\pm$ 0.015) | 0.134 ($\pm$ 0.024) | 0.042 ($\pm$ 0.006) | 0.299 ($\pm$ 0.011) | 0.022 ($\pm$ 0.005) |
| $5 \longrightarrow 6$ | 0.263 ($\pm$ 0.032) | 0.109 ($\pm$ 0.021) | 0.216 ($\pm$ 0.054) | 0.030 ($\pm$ 0.004) | 0.341 ($\pm$ 0.016) | 0.049 ($\pm$ 0.015) |
| $6 \longrightarrow 7$ | 0.506 ($\pm$ 0.002) | 0.105 ($\pm$ 0.004) | 0.089 ($\pm$ 0.006) | 0.030 ($\pm$ 0.006) | 0.313 ($\pm$ 0.008) | 0.100 ($\pm$ 0.004) |
| $7 \longrightarrow 1$ | 0.424 ($\pm$ 0.086) | 0.294 ($\pm$ 0.074) | 0.236 ($\pm$ 0.060) | 0.478 ($\pm$ 0.118) | 0.261 ($\pm$ 0.074) | 0.307 ($\pm$ 0.060) |
| **Subject Two** | Moment ($Nm/kg$) | | | | | |
| Gait Transition | Right Hip | Left Hip | Right Knee | Left Knee | Right Ankle | Left Ankle |
| $1 \longrightarrow 2$ | 0.157 ($\pm$ 0.002) | 0.047 ($\pm$ 0.010) | 0.121 ($\pm$ 0.015) | 0.054 ($\pm$ 0.011) | 0.132 ($\pm$ 0.020) | 0.247 ($\pm$ 0.018) |
| $2 \longrightarrow 3$ | 0.088 ($\pm$ 0.019) | 0.388 ($\pm$ 0.020) | 0.122 ($\pm$ 0.018) | 0.116 ($\pm$ 0.016) | 0.088 ($\pm$ 0.020) | 0.410 ($\pm$ 0.0160) |
| $3 \longrightarrow 4$ | 0.162 ($\pm$ 0.022) | 0.470 ($\pm$ 0.033) | 0.169 ($\pm$ 0.020) | 0.393 ($\pm$ 0.013) | 0.294 ($\pm$ 0.009) | 0.424 ($\pm$ 0.010) |
| $4 \longrightarrow 5$ | 0.051 ($\pm$ 0.008) | 0.088 ($\pm$ 0.010) | 0.132 ($\pm$ 0.020) | 0.062 ($\pm$ 0.004) | 0.359 ($\pm$ 0.015) | 0.013 ($\pm$ 0.0027) |
| $5 \longrightarrow 6$ | 0.159 ($\pm$ 0.009) | 0.075 ($\pm$ 0.015) | 0.123 ($\pm$ 0.011) | 0.045 ($\pm$ 0.007) | 0.387 ($\pm$ 0.017) | 0.048 ($\pm$ 0.004) |
| $6 \longrightarrow 7$ | 0.512 ($\pm$ 0.004) | 0.122 ($\pm$ 0.006) | 0.260 ($\pm$ 0.002) | 0.104 ($\pm$ 0.005) | 0.485 ($\pm$ 0.009) | 0.107 ($\pm$ 0.007) |
| $7 \longrightarrow 1$ | 0.605 ($\pm$ 0.038) | 0.135 ($\pm$ 0.017) | 0.384 ($\pm$ 0.017) | 0.341 ($\pm$ 0.033) | 0.340 ($\pm$ 0.025) | 0.251 ($\pm$ 0.022) |
| **All Participants** | Moment ($Nm/kg$) | | | | | |
| Gait Transition | Right Hip | Left Hip | Right Knee | Left Knee | Right Ankle | Left Ankle |
| $1 \longrightarrow 2$ | 0.109 ($\pm$ 0.062) | 0.102 ($\pm$ 0.072) | 0.127 ($\pm$ 0.039) | 0.118 ($\pm$ 0.080) | 0.109 ($\pm$ 0.062) | 0.295 ($\pm$ 0.097) |
| $2 \longrightarrow 3$ | 0.104 ($\pm$ 0.065) | 0.270 ($\pm$ 0.117) | 0.122 ($\pm$ 0.063) | 0.116 ($\pm$ 0.050) | 0.104 ($\pm$ 0.064) | 0.387 ($\pm$ 0.052) |
| $3 \longrightarrow 4$ | 0.130 ($\pm$ 0.030) | 0.435 ($\pm$ 0.239) | 0.189 ($\pm$ 0.056) | 0.331 ($\pm$ 0.130) | 0.131 ($\pm$ 0.031) | 0.354 ($\pm$ 0.152) |
| $4 \longrightarrow 5$ | 0.083 ($\pm$ 0.028) | 0.111 ($\pm$ 0.063) | 0.146 ($\pm$ 0.021) | 0.080 ($\pm$ 0.036) | 0.086 ($\pm$ 0.041) | 0.055 ($\pm$ 0.039) |
| $5 \longrightarrow 6$ | 0.194 ($\pm$ 0.104) | 0.116 ($\pm$ 0.096) | 0.181 ($\pm$ 0.057) | 0.056 ($\pm$ 0.042) | 0.197 ($\pm$ 0.107) | 0.053 ($\pm$ 0.025) |
| $6 \longrightarrow 7$ | 0.425 ($\pm$ 0.232) | 0.089 ($\pm$ 0.035) | 0.212 ($\pm$ 0.124) | 0.066 ($\pm$ 0.045) | 0.426 ($\pm$ 0.231) | 0.064 ($\pm$ 0.035) |
| $7 \longrightarrow 1$ | 0.0.439 ($\pm$ 0.207) | 0.161 ($\pm$ 0.128) | 0.264 ($\pm$ 0.099) | 0.283 ($\pm$ 0.177) | 0.438 ($\pm$ 0.206) | 0.254 ($\pm$ 0.138) |

**Table A.6:** A table of the regression accuracy per phase when generating the Extra Trees model to predict joint moments from joint angles. The accuracy is the coefficient of determination, $R^2$, of the prediction. The best possible score is 1.0.

| Phase of Gait | Regression Accuracy ($R^2$ error) |
|---|---|
| 1 | 0.567 |
| 2 | 0.592 |
| 3 | 0.713 |
| 4 | 0.840 |
| 5 | 0.568 |
| 6 | 0.727 |
| 7 | 0.505 |

**Table A.7:** Participant Information used in Figure 5.7.

| | **Height** | **Age** | **Weight** |
|---|---|---|---|
| Male | 1.66 | 31 | 67 |
| Female | 1.64 | 48 | 65.4 |
| Female | 1.56 | 28 | 50 |
| Male | 1.77 | 23 | 72.5 |
| Male | 1.83 | 25 | 73.5 |
| Male | 1.76 | 23 | 73 |
| Female | 1.69 | 44 | 65 |
| Female | 1.66 | 30 | 57.1 |
| Male | 1.88 | 57 | 86 |
| Male | 1.8 | 59 | 63.4 |
| Female | 1.7 | 26 | 61.3 |
| Male | 1.8 | 29 | 92 |
| Female | 1.58 | 22 | 67 |
| Female | 1.76 | 26 | 73.8 |
| Female | 1.71 | 48 | 59.8 |
| Male | 1.92 | 33 | 87.5 |
| Female | 1.66 | 31 | 80.5 |
| Male | 1.89 | 38 | 89.9 |
| Female | 1.7 | 62 | 60.7 |
| Male | 1.77 | 21 | 67.2 |
| Female | 1.6 | 24 | 63.5 |
| Male | 1.84 | 21 | 89.6 |
| Female | 1.55 | 19 | 56.5 |
| Female | 1.65 | 40 | 61.8 |
| Female | 1.64 | 40 | 61.5 |
| Male | 1.74 | 32 | 72.2 |
| Female | 1.64 | 28 | 61.9 |
| Male | 1.91 | 25 | 88 |
| Male | 1.82 | 25 | 79.5 |
| Female | 1.72 | 21 | 62.8 |
| Male | 1.74 | 39 | 74 |
| Male | 1.77 | 52 | 87.2 |
| Female | 1.7 | 35 | 62 |
| Male | 1.9 | 48 | 89.4 |
| Female | 1.66 | 63 | 60.2 |

**Table A.7:** *Cont.*

| | Height | Age | Weight |
|---|---|---|---|
| Female | 1.69 | 58 | 73 |
| Female | 1.73 | 50 | 68 |
| Female | 1.69 | 46 | 76 |
| Female | 1.67 | 41 | 60.5 |
| Male | 1.79 | 43 | 95 |
| Female | 1.69 | 30 | 58 |
| Female | 1.71 | 64 | 51.5 |
| Male | 1.72 | 51 | 65.5 |
| Male | 1.87 | 24 | 86 |
| Male | 1.72 | 26 | 50.8 |
| Male | 1.77 | 38 | 81.5 |
| Male | 1.76 | 42 | 66.1 |
| Male | 1.88 | 31 | 74.8 |
| Male | 1.83 | 67 | 98 |
| Male | 1.78 | 21 | 74 |
| Male | 1.75 | 29 | 68.9 |
| Female | 1.81 | 21 | 64.9 |
| Male | 1.84 | 21 | 80.8 |
| Male | 1.82 | 23 | 82.7 |
| Female | 1.63 | 26 | 54.9 |
| Male | 1.79 | 21 | 77.3 |
| Male | 1.91 | 24 | 94.2 |
| Male | 1.88 | 23 | 69.5 |
| Male | 1.84 | 26 | 72 |
| Female | 1.58 | 20 | 52.3 |
| Female | 1.68 | 25 | 60.4 |
| Female | 1.64 | 23 | 55 |
| Female | 1.69 | 21 | 69.7 |
| Female | 1.69 | 26 | 59.3 |
| Female | 1.67 | 25 | 54.5 |
| Female | 1.75 | 23 | 57.4 |
| Female | 1.6 | 27 | 47.3 |
| Female | 1.62 | 22 | 61.4 |
| Male | 1.81 | 21 | 82.3 |
| Female | 1.69 | 19 | 65.6 |
| Female | 1.55 | 22 | 56.7 |
| Female | 1.61 | 26 | 56 |
| Male | 1.82 | 21 | 69.1 |
| Female | 1.62 | 22 | 62.1 |
| Male | 1.74 | 30 | 80.7 |
| Male | 1.99 | 21 | 91.2 |
| Male | 1.78 | 21 | 69.5 |

**Table A.7:** *Cont.*

| | Height | Age | Weight |
|---|---|---|---|
| Male | 1.83 | 24 | 67.5 |
| Female | 1.81 | 22 | 62.1 |
| Male | 1.81 | 28 | 81.35 |
| Female | 1.65 | 21 | 58.1 |
| Male | 1.78 | 23 | 80.9 |
| Female | 1.68 | 27 | 67.6 |
| Male | 1.78 | 23 | 82 |
| Female | 1.67 | 21 | 58.8 |
| Female | 1.69 | 24 | 59 |
| Female | 1.72 | 23 | 56.1 |
| Female | 1.61 | 23 | 52.1 |
| Male | 1.79 | 30 | 71 |
| Female | 1.58 | 21 | 53.15 |
| Female | 1.75 | 21 | 65.15 |
| Male | 1.83 | 25 | 79.95 |
| Female | 1.64 | 23 | 54.8 |
| Male | 1.82 | 21 | 76.5 |
| Male | 1.82 | 22 | 74.6 |
| Female | 1.65 | 20 | 56.45 |
| Male | 1.88 | 22 | 78.3 |
| Male | 1.92 | 22 | 90.8 |
| Male | 1.86 | 24 | 72.2 |
| Male | 1.87 | 22 | 81.8 |
| Female | 1.67 | 21 | 61.8 |
| Female | 1.61 | 30 | 55.75 |
| Male | 1.71 | 20 | 69.75 |
| Female | 1.7 | 22 | 66.15 |
| Male | 1.86 | 23 | 73.35 |
| Male | 1.79 | 22 | 71.75 |
| Male | 1.85 | 19 | 77.75 |
| Male | 1.778 | 24 | 69.85 |
| Male | 1.83 | 21 | 68.04 |

**Table A.8:** Longitudinal studies with the custom sensors result in a significant drift in the frontal and traversal planes. This table shows the slope of the drift (deg/sec) during a 45 minutes session recording the base of the foot on an exercise bike (Figure 6.2)

| Plane | Slope (deg/sec) |
|---|---|
| **Frontal** | 0.0102 |
| **Saggital** | $-6.93 \cdot 10^{-4}$ |
| **Traverse** | -0.0073 |

# Bibliography


[1] Y. Nubar and R. Contini, "A minimal principle in biomechanics," *The bulletin of mathematical biophysics*, vol. 23, no. 4, pp. 377–391, 1961.

[2] A. Cappozzo, U. Della Croce, A. Leardini, and L. Chiari, "Human movement analysis using stereophotogrammetry: Part 1: theoretical background," *Gait & posture*, vol. 21, no. 2, pp. 186–196, 2005.

[3] A. B. Zoss, H. Kazerooni, and A. Chu, "Biomechanical design of the berkeley lower extremity exoskeleton (bleex)," *IEEE/ASME Transactions On Mechatronics*, vol. 11, no. 2, pp. 128–138, 2006.

[4] G. Zeilig, H. Weingarden, M. Zwecker, I. Dudkiewicz, A. Bloch, and A. Esquenazi, "Safety and tolerance of the rewalk™ exoskeleton suit for ambulation by people with complete spinal cord injury: a pilot study," *The journal of spinal cord medicine*, vol. 35, no. 2, pp. 96–101, 2012.

[5] M. Wehner, B. Quinlivan, P. M. Aubin, E. Martinez-Villalpando, M. Baumann, L. Stirling, K. Holt, R. Wood, and C. Walsh, "A lightweight soft exosuit for gait assistance," in *Robotics and Automation (ICRA), 2013 IEEE International Conference on*, pp. 3362–3369, IEEE, 2013.

[6] E. J. Rouse, L. M. Mooney, and H. M. Herr, "Clutchable series-elastic actuator: Implications for prosthetic knee design," *The International Journal of Robotics Research*, vol. 33, no. 13, pp. 1611–1625, 2014.

[7] E. S. van Hal, J. M. Hijmans, K. Postema, and E. Otten, "A prosthetic leg prototype for improved mediolateral balance control: Design of a case–control study," *Cogent Engineering*, vol. 5, no. 1, pp. 1–12, 2018.

[8] E. Rogers, P. Polygerinos, S. Allen, F. A. Panizzolo, C. J. Walsh, and D. P. Holland, "A quasi-passive knee exoskeleton to assist during descent," in *Wearable Robotics: Challenges and Trends*, pp. 63–67, Springer, 2017.

[9] K. Nishimura, M. Bugajska, J. Vaz, P. Oh, D. Sofge, and D. M. Lofaro, "On humanoid co-robot locomotion when mechanically coupled to a human

partner," in *2018 15th International Conference on Ubiquitous Robots (UR)*, pp. 412–419, IEEE, 2018.

[10] M. T. Tolley, R. F. Shepherd, B. Mosadegh, K. C. Galloway, M. Wehner, M. Karpelson, R. J. Wood, and G. M. Whitesides, "A resilient, untethered soft robot," *Soft robotics*, vol. 1, no. 3, pp. 213–223, 2014.

[11] M. Wehner, R. L. Truby, D. J. Fitzgerald, B. Mosadegh, G. M. Whitesides, J. A. Lewis, and R. J. Wood, "An integrated design and fabrication strategy for entirely soft, autonomous robots," *Nature*, vol. 536, no. 7617, pp. 451–455, 2016.

[12] D. Hustig-Schultz, V. SunSpiral, and M. Teodorescu, "Morphological design for controlled tensegrity quadruped locomotion," in *Intelligent Robots and Systems (IROS), 2016 IEEE/RSJ International Conference on*, pp. 4714–4719, IEEE, 2016.

[13] F. Carreño and M. A. Post, "Design of a novel wheeled tensegrity robot: a comparison of tensegrity concepts and a prototype for travelling air ducts," *Robotics and Biomimetics*, vol. 5, no. 1, p. 1, 2018.

[14] J. Bruce, A. Sabelhaus, Y. Chen, D. Lu, K. Morse, S. Milam, K. Caluwaerts, A. M. Agogino, and V. SunSpiral, "Superball: Exploring tensegrities for planetary probes," in *12th International Symposium on Artificial Intelligence, Robotics and Automation in Space (i-SAIRAS)*, 2014.

[15] A. P. Sabelhaus, L. J. van Vuuren, A. Joshi, E. Zhu, H. J. Garnier, K. A. Sover, J. Navarro, A. K. Agogino, and A. M. Agogino, "Design, simulation, and testing of laika, a quadruped robot with a flexible actuated spine," *arXiv preprint arXiv:1804.06527*, 2018.

[16] J. Friesen, A. Pogue, T. Bewley, M. de Oliveira, R. Skelton, and V. Sunspiral, "Ductt: a tensegrity robot for exploring duct systems," in *Robotics and Automation (ICRA), 2014 IEEE International Conference on*, pp. 4222–4228, IEEE, 2014.

[17] S. Lessard, J. Bruce, E. Jung, M. Teodorescu, V. SunSpiral, and A. Agogino, "A lightweight, multi-axis compliant tensegrity joint," in *Robotics and Automation (ICRA), 2016 IEEE International Conference on*, pp. 630–635, IEEE, 2016.

[18] L. B. Baltaxe-Admony, A. S. Robbins, E. A. Jung, S. Lessard, M. Teodorescu, V. SunSpiral, and A. Agogino, "Simulating the human shoulder through active tensegrity structures," in *ASME 2016 International Design*

*Engineering Technical Conferences and Computers and Information in Engineering Conference*, pp. V006T09A027–V006T09A027, American Society of Mechanical Engineers, 2016.

[19] E. Jung, V. Ly, D. Castro, and M. Teodorescu, "Knee-inspired tensegrity flexural joint," *Ubiquitous Robotics (UR), Korean Robotics Society (KROS)*, 2018.

[20] E. Jung, V. Ly, N. Cessna, L. Ngo, D. Castro, V. SunSpiral, and M. Teodorescu, "Bio-inspired tensegrity flexural joints," *Robotics and Automation (ICRA), IEEE International Conference*, 2018.

[21] C. Schreiber and F. Moissenet, "A multimodal dataset of human gait at different walking speeds established on injury-free adult participants," *Scientific data*, vol. 6, no. 1, pp. 1–7, 2019.

[22] F. Horst, S. Lapuschkin, W. Samek, K. Müller, and W. Schöllhorn, "A public dataset of overground walking kinetics and full-body kinematics in healthy individuals," *Mendeley Data v1*, 2018.

[23] S. L. Delp, F. C. Anderson, A. S. Arnold, P. Loan, A. Habib, C. T. John, E. Guendelman, and D. G. Thelen, "Opensim: open-source software to create and analyze dynamic simulations of movement," *IEEE transactions on biomedical engineering*, vol. 54, no. 11, pp. 1940–1950, 2007.

[24] A. Seth, M. Sherman, J. A. Reinbolt, and S. L. Delp, "Opensim: a musculoskeletal modeling and simulation framework for in silico investigations and exchange," *Procedia Iutam*, vol. 2, pp. 212–232, 2011.

[25] S. Kim, J. Bosque, J. P. Meehan, A. Jamali, and R. Marder, "Increase in outpatient knee arthroscopy in the united states: a comparison of national surveys of ambulatory surgery, 1996 and 2006," *JBJS*, vol. 93, no. 11, pp. 994–1000, 2011.

[26] K. Ziegler-Graham, E. J. MacKenzie, P. L. Ephraim, T. G. Travison, and R. Brookmeyer, "Estimating the prevalence of limb loss in the united states: 2005 to 2050," *Archives of physical medicine and rehabilitation*, vol. 89, no. 3, pp. 422–429, 2008.

[27] L. Nashner, "Adapting reflexes controlling the human posture," *Experimental brain research*, vol. 26, no. 1, pp. 59–72, 1976.

[28] M. B. Wiggin, G. S. Sawicki, and S. H. Collins, "An exoskeleton using controlled energy storage and release to aid ankle propulsion," in *Rehabilitation Robotics (ICORR), 2011 IEEE International Conference on*, pp. 1–5, IEEE, 2011.

[29] H. Springer Berlin Heidelberg, Martin, and et al, "Musculoskeletal robots and wearable devices on the basis of cable-driven actuators, soft robotics," *pg. 42-53*, 2015.

[30] R. E. Skelton and M. C. de Oliveira, *Tensegrity systems*. Springer, 2009.

[31] L.-H. Chen, K. Kim, E. Tang, K. Li, R. House, E. L. Zhu, K. Fountain, A. M. Agogino, A. Agogino, V. Sunspiral, *et al.*, "Soft spherical tensegrity robot design using rod-centered actuation and control," *Journal of Mechanisms and Robotics*, vol. 9, no. 2, p. 025001, 2017.

[32] J. W. Michael, "Modern prosthetic knee mechanisms," *Clinical Orthopaedics and Related Research®*, vol. 361, pp. 39–47, 1999.

[33] J. Paul, "Biomechanics," 1966.

[34] T.-W. Lu and C.-F. Chang, "Biomechanics of human movement and its clinical applications," *The Kaohsiung journal of medical sciences*, vol. 28, no. 2, pp. S13–S25, 2012.

[35] B. M. Nigg, *Biomechanics of the musculo-skeletal system*. John Wiley & Sons Incorporated, 2007.

[36] P. Allard, I. Stokes, and J. Blanchi, "Three-dimensional analysis of human movement. 1995," *Champaign, IL: Human Kinetics*.

[37] L. Chiari, U. Della Croce, A. Leardini, and A. Cappozzo, "Human movement analysis using stereophotogrammetry: Part 2: Instrumental errors," *Gait & posture*, vol. 21, no. 2, pp. 197–211, 2005.

[38] M. M. Martins, C. P. Santos, A. Frizera-Neto, and R. Ceres, "Assistive mobility devices focusing on smart walkers: Classification and review," *Robotics and Autonomous Systems*, vol. 60, no. 4, pp. 548–562, 2012.

[39] R. C. Simpson, "Smart wheelchairs: A literature review," *Journal of rehabilitation research and development*, vol. 42, no. 4, p. 423, 2005.

[40] K. Tanaka, K. Matsunaga, and H. O. Wang, "Electroencephalogram-based control of an electric wheelchair," *IEEE transactions on robotics*, vol. 21, no. 4, pp. 762–766, 2005.

[41] A. F. Neto, W. C. Celeste, V. R. Martins, T. F. Bastos Filho, and M. Sarcinelli Filho, "Human-machine interface based on electro-biological signals for mobile vehicles," in *2006 IEEE International Symposium on Industrial Electronics*, vol. 4, pp. 2954–2959, IEEE, 2006.

[42] D. G. Smith, P. Horn, D. Malchow, D. A. Boone, G. E. Reiber, and S. T. Hansen, "Prosthetic history, prosthetic charges, and functional outcome of the isolated, traumatic below-knee amputee," *Journal of Trauma and Acute Care Surgery*, vol. 38, no. 1, pp. 44–47, 1995.

[43] P. Hernigou, "Crutch art painting in the middle age as orthopaedic heritage (part i: the lepers, the poliomyelitis, the cripples)," *International orthopaedics*, vol. 38, no. 6, pp. 1329–1335, 2014.

[44] A. M. Dollar and H. Herr, "Lower extremity exoskeletons and active orthoses: challenges and state-of-the-art," *IEEE Transactions on robotics*, vol. 24, no. 1, pp. 144–158, 2008.

[45] N. J. Mizen, "Preliminary design for the shoulders and arms of a powered exoskeletal structure.," tech. rep., CORNELL AERONAUTICAL LAB INC BUFFALO NY, 1965.

[46] A. Schiele, "Ergonomics of exoskeletons: Objective performance metrics," in *EuroHaptics conference, 2009 and Symposium on Haptic Interfaces for Virtual Environment and Teleoperator Systems. World Haptics 2009. Third Joint*, pp. 103–108, IEEE, 2009.

[47] J. PARK, H. PARK, and J. KIM, "Performance estimation of the lower limb exoskeleton for plantarflexion using surface electromyography (semg) signals," *Journal of Biomechanical Science and Engineering*, vol. 12, no. 2, pp. 16–00595, 2017.

[48] J. Rose, E. E. Bleck, and J. G. Gamble, "Human walking, 2nd edn," *Developmental Medicine and Child Neurology*, vol. 37, no. 1, pp. 92–92, 1995.

[49] R. C. Browning, J. R. Modica, R. Kram, and A. Goswami, "The effects of adding mass to the legs on the energetics and biomechanics of walking," *Medicine & Science in Sports & Exercise*, vol. 39, no. 3, pp. 515–525, 2007.

[50] L. Stirling, C.-H. Yu, J. Miller, E. Hawkes, R. Wood, E. Goldfield, and R. Nagpal, "Applicability of shape memory alloy wire for an active, soft orthotic," *Journal of materials engineering and performance*, vol. 20, no. 4-5, pp. 658–662, 2011.

[51] A. T. Asbeck, S. M. De Rossi, K. G. Holt, and C. J. Walsh, "A biologically inspired soft exosuit for walking assistance," *The International Journal of Robotics Research*, vol. 34, no. 6, pp. 744–762, 2015.

[52] U. Onen, F. M. Botsali, M. Kalyoncu, M. Tinkir, N. Yilmaz, and Y. Sahin, "Design and actuator selection of a lower extremity exoskeleton,"

*IEEE/ASME Transactions on Mechatronics*, vol. 19, no. 2, pp. 623–632, 2014.

[53] S. Krut, M. Benoit, E. Dombre, and F. Pierrot, "Moonwalker, a lower limb exoskeleton able to sustain bodyweight using a passive force balancer," in *Robotics and Automation (ICRA), 2010 IEEE International Conference on*, pp. 2215–2220, IEEE, 2010.

[54] J. L. Johansson, D. M. Sherrill, P. O. Riley, P. Bonato, and H. Herr, "A clinical comparison of variable-damping and mechanically passive prosthetic knee devices.," *American journal of physical medicine & rehabilitation*, vol. 84 8, pp. 563–75, 2005.

[55] M. S. Cherry, D. J. Choi, K. J. Deng, S. Kota, and D. P. Ferris, "Design and fabrication of an elastic knee orthosis: preliminary results," in *Proceedings of IDETC/CIE ASME International Design Engineering Technical Conferences & Computers and Information in Engineering Conference. Philadelphia, USA*, 2006.

[56] C. J. Walsh, K. Endo, and H. Herr, "A quasi-passive leg exoskeleton for load-carrying augmentation," *International Journal of Humanoid Robotics*, vol. 4, no. 03, pp. 487–506, 2007.

[57] K. Endo, D. Paluska, and H. Herr, "A quasi-passive model of human leg function in level-ground walking," in *Intelligent Robots and Systems, 2006 IEEE/RSJ International Conference on*, pp. 4935–4939, IEEE, 2006.

[58] N. Costa and D. G. Caldwell, "Control of a biomimetic" soft-actuated" 10dof lower body exoskeleton," in *Biomedical Robotics and Biomechatronics, 2006. BioRob 2006. The First IEEE/RAS-EMBS International Conference on*, pp. 495–501, IEEE, 2006.

[59] S. Lessard, D. Castro, W. Asper, S. D. Chopra, L. B. Baltaxe-Admony, M. Teodorescu, V. SunSpiral, and A. Agogino, "A bio-inspired tensegrity manipulator with multi-dof, structurally compliant joints," in *Intelligent Robots and Systems (IROS), 2016 IEEE/RSJ International Conference on*, pp. 5515–5520, IEEE, 2016.

[60] Y. Bai, J. Wang, J.-p. Wu, J.-x. Dai, O. Sha, D. Tai Wai Yew, L. Yuan, and Q.-n. Liang, "Review of evidence suggesting that the fascia network could be the anatomical basis for acupoints and meridians in the human body," *Evidence-based complementary and alternative medicine*, vol. 2011, 2011.

[61] S. K. Dwivedy and P. Eberhard, "Dynamic analysis of flexible manipulators, a literature review," *Mechanism and machine theory*, vol. 41, no. 7, pp. 749–777, 2006.

[62] S. Ozgoli and H. Taghirad, "A survey on the control of flexible joint robots," *Asian Journal of Control*, vol. 8, no. 4, pp. 332–344, 2006.

[63] J. Hughes, U. Culha, F. Giardina, F. Guenther, A. Rosendo, and F. Iida, "Soft manipulators and grippers: a review," *Frontiers in Robotics and AI*, vol. 3, p. 69, 2016.

[64] T. George Thuruthel, Y. Ansari, E. Falotico, and C. Laschi, "Control strategies for soft robotic manipulators: A survey," *Soft robotics*, vol. 5, no. 2, pp. 149–163, 2018.

[65] M. Haegele, C. Maufroy, W. Kraus, M. Siee, and J. Breuninger, "Musculoskeletal robots and wearable devices on the basis of cable-driven actuators," in *Soft Robotics*, pp. 42–53, Springer, 2015.

[66] F. Ansarieshlaghi and P. Eberhard, "Hybrid force/position control of a very flexible parallel robot manipulator in contact with an environment.," in *ICINCO (2)*, pp. 59–67, 2019.

[67] M. Jiang, Z. Zhou, and N. Gravish, "Flexoskeleton printing enables versatile fabrication of hybrid soft and rigid robots," *Soft robotics*, vol. 7, no. 6, pp. 770–778, 2020.

[68] A. P. Sabelhaus, J. Bruce, K. Caluwaerts, P. Manovi, R. F. Firoozi, S. Dobi, A. M. Agogino, and V. SunSpiral, "System design and locomotion of superball, an untethered tensegrity robot," in *Robotics and Automation (ICRA), 2015 IEEE International Conference on*, pp. 2867–2873, IEEE, 2015.

[69] C. Paul, J. W. Roberts, H. Lipson, and F. V. Cuevas, "Gait production in a tensegrity based robot," in *Advanced Robotics, 2005. ICAR'05. Proceedings., 12th International Conference on*, pp. 216–222, IEEE, 2005.

[70] Y. Koizumi, M. Shibata, and S. Hirai, "Rolling tensegrity driven by pneumatic soft actuators," in *ICRA*, pp. 1988–1993, 2012.

[71] T. Flemons, "Tensegrity Wiki." `http://tensegritywiki.com`, 2017. [Online; accessed 15-September-2017].

[72] D. Blostein, "Simulation of abstract models of structural homeostasis," *Journal of bodywork and movement therapies*, vol. 20, no. 2, pp. 373–376, 2016.

[73] B. Mirletz, I.-W. Park, T. E. Flemons, A. K. Agogino, R. D. Quinn, and V. SunSpiral, "Design and control of modular spine-like tensegrity structures," in *The 6th World Conference of the International Association for Structural Control and Monitoring (6WCSCM)*, 2014.

[74] S. Levin, "The tensegrity-truss as a model for spine mechanics: Biotensegrity," *Journal of Mechanics in Medicine and Biology*, vol. 2, pp. 375–388, 2002.

[75] S. Lessard, P. Pansodtee, A. Robbins, L. B. Baltaxe-Admony, J. M. Trombadore, M. Teodorescu, A. Agogino, and S. Kurniawan, "Crux: A compliant robotic upper-extremity exosuit for lightweight, portable, multi-joint muscular augmentation," in *Rehabilitation Robotics (ICORR), 2017 International Conference on*, pp. 1633–1638, IEEE, 2017.

[76] F. Horst, S. Lapuschkin, W. Samek, K.-R. Müller, and W. I. Schöllhorn, "Explaining the unique nature of individual gait patterns with deep learning," *Scientific reports*, vol. 9, no. 1, pp. 1–13, 2019.

[77] C. Prakash, R. Kumar, and N. Mittal, "Recent developments in human gait research: parameters, approaches, applications, machine learning techniques, datasets and challenges," *Artificial Intelligence Review*, vol. 49, no. 1, pp. 1–40, 2018.

[78] R. E. Richards, M. S. Andersen, J. Harlaar, and J. Van Den Noort, "Relationship between knee joint contact forces and external knee joint moments in patients with medial knee osteoarthritis: effects of gait modifications," *Osteoarthritis and cartilage*, vol. 26, no. 9, pp. 1203–1214, 2018.

[79] A. Barre and S. Armand, "Biomechanical toolkit: Open-source framework to visualize and process biomechanical data," *Computer methods and programs in biomedicine*, vol. 114, no. 1, pp. 80–87, 2014.

[80] A. Barre, F. Leboeuf, S. Armand, *et al.*, "Openma: a new open source library for working and altering the conventional gait model," *Gait & Posture*, vol. 49, p. 260, 2016.

[81] A. De Luca and W. Book, "Robots with flexible elements. handbook of robotics, b. siciliano and o. khatib, eds," 2008.

[82] A. Jain, *Robot and multibody dynamics: analysis and algorithms*. Springer Science & Business Media, 2010.

[83] E. Todorov, "Convex and analytically-invertible dynamics with contacts and constraints: Theory and implementation in mujoco," in *2014 IEEE International Conference on Robotics and Automation (ICRA)*, pp. 6054–6061, IEEE, 2014.

[84] E. Rohmer, S. P. Singh, and M. Freese, "V-rep: A versatile and scalable robot simulation framework," in *2013 IEEE/RSJ International Conference on Intelligent Robots and Systems*, pp. 1321–1326, IEEE, 2013.

[85] N. Koenig and A. Howard, "Design and use paradigms for gazebo, an open-source multi-robot simulator," in *2004 IEEE/RSJ International Conference on Intelligent Robots and Systems (IROS)(IEEE Cat. No. 04CH37566)*, vol. 3, pp. 2149–2154, IEEE, 2004.

[86] C. Anagnostopoulos and A. P. Kalogeras, "An industrial simulator utilizing a gaming platform," in *2015 IEEE 20th Conference on Emerging Technologies & Factory Automation (ETFA)*, pp. 1–5, IEEE, 2015.

[87] K. Caluwaerts, J. Despraz, A. Işçen, A. P. Sabelhaus, J. Bruce, B. Schrauwen, and V. SunSpiral, "Design and control of compliant tensegrity robots through simulation and hardware validation," *Journal of The Royal Society Interface*, vol. 11, no. 98, p. 20140520, 2014.

[88] BulletPhysicsEngine, "http://www.bulletphysics.org/," 2013.

[89] R. Goyal, M. Chen, M. Majji, and R. E. Skelton, "Motes: Modeling of tensegrity structures," *Journal of Open Source Software*, vol. 4, no. 42, p. 1613, 2019.

[90] K. Pajunen, P. Johanns, R. K. Pal, J. J. Rimoli, and C. Daraio, "Design and impact response of 3d-printable tensegrity-inspired structures," *Materials & Design*, vol. 182, p. 107966, 2019.

[91] E. Todorov, T. Erez, and Y. Tassa, "Mujoco: A physics engine for model-based control," in *2012 IEEE/RSJ International Conference on Intelligent Robots and Systems*, pp. 5026–5033, IEEE, 2012.

[92] N. Docquier, A. Poncelet, and P. Fisette, "Robotran: a powerful symbolic gnerator of multibody models," *Mechanical Sciences*, vol. 4, no. 1, pp. 199–219, 2013.

[93] L. Tagliapietra, L. Modenese, E. Ceseracciu, C. Mazzà, and M. Reggiani, "Validation of a model-based inverse kinematics approach based on wearable inertial sensors," *Computer methods in biomechanics and biomedical engineering*, vol. 21, no. 16, pp. 834–844, 2018.

[94] D. Young, S. D'orey, R. Opperman, C. Hainley, and D. Newman, "Estimation of lower limb joint angles during walking using extended kalman filtering," in *6th World Congress of Biomechanics (WCB 2010). August 1-6, 2010 Singapore*, pp. 1319–1322, Springer, 2010.

[95] A. Karatsidis, M. Jung, H. M. Schepers, G. Bellusci, M. de Zee, P. H. Veltink, and M. S. Andersen, "Musculoskeletal model-based inverse dynamic analysis under ambulatory conditions using inertial motion capture," *Medical engineering & physics*, vol. 65, pp. 68–77, 2019.

[96] B. J. Borbély and P. Szolgay, "Real-time inverse kinematics for the upper limb: a model-based algorithm using segment orientations," *Biomedical engineering online*, vol. 16, no. 1, p. 21, 2017.

[97] D. Torricelli, C. Cortés, N. Lete, Á. Bertelsen, J. E. Gonzalez-Vargas, A. J. Del-Ama, I. Dimbwadyo, J. C. Moreno, J. Florez, and J. L. Pons, "A subject-specific kinematic model to predict human motion in exoskeleton-assisted gait," *Frontiers in neurorobotics*, vol. 12, p. 18, 2018.

[98] H. Zhou and H. Hu, "Human motion tracking for rehabilitation—a survey," *Biomedical Signal Processing and Control*, vol. 3, no. 1, pp. 1–18, 2008.

[99] P. O'donoghue, *Research methods for sports performance analysis*. Routledge, 2009.

[100] B. Bolsterlee, D. H. Veeger, and E. K. Chadwick, "Clinical applications of musculoskeletal modelling for the shoulder and upper limb," *Medical & biological engineering & computing*, vol. 51, no. 9, pp. 953–963, 2013.

[101] G. Wu, S. Siegler, P. Allard, C. Kirtley, A. Leardini, D. Rosenbaum, M. Whittle, D. D D'Lima, L. Cristofolini, H. Witte, *et al.*, "Isb recommendation on definitions of joint coordinate system of various joints for the reporting of human joint motion—part i: ankle, hip, and spine," *Journal of biomechanics*, vol. 35, no. 4, pp. 543–548, 2002.

[102] S. Sabatelli, M. Galgani, L. Fanucci, and A. Rocchi, "A double stage kalman filter for sensor fusion and orientation tracking in 9d imu," in *2012 IEEE Sensors Applications Symposium Proceedings*, pp. 1–5, IEEE, 2012.

[103] Y. Tian, H. Wei, and J. Tan, "An adaptive-gain complementary filter for real-time human motion tracking with marg sensors in free-living environments," *IEEE Transactions on Neural Systems and Rehabilitation Engineering*, vol. 21, no. 2, pp. 254–264, 2012.

[104] D. TarniŢă, "Wearable sensors used for human gait analysis," *Rom J Morphol Embryol*, vol. 57, no. 2, pp. 373–382, 2016.

[105] T. Seel, J. Raisch, and T. Schauer, "Imu-based joint angle measurement for gait analysis," *Sensors*, vol. 14, no. 4, pp. 6891–6909, 2014.

[106] L. S. Vargas-Valencia, A. Elias, E. Rocon, T. Bastos-Filho, and A. Frizera, "An imu-to-body alignment method applied to human gait analysis," *Sensors*, vol. 16, no. 12, p. 2090, 2016.

[107] Y. C. Han, K. I. Wong, and I. Murray, "Gait phase detection for normal and abnormal gaits using imu," *IEEE Sensors Journal*, vol. 19, no. 9, pp. 3439–3448, 2019.

[108] A. Kececi, A. Yildirak, K. Ozyazici, G. Ayluctarhan, O. Agbulut, and I. Zincir, "Implementation of machine learning algorithms for gait recognition," *Engineering Science and Technology, an International Journal*, 2020.

[109] E. Jung, C. Cheney, M. Contreras, D. Yong, V. Ly, and M. Teodorescu, "Low-cost motion tracking system using opensim for kinematic and dynamic analysis," *Engineering and technology*, Under Review.

[110] A. G. Cutti, A. Giovanardi, L. Rocchi, A. Davalli, and R. Sacchetti, "Ambulatory measurement of shoulder and elbow kinematics through inertial and magnetic sensors," *Medical & biological engineering & computing*, vol. 46, no. 2, pp. 169–178, 2008.

[111] W. De Vries, H. Veeger, A. Cutti, C. Baten, and F. Van Der Helm, "Functionally interpretable local coordinate systems for the upper extremity using inertial & magnetic measurement systems," *Journal of biomechanics*, vol. 43, no. 10, pp. 1983–1988, 2010.

[112] T. Cloete and C. Scheffer, "Benchmarking of a full-body inertial motion capture system for clinical gait analysis," in *2008 30th Annual International Conference of the IEEE Engineering in Medicine and Biology Society*, pp. 4579–4582, IEEE, 2008.

[113] D. Giansanti, G. Maccioni, F. Benvenuti, and V. Macellari, "Inertial measurement units furnish accurate trunk trajectory reconstruction of the sit-to-stand manoeuvre in healthy subjects," *Medical & biological engineering & computing*, vol. 45, no. 10, pp. 969–976, 2007.

[114] P. C. Dixon, J. J. Loh, Y. Michaud-Paquette, and D. J. Pearsall, "biomechzoo: An open-source toolbox for the processing, analysis, and visualization of biomechanical movement data," *Computer Methods and Programs in Biomedicine*, vol. 140, pp. 1–10, 2017.

[115] I. P. Pappas, M. R. Popovic, T. Keller, V. Dietz, and M. Morari, "A reliable gait phase detection system," *IEEE Transactions on neural systems and rehabilitation engineering*, vol. 9, no. 2, pp. 113–125, 2001.

[116] C. M. O'Connor, S. K. Thorpe, M. J. O'Malley, and C. L. Vaughan, "Automatic detection of gait events using kinematic data," *Gait & posture*, vol. 25, no. 3, pp. 469–474, 2007.

[117] J.-Y. Jung, W. Heo, H. Yang, and H. Park, "A neural network-based gait phase classification method using sensors equipped on lower limb exoskeleton robots," *Sensors*, vol. 15, no. 11, pp. 27738–27759, 2015.

[118] J. D. Farah, N. Baddour, and E. D. Lemaire, "Gait phase detection from thigh kinematics using machine learning techniques," in *2017 IEEE International Symposium on Medical Measurements and Applications (MeMeA)*, pp. 263–268, IEEE, 2017.

[119] R. Begg and J. Kamruzzaman, "A machine learning approach for automated recognition of movement patterns using basic, kinetic and kinematic gait data," *Journal of biomechanics*, vol. 38, no. 3, pp. 401–408, 2005.

[120] R. Kohavi *et al.*, "A study of cross-validation and bootstrap for accuracy estimation and model selection," in *Ijcai*, vol. 14, pp. 1137–1145, Montreal, Canada, 1995.

[121] G. Song, Y. Wang, M. Wang, and Y. Li, "Lower limb movement intent recognition based on grid search random forest algorithm," in *Proceedings of the 3rd International Conference on Robotics, Control and Automation*, pp. 225–229, 2018.

[122] T. Cover and P. Hart, "Nearest neighbor pattern classification," *IEEE transactions on information theory*, vol. 13, no. 1, pp. 21–27, 1967.

[123] A. Liaw, M. Wiener, *et al.*, "Classification and regression by randomforest," *R news*, vol. 2, no. 3, pp. 18–22, 2002.

[124] Motive, "Motive: Production motion capture software." `https://optitrack.com/products/motive/`, 2020.

[125] Oxford, "Oxford foot model." `https://www.vicon.com/software/oxford-foot-model/`, 2020.

[126] SimTK, "How Forward Dynamics Works." `https://simtk-confluence.stanford.edu/display/OpenSim/How+Forward+Dynamics+Works`, 1993. [Online; accessed 25-August-2017].

[127] N. Wang, J. D. Tytell, and D. E. Ingber, "Mechanotransduction at a distance: Mechanically coupling the extracellular matrix with the nucleus.," *Nature Reviews Molecular Cell Biology*, vol. 10, no. 1, pp. 75–82, 2009.

[128] A. Iscen, A. Agogino, V. SunSpiral, and K. Tumer, "Learning to control complex tensegrity robots," in *AAMAS*, 2013.

[129] A. Ikkala and P. Hämäläinen, "Converting biomechanical models from opensim to mujoco," *arXiv preprint arXiv:2006.10618*, 2020.

[130] SimTk, "How inverse kinematics works." `https://simtk-confluence.stanford.edu:8443/display/OpenSim/How+Inverse+Kinematics+Works`. Accessed: 2020-02-15.

[131] D. G. Thelen, "Adjustment of muscle mechanics model parameters to simulate dynamic contractions in older adults," *Journal of biomechanical engineering*, vol. 125, no. 1, pp. 70–77, 2003.

[132] E. Jung, V. Ly, A. Buderi, E. Appleton, and M. Teodorescu, "Design and selection of muscle excitation patterns for modeling a lower extremity joint inspired tensegrity," in *2019 Third IEEE International Conference on Robotic Computing (IRC)*, pp. 282–287, IEEE, 2019.

[133] S. R. Hamner, A. Seth, K. M. Steele, and S. L. Delp, "A rolling constraint reproduces ground reaction forces and moments in dynamic simulations of walking, running, and crouch gait," *Journal of biomechanics*, vol. 46, no. 10, pp. 1772–1776, 2013.

[134] R. Skelton and J. Mirats-Tur, "Nonlinear control of non-minimal tensegrity models," in *Decision and Control, 2009 held jointly with the 2009 28th Chinese Control Conference. CDC/CCC 2009. Proceedings of the 48th IEEE Conference on*, pp. 6662–6667, Dec 2009.

[135] A. Falisse, S. Van Rossom, J. Gijsbers, F. Steenbrink, B. J. van Basten, I. Jonkers, A. J. van den Bogert, and F. De Groote, "Opensim versus human body model: a comparison study for the lower limbs during gait," *Journal of applied biomechanics*, vol. 34, no. 6, pp. 496–502, 2018.

[136] D. Castro, *Modeling the human knee using tensegrity*. PhD thesis, University of California, Santa Cruz, 2017.

[137] V. C. Dionisio, G. L. Almeida, M. Duarte, and R. P. Hirata, "Kinematic, kinetic and emg patterns during downward squatting," *Journal of Electromyography and Kinesiology*, vol. 18, no. 1, pp. 134–143, 2008.

[138] E. M. Arnold, S. R. Ward, R. L. Lieber, and S. L. Delp, "A model of the lower limb for analysis of human movement," *Annals of biomedical engineering*, vol. 38, no. 2, pp. 269–279, 2010.

[139] M. M. Hamdi, M. I. Awad, M. M. Abdelhameed, and F. A. Tolbah, "Lower limb motion tracking using imu sensor network," in *2014 Cairo International Biomedical Engineering Conference (CIBEC)*, pp. 28–33, IEEE, 2014.

[140] S. O. Madgwick, A. J. Harrison, and R. Vaidyanathan, "Estimation of imu and marg orientation using a gradient descent algorithm," in *2011 IEEE international conference on rehabilitation robotics*, pp. 1–7, IEEE, 2011.

[141] Adafruit, "Adafruit unified bno055 driver (ahrs/orientation)." `https://github.com/adafruit/Adafruit_BNO055`. Accessed: 2021-03-10.

[142] P. Barralon, N. Vuillerme, and N. Noury, "Walk detection with a kinematic sensor: Frequency and wavelet comparison," in *2006 International Conference of the IEEE Engineering in Medicine and Biology Society*, pp. 1711–1714, IEEE, 2006.

[143] J. Goudsmit, S. L. Giudici, J. Herweijer, and S. Vos, "Measuring running workload and key points during treadmill running using a custom build 'nodes' system," in *Multidisciplinary Digital Publishing Institute Proceedings*, vol. 49, p. 30, 2020.

[144] C. Mitschke, F. Zaumseil, and T. L. Milani, "The influence of inertial sensor sampling frequency on the accuracy of measurement parameters in rearfoot running," *Computer methods in BiomeChaniCs and BiomediCal engineering*, vol. 20, no. 14, pp. 1502–1511, 2017.

[145] "Bno055 odr 2," Jun 2019.

[146] G. Scarr, "A consideration of the elbow as a tensegrity structure," *International Journal of Osteopathic Medicine*, vol. 15, no. 2, pp. 53–65, 2012.

[147] A. Wang, J. Lu, Y. Ge, J. Yu, and S. Zhang, "Simulation of limb rehabilitation robot based on opensim," in *International Conference on Bio-Inspired Computing: Theories and Applications*, pp. 647–654, Springer, 2019.

[148] P. Kutilek, Z. Svoboda, and P. Smrcka, "Evaluation of bilateral asymmetry of the muscular forces using opensim software and bilateral cyclograms," in *Mechatronics 2013*, pp. 801–808, Springer, 2014.

[149] A. Scarton, I. Jonkers, A. Guiotto, F. Spolaor, G. Guarneri, A. Avogaro, C. Cobelli, and Z. Sawacha, "Comparison of lower limb muscle strength between diabetic neuropathic and healthy subjects using opensim," *Gait & posture*, vol. 58, pp. 194–200, 2017.

[150] T. Rudy, G. Livesay, S.-Y. Woo, and F. Fu, "A combined robotic/universal force sensor approach to determine in situ forces of knee ligaments," *Journal of biomechanics*, vol. 29, no. 10, pp. 1357–1360, 1996.

[151] L. Roussel, C. Canudas-de Wit, and A. Goswami, "Generation of energy optimal complete gait cycles for biped robots," vol. 3, pp. 2036–2041, 1998.

[152] B. Appleton, "Stretching and Flexibility: Normal Ranges of Joint Motion." `https://people.bath.ac.uk/masrjb/Stretch/stretching_8.html`, 2007. [Online; accessed 20-August-2017].

[153] G. Panahandeh, N. Mohammadiha, A. Leijon, and P. Händel, "Continuous hidden markov model for pedestrian activity classification and gait analysis," *IEEE Transactions on Instrumentation and Measurement*, vol. 62, no. 5, pp. 1073–1083, 2013.

[154] F. Tafazzoli, G. Bebis, S. Louis, and M. Hussain, "Improving human gait recognition using feature selection," in *International Symposium on Visual Computing*, pp. 830–840, Springer, 2014.

[155] A. Mannini, D. Trojaniello, A. Cereatti, and A. M. Sabatini, "A machine learning framework for gait classification using inertial sensors: Application to elderly, post-stroke and huntington's disease patients," *Sensors*, vol. 16, no. 1, p. 134, 2016.

[156] W. R. Johnson, A. Mian, C. J. Donnelly, D. Lloyd, and J. Alderson, "Predicting athlete ground reaction forces and moments from motion capture," *Medical & biological engineering & computing*, vol. 56, no. 10, pp. 1781–1792, 2018.

[157] D. Michie, D. J. Spiegelhalter, C. Taylor, *et al.*, "Machine learning," *Neural and Statistical Classification*, vol. 13, no. 1994, pp. 1–298, 1994.

[158] S. Choi, I.-H. Youn, R. LeMay, S. Burns, and J.-H. Youn, "Biometric gait recognition based on wireless acceleration sensor using k-nearest neighbor classification," in *2014 International Conference on Computing, Networking and Communications (ICNC)*, pp. 1091–1095, IEEE, 2014.

[159] M. Derlatka and M. Bogdan, "Ensemble knn classifiers for human gait recognition based on ground reaction forces," in *2015 8th International Conference on Human System Interaction (HSI)*, pp. 88–93, IEEE, 2015.

[160] L. Wang, H. Ning, W. Hu, and T. Tan, "Gait recognition based on procrustes shape analysis," in *Proceedings. International Conference on Image Processing*, vol. 3, pp. III–III, IEEE, 2002.

[161] K. Chomboon, P. Chujai, P. Teerarassamee, K. Kerdprasop, and N. Kerdprasop, "An empirical study of distance metrics for k-nearest neighbor algorithm," in *Proceedings of the 3rd international conference on industrial application engineering*, pp. 280–285, 2015.

[162] F. Pedregosa, G. Varoquaux, A. Gramfort, V. Michel, B. Thirion, O. Grisel, M. Blondel, P. Prettenhofer, R. Weiss, V. Dubourg, *et al.*, "Scikit-learn: Machine learning in python," *the Journal of machine Learning research*, vol. 12, pp. 2825–2830, 2011.

[163] D. Paper, "Scikit-learn classifier tuning from simple training sets," *Hands-on Scikit-Learn for Machine Learning Applications: Data Science Fundamentals with Python*, pp. 137–163, 2020.

[164] R. J. Lewis, "An introduction to classification and regression tree (cart) analysis," in *Annual meeting of the society for academic emergency medicine in San Francisco, California*, vol. 14, 2000.

[165] T. Suzuki, S. Sonoda, E. Saitoh, K. Onogi, H. Fujino, T. Teranishi, T. Oyobe, M. Katoh, and K. Ohtsuka, "Prediction of gait outcome with the knee–ankle–foot orthosis with medial hip joint in patients with spinal cord injuries: a study using recursive partitioning analysis," *Spinal Cord*, vol. 45, no. 1, pp. 57–63, 2007.

[166] Q. Guo and D. Jiang, "Method for walking gait identification in a lower extremity exoskeleton based on c4. 5 decision tree algorithm," *International Journal of Advanced Robotic Systems*, vol. 12, no. 4, p. 30, 2015.

[167] H. H. Manap, N. M. Tahir, and R. Abdullah, "Parkinsonian gait motor impairment detection using decision tree," in *2013 European Modelling Symposium*, pp. 209–214, IEEE, 2013.

[168] D. Coppersmith, S. J. Hong, and J. R. Hosking, "Partitioning nominal attributes in decision trees," *Data Mining and Knowledge Discovery*, vol. 3, no. 2, pp. 197–217, 1999.

[169] P. A. Chou, "Optimal partitioning for classification and regression trees," *IEEE Transactions on Pattern Analysis & Machine Intelligence*, no. 4, pp. 340–354, 1991.

[170] N. R. Draper and H. Smith, *Applied regression analysis*, vol. 326. John Wiley & Sons, 1998.

[171] P. Geurts, D. Ernst, and L. Wehenkel, "Extremely randomized trees," *Machine learning*, vol. 63, no. 1, pp. 3–42, 2006.

[172] C. Morbidoni, L. Principi, G. Mascia, A. Strazza, F. Verdini, A. Cucchiarelli, and F. Di Nardo, "Gait phase classification from surface emg signals using neural networks," in *Mediterranean Conference on Medical and Biological Engineering and Computing*, pp. 75–82, Springer, 2019.

[173] V. Agostini, G. Balestra, and M. Knaflitz, "Segmentation and classification of gait cycles," *IEEE Transactions on Neural Systems and Rehabilitation Engineering*, vol. 22, no. 5, pp. 946–952, 2013.

[174] C. Kalkbrenner, S. Hacker, M.-E. Algorri, and R. Blechschmidt-Trapp, "Motion capturing with inertial measurement units and kinect," in *Proc. Int. Joint Conf. Biomed. Eng. Syst. Technol*, vol. 1, pp. 120–126, 2014.

[175] H. M. Reynolds and R. P. Hubbard, "Anatomical frames of reference and biomechanics," *Human factors*, vol. 22, no. 2, pp. 171–176, 1980.

[176] A. R. Wu, C. S. Simpson, E. H. van Asseldonk, H. van der Kooij, and A. J. Ijspeert, "Mechanics of very slow human walking," *Scientific reports*, vol. 9, no. 1, pp. 1–10, 2019.

[177] J. Majernik *et al.*, "Normative human gait databases," *Statistics Research Letters*, vol. 2, no. 3, pp. 69–74, 2013.

[178] Y. Asano, H. Mizoguchi, M. Osada, T. Kozuki, J. Urata, T. Izawa, Y. Nakanishi, K. Okada, and M. Inaba, "Biomimetic design of musculoskeletal humanoid knee joint with patella and screw-home mechanism," in *2011 IEEE International Conference on Robotics and Biomimetics*, pp. 1813–1818, IEEE, 2011.

[179] L. B. Baltaxe-Admony, A. S. Robbins, E. A. Jung, S. Lessard, M. Teodorescu, V. SunSpiral, and A. Agogino, "Simulating the human shoulder through active tensegrity structures," in *International Design Engineering Technical Conferences and Computers and Information in Engineering Conference*, vol. 50183, p. V006T09A027, American Society of Mechanical Engineers, 2016.

[180] Y. Asano, H. Mizoguchi, M. Osada, T. Kozuki, J. Urata, T. Izawa, Y. Nakanishi, K. Okada, and M. Inaba, "Biomimetic design of musculoskeletal humanoid knee joint with patella and screw-home mechanism," *Robotics and Biomimetics (ROBIO), 2011 IEEE International Conference on*, pp. 1813–1818, 2011.

[181] H. L. Kamenetz, "A brief history of the wheelchair," *Journal of the history of medicine and allied sciences*, vol. 24, no. 2, pp. 205–210, 1969.

[182] L. P. Kaelbling, M. L. Littman, and A. W. Moore, "Reinforcement learning: A survey," *Journal of artificial intelligence research*, vol. 4, pp. 237–285, 1996.

[183] S. Bembli, N. K. Haddad, and S. Belghith, "Robustness analysis of an upper-limb exoskeleton using monte carlo simulation," in *2018 International Conference on Advanced Systems and Electric Technologies (IC_ASET)*, pp. 78–84, IEEE, 2018.

[184] J. Kober and J. Peters, "Reinforcement learning in robotics: A survey," in *Reinforcement Learning*, pp. 579–610, Springer, 2012.

[185] A. J. Young and D. P. Ferris, "State of the art and future directions for lower limb robotic exoskeletons," *IEEE Transactions on Neural Systems and Rehabilitation Engineering*, vol. 25, no. 2, pp. 171–182, 2017.

[186] J. R. Davis, *Tensile testing*. ASM international, 2004.

[187] T. R. Clites, M. J. Carty, S. Srinivasan, A. N. Zorzos, and H. M. Herr, "A murine model of a novel surgical architecture for proprioceptive muscle feedback and its potential application to control of advanced limb prostheses," *Journal of neural engineering*, vol. 14, no. 3, p. 036002, 2017.

[188] N. Mohd Hawari, M. Jawaid, P. Md Tahir, and R. A. Azmeer, "Case study: survey of patient satisfaction with prosthesis quality and design among below-knee prosthetic leg socket users," *Disability and Rehabilitation: Assistive Technology*, vol. 12, no. 8, pp. 868–874, 2017.

[189] B. T. Dyer, S. Noroozi, S. Redwood, and P. Sewell, "The design of lower-limb sports prostheses: fair inclusion in disability sport," *Disability & Society*, vol. 25, no. 5, pp. 593–602, 2010.

[190] J. B. Waanders, T. Hortobágyi, A. Murgia, P. DeVita, and J. R. Franz, "Advanced age redistributes positive but not negative leg joint work during walking," *Medicine and science in sports and exercise*, vol. 51, no. 4, p. 615, 2019.

[191] Y. Asano, H. Mizoguchi, M. Osada, T. Kozuki, J. Urata, T. Izawa, Y. Nakanishi, K. Okada, and M. Inaba, "Biomimetic design of musculoskeletal humanoid knee joint with patella and screw-home mechanism," pp. 1813–1818, 2011.

[192] D. Phan, N. Nguyen, P. N. Pathirana, M. Horne, L. Power, and D. Szmulewicz, "A random forest approach for quantifying gait ataxia with truncal and peripheral measurements using multiple wearable sensors," *IEEE Sensors Journal*, vol. 20, no. 2, pp. 723–734, 2019.

[193] Y. Zhang and Y. Ma, "Application of supervised machine learning algorithms in the classification of sagittal gait patterns of cerebral palsy children with spastic diplegia," *Computers in biology and medicine*, vol. 106, pp. 33–39, 2019.

[194] M.-S. Scholz, J. Blanchfield, L. Bloom, B. Coburn, M. Elkington, J. Fuller, M. Gilbert, S. Muflahi, M. Pernice, S. Rae, *et al.*, "The use of composite materials in modern orthopaedic medicine and prosthetic devices: A review," *Composites Science and Technology*, vol. 71, no. 16, pp. 1791–1803, 2011.

[195] A. M. Karmarkar, D. M. Collins, T. Wichman, A. Franklin, S. G. Fitzgerald, B. E. Dicianno, P. F. Pasquina, and R. A. Cooper, "Prosthesis and wheelchair use in veterans with lower-limb amputation.," *Journal of Rehabilitation Research & Development*, vol. 46, no. 5, 2009.

[196] Y. Yanneng and Z. Li, "Mathematical model and simulation of magnetic levitation spherical driving joint with inverse system decoupling control," *RN*, vol. 2, p. 1, 2012.

[197] D. Murphy, D. Connolly, and B. Beynnon, "Risk factors for lower extremity injury: a review of the literature," *British journal of sports medicine*, vol. 37, no. 1, pp. 13–29, 2003.

[198] N. Tolou, M. Simi, P. Valdastri, J. Herder, P. Dario, and A. Menciassi, "Modeling of a compliant joint in a magnetic levitation system for an endoscopic camera," *Mechanical Sciences, 3 (1), 2012*, 2012.

[199] F. Sup, A. Bohara, and M. Goldfarb, "Design and control of a powered transfemoral prosthesis," *The International journal of robotics research*, vol. 27, no. 2, pp. 263–273, 2008.

[200] L. J. Hargrove, A. J. Young, A. M. Simon, N. P. Fey, R. D. Lipschutz, S. B. Finucane, E. G. Halsne, K. A. Ingraham, and T. A. Kuiken, "Intuitive control of a powered prosthetic leg during ambulation: a randomized clinical trial," *Jama*, vol. 313, no. 22, pp. 2244–2252, 2015.

[201] J. E. Pratt, B. T. Krupp, C. J. Morse, and S. H. Collins, "The roboknee: an exoskeleton for enhancing strength and endurance during walking," in *Robotics and Automation, 2004. Proceedings. ICRA'04. 2004 IEEE International Conference on*, vol. 3, pp. 2430–2435, IEEE, 2004.

[202] J. C. Perry, J. Rosen, and S. Burns, "Upper-limb powered exoskeleton design," *IEEE/ASME transactions on mechatronics*, vol. 12, no. 4, pp. 408–417, 2007.

[203] L. Lucas, M. DiCicco, and Y. Matsuoka, "An emg-controlled hand exoskeleton for natural pinching," *Journal of Robotics and Mechatronics*, vol. 16, pp. 482–488, 2004.

[204] M. Hutter, C. D. Remy, M. A. Höpflinger, and R. Siegwart, "Slip running with an articulated robotic leg," in *Intelligent Robots and Systems (IROS), 2010 IEEE/RSJ International Conference on*, pp. 4934–4939, IEEE, 2010.

[205] H. K. Yap, J. H. Lim, F. Nasrallah, J. C. Goh, and R. C. Yeow, "A soft exoskeleton for hand assistive and rehabilitation application using pneumatic

actuators with variable stiffness," in *Robotics and Automation (ICRA), 2015 IEEE International Conference on*, pp. 4967–4972, IEEE, 2015.

[206] D. Howe, "Magnetic actuators," *Sensors and Actuators A: Physical*, vol. 81, no. 1, pp. 268–274, 2000.

[207] K. Shamaei, M. Cenciarini, A. A. Adams, K. N. Gregorczyk, J. M. Schiffman, and A. M. Dollar, "Design and evaluation of a quasi-passive knee exoskeleton for investigation of motor adaptation in lower extremity joints," *IEEE Transactions on Biomedical Engineering*, vol. 61, no. 6, pp. 1809–1821, 2014.

[208] A. Gams, T. Petrič, T. Debevec, and J. Babič, "Effects of robotic knee exoskeleton on human energy expenditure," *IEEE Transactions on Biomedical Engineering*, vol. 60, no. 6, pp. 1636–1644, 2013.

[209] J. F. Veneman, R. Kruidhof, E. E. Hekman, R. Ekkelenkamp, E. H. Van Asseldonk, and H. Van Der Kooij, "Design and evaluation of the lopes exoskeleton robot for interactive gait rehabilitation," *IEEE Transactions on Neural Systems and Rehabilitation Engineering*, vol. 15, no. 3, pp. 379–386, 2007.

[210] H. Kazerooni, A. Chu, and R. Steger, "That which does not stabilize, will only make us stronger," *The International Journal of Robotics Research*, vol. 26, no. 1, pp. 75–89, 2007.

[211] K. Low, X. Liu, and H. Yu, "Development of ntu wearable exoskeleton system for assistive technologies," in *Mechatronics and Automation, 2005 IEEE International Conference*, vol. 2, pp. 1099–1106, IEEE, 2005.

[212] N. Lefeber, E. Swinnen, M. Michielsen, S. Henderix, and E. Kerckhofs, "Energy consumption and cardiorespiratory load during lokomat walking compared to walking without robot-assistance in stroke patients: Preliminary results," in *Converging Clinical and Engineering Research on Neurorehabilitation II*, pp. 1229–1233, Springer International Publishing, 2017.

[213] M. Cestari, D. Sanz-Merodio, J. C. Arevalo, and E. Garcia, "An adjustable compliant joint for lower-limb exoskeletons," *IEEE/ASME Transactions on Mechatronics*, vol. 20, no. 2, pp. 889–898, 2015.

[214] S. Wang, C. Meijneke, and H. van der Kooij, "Modeling, design, and optimization of mindwalker series elastic joint," in *Rehabilitation Robotics (ICORR), 2013 IEEE International Conference on*, pp. 1–8, IEEE, 2013.

[215] G. Aguirre-Ollinger, J. E. Colgate, M. A. Peshkin, and A. Goswami, "Design of an active one-degree-of-freedom lower-limb exoskeleton with inertia compensation," *The International Journal of Robotics Research*, vol. 30, no. 4, pp. 486–499, 2011.

[216] K. Kong and D. Jeon, "Fuzzy control of a new tendon-driven exoskeletal power assistive device," in *Proceedings of the IEEE/ASME International Conference on Advanced Intelligent Mechatronics (AIM 2005)*, pp. 146–151, 2005.

[217] Y. Zhao, W. Zhang, W. Ge, and S. Li, "Finite element simulation of soldier lower extremity exoskeleton," *Journal of Multimedia*, vol. 8, no. 6, pp. 705–711, 2013.

[218] H. K. Kwa, J. H. Noorden, M. Missel, T. Craig, J. E. Pratt, and P. D. Neuhaus, "Development of the ihmc mobility assist exoskeleton," in *Robotics and Automation, 2009. ICRA'09. IEEE International Conference on*, pp. 2556–2562, IEEE, 2009.

[219] J. Gancet, M. Ilzkovitz, G. Cheron, Y. Ivanenko, H. van der Kooij, F. van der Helm, F. Zanow, and F. Thorsteinsson, "Mindwalker: a brain controlled lower limbs exoskeleton for rehabilitation. potential applications to space," in *11th Symposium on advanced space technologies in robotics and automation*, pp. 12–14, 2011.

[220] K. L. Moore, A. F. Dalley, and A. M. Agur, *Clinically oriented anatomy.* Lippincott Williams & Wilkins, 2013.

[221] C. J. Snow and K. Blacklin, "Reliability of knee flexor peak torque measurements from a standardized test protocol on a kin/com dynamometer," *Archives of physical medicine and rehabilitation*, vol. 73, no. 1, pp. 15–21, 1992.

[222] K. M. Steele, M. S. DeMers, M. H. Schwartz, and S. L. Delp, "Compressive tibiofemoral force during crouch gait," *Gait & posture*, vol. 35, no. 4, pp. 556–560, 2012.

[223] T. Sugihara, Y. Nakamura, and H. Inoue, "Real-time humanoid motion generation through zmp manipulation based on inverted pendulum control," in *Robotics and Automation, 2002. Proceedings. ICRA'02. IEEE International Conference on*, vol. 2, pp. 1404–1409, IEEE, 2002.

[224] L. Wang, S. Wang, E. H. van Asseldonk, and H. van der Kooij, "Actively controlled lateral gait assistance in a lower limb exoskeleton," in *Intelligent Robots and Systems (IROS), 2013 IEEE/RSJ International Conference on*, pp. 965–970, IEEE, 2013.

[225] B. Ugurlu, M. Nishimura, K. Hyodo, M. Kawanishi, and T. Narikiyo, "A framework for sensorless torque estimation and control in wearable exoskeletons," in *Advanced Motion Control (AMC), 2012 12th IEEE International Workshop on*, pp. 1–7, IEEE, 2012.

[226] Q. Wu, X. Wang, F. Du, and X. Zhang, "Design and control of a powered hip exoskeleton for walking assistance," *International Journal of Advanced Robotic Systems*, vol. 12, no. 3, p. 18, 2015.

[227] H. Aguilar-Sierra, R. Lopez, W. Yu, S. Salazar, and R. Lozano, "A lower limb exoskeleton with hybrid actuation," in *Biomedical Robotics and Biomechatronics (2014 5th IEEE RAS & EMBS International Conference on*, pp. 695–700, IEEE, 2014.

[228] K. K. Karunakaran and R. Foulds, "Control of foot trajectory in biped robots," in *Bioengineering Conference (NEBEC), 2013 39th Annual Northeast*, pp. 203–204, IEEE, 2013.